Badania Nieniszczące i Diagnostyka

2/2018
Kwartalnik Naukowo-Techniczny

Nondestructive Testing and Diagnostics

Rok założenia 2016 PLISSN 2451-4462 Cena 18,50 zł (w tym 5% VAT)

OLYMPUS®

NOWOŚĆ: Wideoskop IPLEX G Lite

IPLEX G LITE

- IP65, MIL-STD, niska waga i 2x mocniejsze światło
- Nowy procesor obrazu i system artykulacji
- Specjalny system ciągłego nagrywania obrazu
- Pomiar skalarny w standardzie i opcjonalne pomiary Stereo
- Wymienne źródła światła UV lub IR

O szczegóły oferty zapytaj przedstawiciela Olympus
lub wyślij zapytanie na **industrial@olympus.pl**

Olympus Polska Sp. z o. o. | ul. Suwak 3, 02-676 Warszawa | tel.: (22) 366 00 77

industrial@olympus.pl | www.olympus-ims.com

WYDAWCA/PUBLISHER

Badania Nieniszczące i Diagnostyka
Agenda Wydawnicza SIMP
ul. Sabały 11a, 71-341 Szczecin
tel. +48 576 400 550
e-mail: wydawnictwo@ptbnidt.pl
www.bnid.pl

KWARTALNIK NAUKOWO-TECHNICZNY AGENDA WYDAWNICZA SIMP

Badania Nieniszczące i Diagnostyka

Nondestructive Testing and Diagnostics

NR 2/2018 ISSN 2451-4462 VOLUMEN 3

SPIS TREŚCI

Alexander Balitskii, Karol Franciszek Abramek, Tomasz Osipowicz
Technical diagnostics fuel injection pump condition used of fuel with hydrogen containing admixtures* 3

Cesar Camerini, João M. A. Rebello, Lucas Braga, Rafael Santos, João Marcio Santos, Gabriela Pereira
Eddy Current System for Complex Geometry Inspection in High Speed Application* 6

Abhishek Pandala, S. Shivaprasad, C.V. Krishnamurthy, Krishnan Balasubramaniam
Robust and efficient finite-difference-time-domain modelling of the propagation of nonlinear elastic waves* 11

Przemysław Łopato
Notatka z wyborów PTBNiDT SIMP 21

Łukasz Rawicki, Karol Kaczmarek, Paweł Irek, Grzegorz Hottowy, Jacek Słania
Badania ultradźwiękowe szyn kolejowych* 23

Volodymyr Troitskiy
Industrial X-ray testing without intermediate data carriers of information* 29

Konferencja "Szkolenia i certyfikacja personelu NDT w TÜV Rheinland Polska" 36

Volodymyr Troitskiy
News in maintenance of technical state of the main pipelines* 37

Gábor Vértesy
Nondestructive investigation of wall thinning in ferromagnetic material by Magnetic adaptive testing: influence of yoke size* 45

Konferencje NDT 49

Informacje dla Autorów i Czytelników 50

* - artykuł recenzowany

INSTYTUT SPAWALNICTWA
Polskie Spawalnicze Centrum Doskonałości

Szkolenia z dofinansowaniem UE

Ofertę Instytutu znajdziesz

w Bazie Usług Rozwojowych:

uslugirozwojowe.parp.gov.pl

Instrukcja jak uzyskać dofinansowanie:

www.is.gliwice.pl/strona-cms/dofinansowanie-ze-srodkow-europejskich

Instytut Spawalnictwa
ul. Bł. Czesława 16-18, 44-100 Gliwice
tel.: 32 231 00 11, fax: 32 231 46 52
is@is.gliwice.pl, www.is.gliwice.pl

Alexander Balitskii[1,2]*, Karol Franciszek Abramek[1], Tomasz Osipowicz[1]
[1]Zachodniopomorski Uniwersytet Technologiczny w Szczecinie
[2]Karpenko Physico-Mechanical Institute of the National Academy of Sciences of Ukraine, Lviv, Ukraine

Technical diagnostics fuel injection pump condition used of fuel with hydrogen containing admixtures

Diagnostyka stanu technicznego pompy wtryskowej pracującej na wzbogaconym dodatkami zawierającymi wodór paliwie

ABSTRACT

Article describes high pressure fuel pump CP1H Common Rail system which worked on fuel with hydrogen containing admixtures. It was presented how can high pressure injection pump diagnose. Research object was dismantled on spare parts and checked under microscope. Paper discusses construction and mechanism of action researched fuel pump. During the researches has been presented crucial elements of pump. It has been described the areas where are produced metal fillings in pressure pump and discussed the methods of prevents them.

Keywords: *high pressure pump, fuel dosages, Common Rail system, fuel injector, CI – engine*

STRESZCZENIE

W artykule przedstawiono pompę wtryskową układu Common Rail typu CP1H, która pracowała na zanieczyszczonym dodatkami zawierającymi wodór paliwie. Pokazano, w jaki sposób można zdiagnozować pompę wtryskową, rozmontowaną na części składowe oraz poddano badaniom mikroskopowym. W referacie została omówiona budowa badanej pompy oraz zasada działania. Podczas badań zostały przedstawione najbardziej newralgiczne elementy pompy. Przedstawiono również miejsca pompy, w których tworzą się niebezpieczne metaliczne opiłki oraz omówiono metody im zapobiegania.

Słowa kluczowe: *pompa wysokiego ciśnienia, dawka paliwa, układ Common Rail, wtryskiwacz paliwa, silnik ZS*

1. Introduction

Common Rail system is at present the most popular injection solution. Because of work condition whole system is very important right fuel quality. There is necessary to keep whole injection system in cleanness or in controlled [1-7]. Fuel pollution is frequent reason of fuel injectors or high pressure pump damages is spite of using special fuel filters. Main source of fuel pollution are: atmosphere factors, friction, corrosion processes and chemical reaction. The most frequent reason damages injection system aresolid bodies (metal filings, Si, Fe and Al oxides, HC), H_2O and corrosion products [8]. Figure 1 presents fuel from high pressure rail polluted with metal fillings.

Theoretically there is no possibility to get water to fuel during refining because of right production and cleaning technology. Water doesn't dissolve in the fuel only makes suspension. The main reason of getting water to engine fuel are transportation and distribution, not appropriate storing and condensation water vapour especially in fuel tanks. Water in engine fuel causes decrease fuel energetic value, corrosion in whole system, greasiness decrease, worst fuel pumping and filter what damages precision elements in fuel injectors and high pressure pumps [9].

2. Description of modern fuel pump

Main task of fuel injection pump is generate high pressure in system in all work engine range. Common Rail system pump generates pressure constantly independent of injection process. There is three section piston radius high pressure pump in cars and as well an in – line high pressure pump with two sections in trucks. High pressure pump is powered from engine through the clutch, flywheels, chain or fan belt. Rotation speed of fuel pump changes with rotation engine speed [10].

High pressure Common Rail system fuel pump is constructed with main body where is on the bearing high pressure section propulsion shaft [6]. Placed on the shaft eccentric makes high pressure section to sliding motion. The move of power from shaft to section piston occurs roller, slide ring and mounted under piston plate. Rotational speed of fuel pump depends on engines speed. Propulsion correlation between pressure pump and engine should be match so that quantity pump fuel were not so high but to cover fuel demand by full engine load [8].

Fuel is led to high pressure section and there is accumulated. Section are moved by pump shaft with help eccentric. High pressure is controlled by high or low pressure valve. It depends on sort Common Rail system. There are two ways of Common Rail steering (high or low pressure). The first systems were controlled only by high pressure valve. Fuel surfeit were transferred to fuel tank. This solution has fault because it was wasted to much energy to accumulate fuel and warm fuel were transferred back to tank. Therefore it was used low pressure valve (fuel dispenser). Main task

*Correspondence author. E-mail: balitski@ipm.lviv.ua

DOI: 10.26357/BNiD.2018.006

of dispenser was transfer that much fuel to high pressure pump how much it was need in given moment. This solution reduced waste of energy [10].

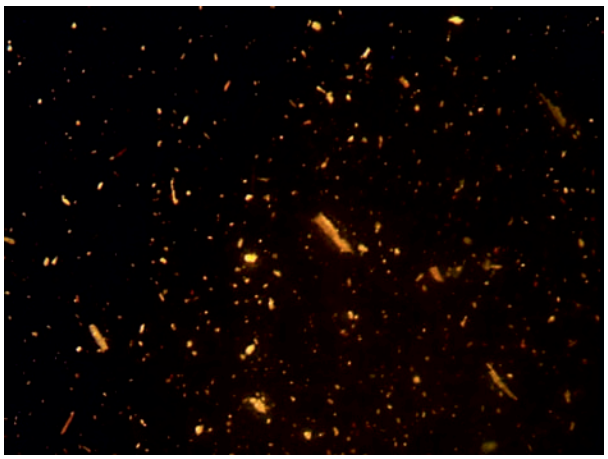

Fig. 1. Pollute fuel with metal fillings from high pressure system rail
Rys. 1. Zanieczyszczone paliwo metalicznymi opiłkami z układu wysokiego ciśnienia

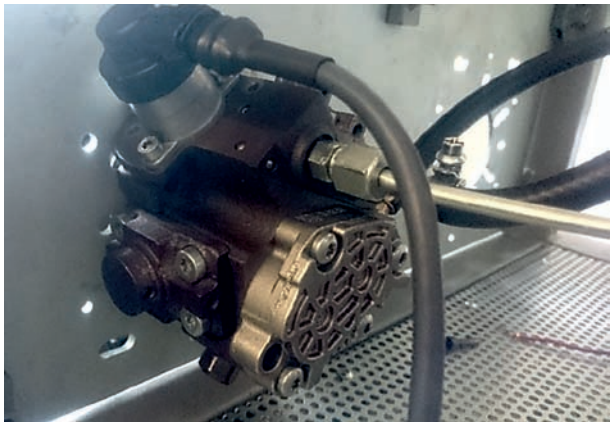

Fig. 2. High pressure Bosch CP1H fuel pump mounted on STPiW 3 test bench
Rys. 2. Wysokociśnieniowa pompa wtryskowa Bosch typ CP1H zamontowana na stanowisku probierczym

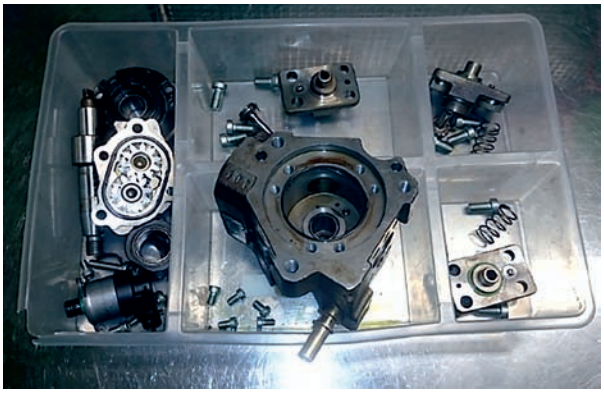

Fig. 3. High pressure Bosch CP1H fuel pump disassemble on spare parts
Rys. 3. Wysokociśnieniowa pompa wtryskowa Bosch typ CP1H zdemontowana na element składowe

There are three types of CP1 high pressure pumps: CP1S (standard), CP1K (compact) and CP1H (reinforced). Piston radial high pressure fuel pump CP1H is reinforced version of CP1 family pumps. It is adapted to higher pressures (160 MPa) because of increase main body strength, changes valve units and reinforces pump propulsion [7]. It was improved energy efficiency through adjustment fuel dosage to section by dispenser valve. Figure 1 presents CP1H high pressure pump [5]

3. Influence the fuel quality on high pressure pump work

The first sign of defect high pressure pump is problem with supporting system pressure in maximum load dosages range [4]. There is perceptible drop engine power in that range. The reason of this is to low system pressure because fuel pump is not able to generate it. The reason of this is defect the high pressure sections. Figure 4 presents high pressure pump divides on two modules: A – propulsion, B – high pressure section. The propulsion module contains propulsion shaft with bearing and eccentricity, efficiency valve and initial fuel pump. High pressure module is responsible for bank up fuel. It contains head with piston, bearing and valve. Figures 5 – 8 present elements depend on high pressure pump parameters. Elements were observed under microscope. There is noticeable considerable their usage.

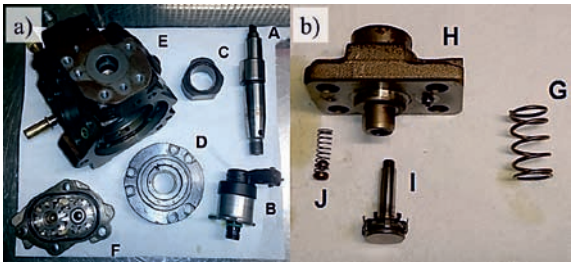

Fig. 4. A – main body with steering and propulsion section, B – high pressure section: A – propulsion shaft, B – efficiency valve, C – eccentricity, D – main bearing, E - main body, F – initial fuel pump, G – piston in high pressure spring, H – high pressure section head, I – high pressure section piston, J – high pressure section valve
Rys. 4. A – korpus pompy wtryskowej z regulatorem wydatku oraz sekcją napędową, B – sekcja wysokiego ciśnienia: A – wałek napędowy, B – zawór wydatku, C – łożysko ślizgowe napędzające sekcje wysokiego ciśnienia, D – pierścień z łożyskiem głównym, E – korpus pompy wtryskowej, F – pompka przetłaczająca, G – sprężyna w sekcji wysokiego ciśnienia, H – głowiczka sekcji wysokiego ciśnienia, I – tłoczek sekcji wysokiego ciśnienia, J – zaworek wysokiego ciśnienia

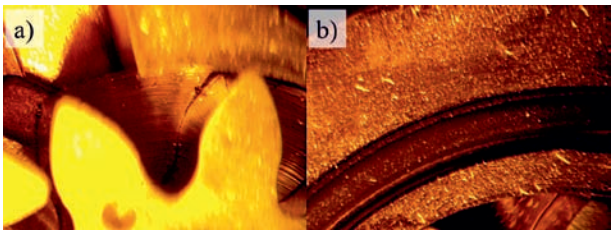

Fig. 5. A – low pressure pump inside, B – polluted area of low pressure pump
Rys. 5. A – wnętrze pompki wysokiego ciśnienia, B – zanieczyszczona powierzchnia pompki przetłaczającej

Figures 7 - 8 present work diagrams of researched high pressure pump. Figure 7 shows the magnitude of fuel

efficiency. There is noticeable that faulty pump has lower fuel efficiency but figures 8 presents that in spite of lower fuel efficiency this pump has higher functionality. During high pressure researches the most important factor is fuel efficiency. Only when fuel efficiency parameters are correctly it is possible to counting fuel pump functionality. There is possibility to calculate practically functionality of fuel pump. The efficiency of correct working pump is 573 mm^3 (1000 rotation of pump) by system pressure 0 MPa. Efficient fuel pump has 523 mm^3 by 100 MPa system pressure. Pump functionality is 91%. Faulty pump has by 100 MPa 150 mm^3 fuel efficiency by 100 MPa. Its theoretical functionality 93% but practical only 26%. It means that high pressure pump is damage.

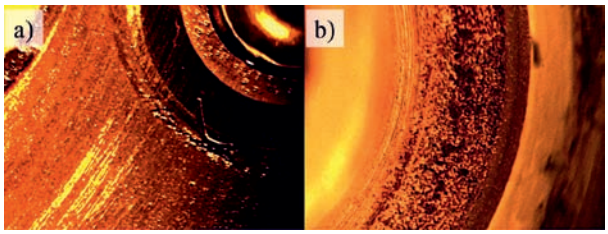

Fig. 6. A, B – high pressure section head
Rys. 6. A, B – głowiczka sekcji wysokiego ciśnienia

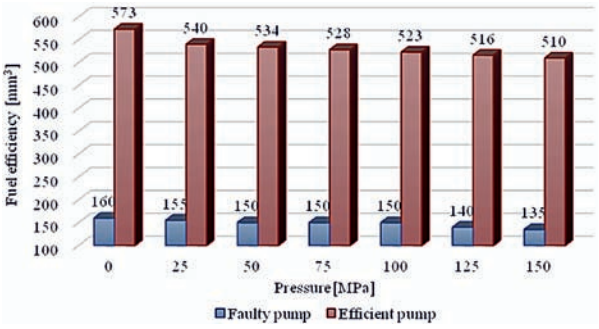

Fig. 7. High pressure pump fuel efficiency [mm^3] diagram
Rys. 7. Wydatek pompy wysokiego ciśnienia [mm^3]

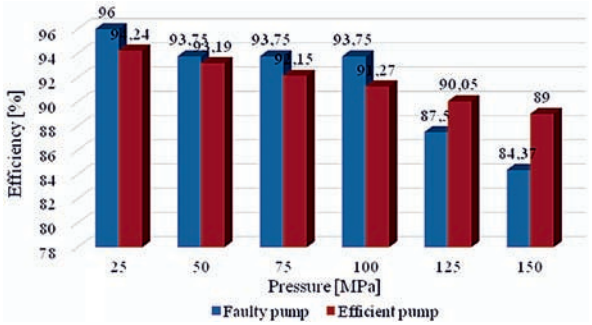

Fig. 8. High pressure pump efficiency [%] diagram
Rys. 8. Sprawność pompy wysokiego ciśnienia [%]

4. Conclusion

The main work parameter of high pressure pump are fuel efficiencies and practical functionality. High pressure pump is functional in huge range of fuel pressure from 25 to 160 MPa. The elements depend on make pressure are sections. Technical conditions of precision elements sections pistons influence on efficiency magnitude. Bad quality fuel damages friction areas in low pressure initial fuel pump. There are produce metal filing between spinning pump elements and pump area. Metal fillings are very dangerous. These damage not only high pressure elements but fuel pump propulsion shaft, main bearing, eccentricity and sealers. Metal filings move with fuel in high pressure system to injectors damaging them. There is in fuel water in spite of air humidity. It causes local corrosion in various high pressure pump elements especially on precision elements (fig. 7). Practical high pressure pump functionality is use full method of diagnosing. It is calculated from efficient pump fuel efficiency without system pressure and research pump fuel efficiency by 100 MPa system pressure. Fuel rotation speed is 1000 turns per minute. So calculates efficient determines usage degree of fuel pump. The range of correctly working high pressure pump efficient is 80 – 100%. Researched pump has of efficiency higher than 80% but fuel efficiency were low. It means that high pressure section were uses similar to turbines elements [11, 12].

5. References/Literatura

[1] Stepniak D., Surwilo J., Skarpetowski B. Badania eksperymentalne silnika spalinowego zasilanego paliwem płynnym typu diesel wzbogaconym wodorem // Mechanik. – 2016. – N 7. – S. 827-829.
[2] Balyts'kyi O.I., Abramek K.F. , Shtoeck T., Osipowicz T. Evaluation of the losses of hydrogen-containing gases in the process of wear of pistons of an internal-combustion engine // Materials Science. - 2017. – Vol.53, N 2. – P. 289 -294.
[3] Ambrozik A., Ambrozik T., Łagowski P.: Fuel impact on emissions of harmful components of the exhaust gas from the ci engine during cold start up. Eksploatacja i Niezawodnosc – maintenance and realiability, 2015, 17(1), 95 – 99.
[4] Günther H.: Common Rail – Systeme in der Werkstattpraxis. Technik, Prüfung, Diagnose. Bad Wörihofen. Krafthand Verlag Walter Schultz GmbH, 2012.
[5] Osipowicz T., Abramek K. F., Stoeck T.: Testing of modern common rail fuel injectors. Combustion Engines. 2015, 162(3), 688-694.
[6] Osipowicz T.: Diagnosing common rail fuel injectors using fuel micro – doses. TEKA. Commission of Motorization and Energetics in Agriculture. 2015, 15(1), 61 – 64.
[7] Osipowicz T.: Analysis of the costs and cost – efficiency of regeneration of modern fuel injection systems in ci engines. Econtechmod. An international quarterly journal. 2016, 5(2), 45 – 50.
[8] Osipowicz T., Lisowski M.: The influence of corrosion phenomena on operational parameters of modern fuel injectors CI – engines. Combustion Engines. 2017, 171(4), 17 – 23.
[9] Olszewski W.: Paliwa i materiały smarowe. Badania i pomiary laboratoryjne podstawowych własności fizykochemicznych. Politechnika Radomska Wydawnictwo, 2009.
[10] Zasobnikowe układy wtryskowe Common Rail. Informator techniczny sterowanie silników ZS.Robert Bosch GmbH. WKiŁ,2005, 2009.
[11] Balyts'kyi O.I., Chmiel J., Krause P., Niekrasz J., Maciag M. The role of hydrogen in cavitation fracture of C45 steel in lubricants // Materials Science.– 2009, Vol. 45, N 5, p. 651-654.
[12] Balitskii A.I., Ivaskevich L.M., Mochulskyi V.M. Temperature dependences of age-hardening austenitic steels mechanical properties in gaseous hydrogen // 12th International Conference on Fracture 2009, ICF-12,Vol. 8, 2009, p. 5786-5792. Ottawa, ON; Canada; 12 July 2009 through 17 July 2009; Code 93954.

Cesar Camerini[1]*, João M. A. Rebello[2], Lucas Braga[1], Rafael Santos[3], João Marcio Santos[3], Gabriela Pereira[1,2]
[1]*Laboratory of Nondestructive Testing, Corrosion and Welding, Federal University of Rio de Janeiro, Brazil*
[2]*Federal University of Rio de Janeiro, Metallurgy and Materials Department, Rio de Janeiro, Brazil*
[3]*Petrobras R&D Centre, Rio de Janeiro, Brazil*

Eddy Current System for Complex Geometry Inspection in High Speed Application

System wiroprądowy do kompleksowej kontroli geometrii w zastosowaniach z dużą prędkością

ABSTRACT

Rigid pipelines installed in offshore structures for oil and gas production are built from pipe sections connected by circumferential welds. Such welds are generally points of stress concentration and therefore the regions that most demand periodic inspection. The weld geometry and the inspection speed required for in service inspection are the main challenges associated to the inspection procedure. In the present work an eddy current transducer with sensing coils placed orthogonally and connected in differential mode was introduced to evaluate fatigue cracks in weld root. A dedicated embedded electronic hardware was developed to drive the transducer and measure the electrical complex impedance of the coils and was specifically designed for operation under autonomous in-line inspection tool in a speed range between 0.5 – 1.0 m/s. The achieved results have confirmed that the introduced eddy current transducer is a potential solution for fatigue crack detection in irregular surfaces like weld root, while the hardware developed presented a reasonable SNR and achieved the data rate required to be incorporated in an autonomous in-line inspection tool.

Keywords: *fatigue crack; weld root; eddy current testing; in-line inspection tool*

STRESZCZENIE

Sztywne rurociągi instalowane w morskich konstrukcjach do produkcji ropy i gazu budowane są z odcinków rur połączonych spoinami obwodowymi. Takie spoiny są zwykle punktami koncentracji naprężeń, a zatem regionami, które w największym stopniu wymagają okresowej kontroli. Geometria spoiny i prędkość kontroli wymagana do przeprowadzenia badania serwisowego stanowią główne wyzwania związane z procedurą inspekcji. W niniejszej pracy, w celu oceny pęknięć zmęczeniowych w rdzeniu spoiny, zaproponowano przetwornik wiroprądowy z cewkami pomiarowymi umieszczonymi ortogonalnie i połączonymi różnicowo. Opracowano specjalny wbudowany system elektroniczny do sterowania przetwornikiem i pomiaru impedancji złożonych cewek elektrycznych. System został zaprojektowany specjalnie do pracy jako autonomiczna jednostka inspekcji linii w zakresie prędkości od 0,5 do 1,0 m/s. Uzyskane wyniki potwierdziły, że wprowadzony przetwornik wiroprądowy jest potencjalnym rozwiązaniem umożliwiającym wykrywania pęknięć zmęczeniowych na nieregularnych powierzchniach, takich jak rdzeń spoiny. Ponadto opracowany sprzęt zapewnia odpowiedni współczynnik stosunku sygnału do szumu SNR i osiąga prędkość transmisji wymaganą dla zastosowania w jednostkach niezależnej kontroli w linii.

Słowa kluczowe: *pęknięcie zmęczeniowe; rdzeń spawu; testowanie wiroprądowe; jednostka kontroli inline*

1. Introduction

Rigid pipelines installed in offshore structures for oil production are built from pipe sections connected by circumferential welds. The application of clad material to subsea rigid pipelines is recently gaining ground in deep water oil exploration. Its bimetallic configuration presents an attractive combination of mechanical strength and corrosion resistance, ensuring the safety and integrity of pipelines that connect the reservoir to oil rig. The clad material for oil exploration consists of a base material, usually carbon steel, inner coated with a thin layer of corrosion resistance alloy (CRA), turning into an attractive economical solution for deep water exploration since only a small portion of the noble anti-corrosive alloy is required. Clad material has a metallurgical bond between the CRA and the base material attained by the carbon diffusion during the hot rolling process [1].

The potential for fatigue cracks to occur in pipeline structures due to cycling loads inherent of any offshore oil production, such as, tide variation, waves, ocean current, platform movements, etc., makes necessary have an inspection tool to carry out periodic nondestructive inspection in the inner pipe surface, figure 1A and B. It is worth mentioning that the inspection tool highlighted in figure 1A flows inside the pipeline propelled by the oil flow at a velocity which at the most times exceed 0.5 m/s.

In case of clad material, it is crucial to detect fatigue crack on its initial stage because if the crack propagates through the layer of the CRA and reaches the carbon steel a strong galvanic couple is completed accelerating exponentially the fatigue corrosion process [2]. In this context, the weld geometry and the inspection speed required for in service inspection are the main challenges associated to the inspection procedure. Figure 2 shows the influence of the weld geometry associated with the inspection speed. Assuming a high-speed condition and a crack in the opposite side of the weld root, in such circumstance the sensor path may not pass exactly through the crack contour surface.

In the present work an eddy current transducer with coils placed orthogonally and differentially connected was introduced to evaluate fatigue cracks in weld root. A dedicated embedded electronic hardware was developed to drive the

*Correspondence author. E-mail: cgcamerini@metalmat.ufrj.br

DOI: 10.26357/BNiD.2018.007

transducer and measure the electrical complex impedance of the coils and was specifically designed for operation under autonomous in-line inspection tool in a speed range between 0.5 – 1.0 m/s. In the laboratory experiments, an automated inspection was performed with the goal to evaluate transducer's detectability and different scanning speed was tested to reproduce in service situation.

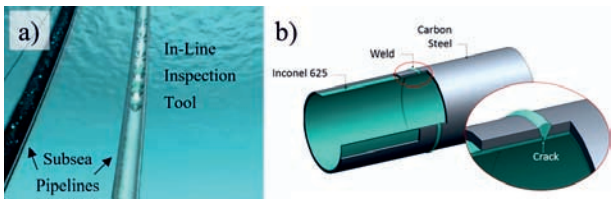

Fig. 1. A) Subsea pipelines and the in-line inspection tool (PIG), and B) Clad pipe section with the inspection region highlighted.
Rys. 1. A) Rurociągi podmorskie i jednostka inspekcji in-line (PIG) i B) Wybrany odcinek rury z powiększonym obszarem kontrolnym.

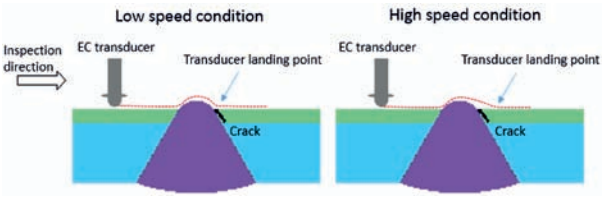

Fig. 2. Influence of the weld geometry and the inspection speed in the crack detectability.
Rys. 2. Wpływ geometrii spoiny i prędkości kontroli na wykrywalności pęknięć.

The techniques instrumented in the commercial in-line inspection tool, such as, MFL (Magnetic Flux Leakage), Ultrasound, EMAT (Electromagnetic Acoustic Transducer), are very effective in inspection of general corrosion or micro cracks in the base metal of carbon steel pipelines [5-7]. However, because of some practical limitation, such techniques are not efficient in micro cracks detection, especially in welded parts. Reber et.al. [8] have shown an ultrasonic configuration for crack detection in carbon steel pipeline girth welds and presented significant experimental results demonstrating the technique capability. The authors highlighted in their conclusions that the application of such technique in in-line inspection tools is still a challenge. Such challenge gets more complex in case of clad material inspection, where the anti-corrosive layer results in an additional interface for the ultrasonic wave propagation, interfering directly in the incident and refracted wave. Moreover, Cheng et.al. [9] pointed out that ultrasonic testing is not effective for inspections of Inconel welds because of its strong inhomogeneity and anisotropy. Once the ultrasound wave is sensitive to grain structures [10], Inconel welds significantly scatter the waves so that clear echoes due to defects cannot always be noticed.

Such challenge motivates the feasibility study of an in-line inspect tool development to detect fatigue cracks in the circumferential welds of clad pipelines based on eddy current concept. Yusa et.al. [11, 12] and Todorov et.al. [13] presented the capability of the EC transducer for fatigue crack detection in welded joints. Among the publications analyzed [11-18], it was verified that the EC transducer with orthogonal configuration of coils exhibits the most relevant inspection results. Its differential configuration and the fact that the coils are located in close proximity to each other, minimizes the influence of the weld root profile in the inspection signal. Besides the relevant results completed with such orthogonal transducer, none of the studied authors evaluated its behavior and performance when operating at high speed condition, relevant for field application for pipeline inspection. In addition, the tests performed in the examined studies used commercial or lab EC equipment, which restricts the application in tools that demands embedded electronic hardware.

Thus, the goal of the present work is evaluate the capability of an EC transducer to successfully meet the previously described requirements: detect fatigue cracks in the circumferential weld root of clad pipelines when operating at different inspection speed. It is worth mention that the in-line tool is propelled by the oil flow, which is inherently inconstant. An orthogonal coils EC based transducer was manufactured and tested, and a specific electronic hardware was developed to drive the transducer and measure the testing coils electrical complex impedance.

2. Materials and measuring system

A clad plate with substrate of carbon steel high strength low alloy, API 5L X65, and clad layer of Inconel 625, with dimensions 120x80x15mm, was manufactured with a 45° bevel to receive a weld bead from GTAW (Gas Tungsten Arc Welding) weld process. An Electrical Discharge Machining (EDM) notch with dimensions of 10.0x1.5x0.2mm was machined in the central part of the Inconel side between the weld root and the Inconel base material. Figure 3a presents a photo of the testing sample with the EDM notch indication, while 3b a metallographic image of the weld cross section after mechanical grinding, polishing and etching with chromium nitride solution. One may note the thickness of the carbon steel layer, 12mm, and the Inconel 625 clad of 3mm.

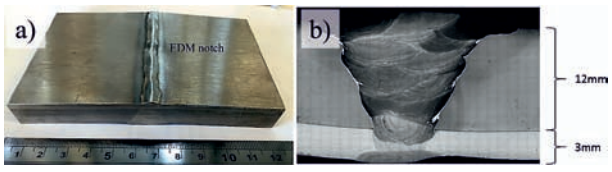

Fig. 3. a) Clad sample with the weld bead and EDM notch; b) metallographic image of the weld cross section.
Rys. 3. a) Próbka warstwowa (materiał platerowany) ze spoiną i nacięciem EDM; b) obraz metalograficzny przekroju spoiny.

The transducer manufactured to inspect the notch, consists of the testing coils placed in orthogonal configuration with layers interweaved, wounded over a dielectric core as shown by figure 4a. The coils are differentially connected thereby reducing spurious signals caused by variation of the distance to examined material during the inspection process [18]. When compared with EC pencil probes, orthogonal coils present low sensitivity to lift-off, allowing reduction

of its influence rate from 40 dB/mm to 8 dB/mm. For weld inspection orthogonal coils configuration present relevant results because spurious signals arising from some specific materials characteristics or from some physical structures that are common to both coils are annihilated thereby providing no undesirable response. Each manufactured coil present 5 interleaved layers with 15 turns per layer, and an average inductance of 36.1 μH. The transducer testing frequency was 400 kHz and to assist the inspection, a KUKA robotic arm model Hollow Wrist with KRC4 controller was used (Figure 4b). With a payload of five kilograms, the robotic arm carry the sensors and tests different inspection speed from 0.05 m/s to 1.0 m/s.

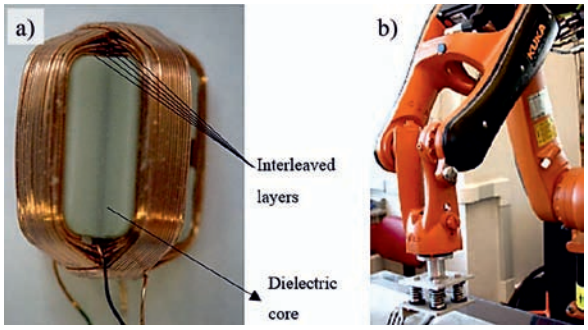

Fig. 4. A) Orthogonal coils with the layers interweaved, and B) KUKA robotic arm for automated inspection.
Rys. 4. A) Cewki ortogonalne z przeplotem warstw i B) Ramię robota KUKA do zautomatyzowanej kontroli.

The electronic hardware was developed to drive the EC sensors and measure the electrical complex impedance of the testing coils. Figure 5 present the basic concept of the EC coils impedance calculation procedure. First, in order to conduct the calculations, both voltage and current of the testing coil were measured. For that purpose, the shunt resistor was utilized and two complex potentials (V1, and V2) were sensed. Then, the Ohm's law in phasor form is applied to obtain the magnitude (eq. 6) and angle (eq. 7) of the complex impedance as demonstrated by equation 1- 7.

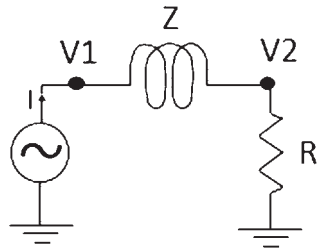

Fig. 5. Electrical scheme of a coil.
Rys. 5. Schemat zastępczy układu cewki.

$$V_1 = |V_1|e^{j\varphi_1} = |V_1|\cos(\varphi_1) + j|V_1|\sin(\varphi_1) \quad (1)$$

$$V_2 = |V_2|e^{j\varphi_2} = |V_2|\cos(\varphi_2) + j|V_2|\sin(\varphi_2) \quad (2)$$

$$V_2 = RI \rightarrow \frac{V_2}{R} = I \quad (3)$$

$$V_1 - V_2 = Z.I = \frac{Z.V_2}{R} \quad (4)$$

$$\frac{R(V_1 - V_2)}{V_2} = Z \quad (5)$$

$$|Z| = R\frac{\sqrt{\left(|V_1|\cos(\varphi_1) - |V_2|\cos(\varphi_2)\right)^2 + \left(|V_1|\sin(\varphi_1) - |V_2|\sin(\varphi_2)\right)^2}}{\sqrt{\left(|V_2|\cos(\varphi_2)\right)^2 + \left(|V_2|\sin(\varphi_2)\right)^2}} \quad (6)$$

$$\angle Z = \arctan\left(\frac{|V_1|\sin(\varphi_1) - |V_2|\sin(\varphi_2)}{|V_1|\cos(\varphi_1) - |V_2|\cos(\varphi_2)}\right) - \arctan\left(\frac{|V_2|sin(\varphi_2)}{|V_2|\cos(\varphi_2)}\right) \quad (7)$$

Figure 6 presents the block scheme of the measuring system while figure 7 shows a photo of the developed electronic Printed Circuit Board (PCB). As shown in the block scheme, the excitation signal is a sine wave with parameters defined in the form of the table and store in the microprocessor, which follows to a digital-to-analog converter (DAC) and a power amplifier to finally drive the coils. The hardware measures signals that are scaled versions of the voltage over the coils and their currents. These signals are digitized by an analog-to-digital converter (ADC). Then, in order to turn the digitized waveforms into phasors, a Fast Fourier Transform (FFT) or a similar algorithm, allowing processing the analysis in frequency domain, is applied.

Initially the algorithm implemented in the microprocessor ARM 32-bit to calculate the magnitude and phase of the complex impedance was the Fast Fourier Transform (FFT). However, in order to improve the hardware processing time and consequently the experimental data rate, the FFT was replaced with the Goertzel algorithm. The Goertzel algorithm is an efficient evaluation of individual terms of the Discrete Fourier Transform (DFT). When the full spectrum analysis needs to be carried out, the Goertzel algorithm is less efficient, because it presents a higher order of complexity than FFT. On the other side, in case of computing a small number of frequency components, it is more numerically efficient (then using the FFT), being very useful for small processors and embedded applications [19]. In the case of conventional EC testing, where the transducer is excited by a single known frequency, the Goertzel algorithm seems to be very suitable to calculate the coil impedance variation.

Equation 8 [19] presents the computed DFT term for the input sequence x[n] in the chosen frequency range ω_0 using the Goertzel analysis. The index k indicates the frequency bin of the DFT. If, for instance, a sine wave with 8 points was used, then the 8th bin of the FFT will have the real and imaginary information that can be turned into magnitude and phase. However, if, instead of using FFT to calculate all the bins, it is possible to use the Goertzel algorithm to calculate only x[7], where less computational effort is conducted.

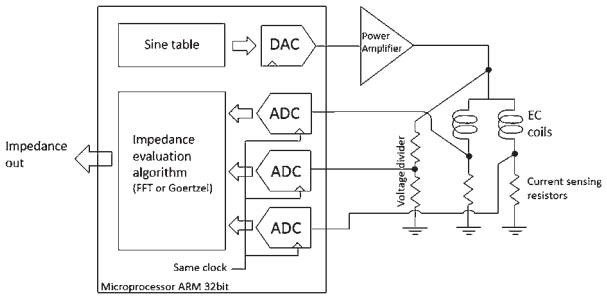

Fig. 6. Schematic block of the hardware to drive the eddy current coils and evaluate the impedance variation.
Rys. 6. Schemat blokowy układu do zasilania cewek wiroprądowych i pomiaru zmienny impedancji.

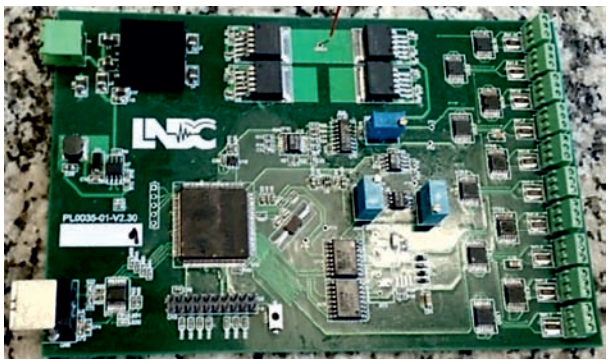

Fig. 7. Photo of the electronic hardware developed to drive and measure the EC transducer impedance variation.
Rys. 7. Zdjęcie układu elektronicznego opracowanego do zasilania i pomiaru zmienny impedancji przetwornika EC.

$$y[N] = \sum_{n=0}^{N} x[n]e^{-j\omega_0} \tag{8}$$

where: $\omega_0 = 2\pi \frac{k}{N}$ and $k \in \{0, 1, 2, \ldots, N-1\}$.

The use of the Goertzel algorithm offered a significant improvement in the hardware data streaming. In comparison to the FFT, the Goertzel analysis resulted in a calculation speed six times faster. On the other hand, while it provides only a single term of the DFT some relevant information, especially concerning harmonics content, is lost. If the excitation signal saturates the ADC it can be easily noticed by the distortion caused in the FFT spectrum and can be evaluated based on the harmonics analysis. In such case, the total harmonic distortion (THD) coefficient can be used. It defines the ratio between main and other harmonics and gives evidences about the behavior of the coil input excitation signal. However, according to the properties of the Goertzel algorithm, the calculation of THD is limited then. Nevertheless, it was decided to work with the faster algorithm in order to increase the hardware data streaming, which is quite relevant for high speed application. Finally, with the faster calculation and less data in the streaming package (THD data is only calculated in the FFT version) allowed the total data rate of the electronic hardware to be increased from ≈50 Hz (1/10.5 ms) for FFT to ≈100 Hz (1/19 ms) for Goertzel.

3. Results and discussion

The testing sample was scanned with different scan speed, 0.2, 0.5 and 1.0 m/s, using the orthogonal EC transducer operating at 400 kHz. Figure 8 presents the experimental schematic where an array of five EC transducers scanned the clad sample. The notch was set in the opposite side of the weld root so that the array must pass over the weld before passing through the notch. The transducer were excited and its response signal measured using the hardware developed. To scan the sample the transducer were set in longitudinal alignment with a lateral spacing of 1 mm, reaching the high scan resolution for in-line inspection tools defined by Barbian et.al. [20]. Although the tests were performed on flat plates, it is considered representative for a circumferential inspection condition. The flat arrangement is mainly used because it simplifies the mechanical arrangement and consequently the tests with different scan speed.

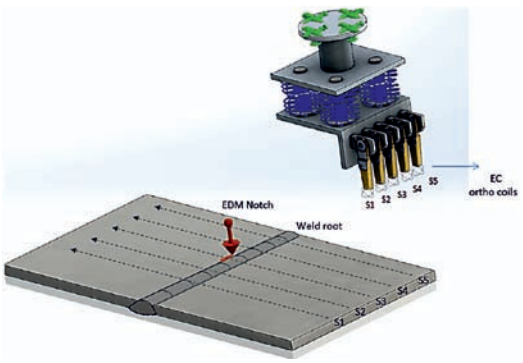

Fig. 8. Inspection result of the clad sample with the notch besides the weld bead.
Rys. 8. Wynik kontroli platerowanej próbki z wycięciem poza ściegiem spoiny.

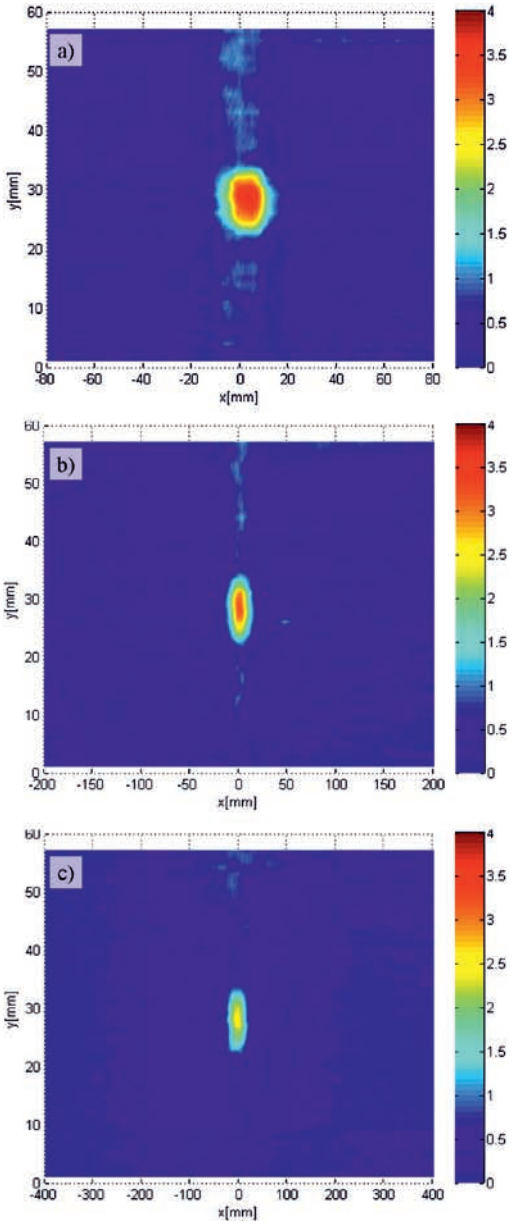

Fig. 9. Inspection results of different scanning speed of the clad sample, where: A) 0.2 m/s, B) 0.5 m/s and C) 1.0 m/s.
Rys. 9. Wyniki kontroli otrzymane dla różnej prędkości skanowania próbki platerowanej: A) 0,2 m/s, B) 0,5 m/s oraz C) 1,0 m/s.

During the movement of the array, the output signal of each transducer was measured, and the two-dimensional distributions of the signals' amplitude are shown in Figure 9a, b and c. One can observe that in all speed condition, the EDM notch can be clearly distinguished from the weld bead and, as the scanning speed increases, the notch signals amplitude are significantly attenuated.

Besides the clear identification of the notch, these results corroborates the fact that as higher the scanning speed, higher is the weld geometry influence in the inspection results. As presented in figure 2, according to the inspection speed there is a transducer trajectory associated in the weld root region. The present results made it explicit that even in high-speed condition, 1.0 m/s, it is possible to detect the notch with the suggested EC array and the developed hardware. It is worth mention that the presented experiments were performed with no lift-off, which in case of long distance inspection might result in a severe abrasion of the transducers along the pipeline inner wall.

4. Conclusions

A dedicated hardware was developed to drive the EC transducer and measure the electrical complex impedance. The Goertzel algorithm implementation improved the hardware data rate, which seems to be a relevant alternative for high-speed inspection tools where only a single frequency is evaluated. Different inspection condition was tested and as the speed is increased the notch identification signal attenuates, mainly because of the weld penetration geometry which makes difficult to proper profile the weld bead. The suggested EC system using the developed hardware and the transducer with orthogonal configuration presented the possibility to implement an in-line inspection tool to detect fatigue cracks in clad pipelines.

5. Acknowledgments

Authors gratefully acknowledge sponsorship by PETROBRAS, CAPES and CNPq.

6. References/Literatura

[1] Jones, R., Karunakara, N, D., Mair, J.,Wang, H., Reeled Clad SCR Weld Fatigue Qualification, Subsea 7 and Exxon Mobil Development, OMAE 2008.
[2] Largura, J. Prediction of Fatigue Behavior of Seal Welds of Lined Pipes. Master's thesis, COPPE/UFRJ, Rio de Janeiro, RJ, Brazil, September, 2011.
[3] Da Silva. S.E. Fatigue Crack Propagation in Circumferential Welded Joints of Steels for Rigid Risers Class API 5l Grade X80. Engineering graduation project. Escola Politécnica/PEMM/UFRJ, Rio de Janeiro, RJ, Brazil, March, 2010.
[4] J. Freire. Engenharia de dutos. Rio de Janeiro: ABCM; 2009.
[5] D. Babcook Energy Limited. "Evaluation of the effectiveness of non-destructive testing screening methods for in-service inspection" RR 659 Research Report, Health and Safety Executive, 2009.
[6] Austin Albright, The Detection of Stress Corrosion Cracking in Natural Gas Pipelines Using Electromagnetic Acoustic Transducers [Masters Theses], University of Tennessee – Knoxville, 2007.
[7] M. Ginten, T. Penny, I. Richardson and Q. Russel. "Integrity Management of Stress Corrosion Cracking in Pipelines – an Integrated Approach". Pipeline Inspection Technical report ROSEN, Germany, 2014.
[8] K. Reber, M. Beller, "Ultrasonic in-line inspection tools to inspect older pipelines for cracks in girth and long-seam welds". NDT Systems & Services AG, Stutensee, Germany, 2003.
[9] Cheng, W., Shiwa, H., Yoneyama, H., Huang, H., Takagi, T., Uchimoto, T., 2003. Ultrasonic and eddy current testing of defects in Inconel welding metals. In: Proceedings of the 12th MAGDA Conference, Oita, Japan, pp. 187–190.
[10] A. Badidi Bouda, S. Lebaili, A. Benchaala, Grain size influence on ultrasonic velocities and attenuation, NDT & E International, Volume 36, Issue 1, 2003, Pages 1-5, ISSN 0963-8695, doi.org/10.1016/S0963-8695(02)00043-9.
[11] Yusa, Noritaka ., Machida, Eiji, Janousek, Ladislav, Rebican, Mihai, Chen, Zhenmao, & Miya, Kenzo (2005). Application of eddy current inversion technique to the sizing of defects in Inconel welds with rough surfaces. Nuclear Engineering and Design, 235(14), 1469-1480. doi:101016/jnucengdes200501005
[12] N. Yusa, L. Janousek, Z. Chen and K. Miya, Diagnostics of stress corrosion and fatigue cracks using benchmark signals, Materials Letters, vol. 59, no. 28, pp. 3656-3659, 2005.
[13] Todorov E, et al. Inspection of laser welds with array eddy current. AIP Conference Proceedings. Vol. 1511, 2013, doi: https://doi.org/10.1063/1.4789161
[14] G. Martín, J.; Gómez-Gil, J.; Vázquez-Sánchez, E. Non-Destructive Techniques Based on Eddy Current Testing. Sensors 2011, 11, 2525-2565, doi:10.3390/s110302525
[15] H. Huang, N. Yusa, K. MIYA, Eddy current testing and sizing of fatigue cracks, 12th A-PCNDT 2006 – Asia-Pacific Conference on NDT, Auckland, New Zealand, 2006.
[16] D. Lamtenzan, G. Washer, and M. Lovez, Detection and Sizing of Cracks in Structural Steel Using the Eddy Current Method, U.S. Department of Transportation, Federal Highway Administration, Report No. FHWA-RD-00-018, November 2000
[17] Xie, R.; Chen, D.; Pan, M.; Tian, W.; Wu, X.; Zhou, W.; Tang, Y. Fatigue Crack Length Sizing Using a Novel Flexible Eddy Current Sensor Array. Sensors 2015, 15, 32138-32151.
[18] A. D. Watkins, D. C. Kunerth, "Eddy Current Examination of Spent Nuclear Fuel Canister Closure Welds" 2006 International High Level Radioactive Waste Management Conference (IHLRWM), Idaho 2006
[19] Tan , Li . Digital Signal Processing: Fundamentals and Applications, Elsevier, 831 p., 2008
[20] A. Barbian, M. Beller, S. Hartmann, U. Schneider, Resolution Ultrasonic In-Line Inspection: Added Value and Special Applications, 6th Pipeline Technology Conference, 2011

Abhishek Pandala[1], S. Shivaprasad[1]*, C.V. Krishnamurthy[1,2], Krishnan Balasubramaniam[1]
[1]*Centre for Non-Destructive Evaluation, Department of Mechanical Engineering, Indian Institute of Technology, Madras, Chennai, India*
[2]*Department of Physics, Indian Institute of Technology, Madras, Chennai, India*

Robust and efficient finite-difference-time-domain modelling of the propagation of nonlinear elastic waves

Niezawodne i wydajne modelowanie propagacji nieliniowych fal sprężystych metodą różnic skończonych w dziedzinie czasu

ABSTRACT

A robust finite-difference-time-domain (FDTD) scheme to model the non-linear elastic wave propagation in a homogeneous isotropic material is presented. A formulation based on rotated staggered grid scheme in a displacement-velocity-stress configuration incorporating both geometric and material nonlinearities is proposed. By adopting a Parsimonious algorithm, the computational memory requirement is reduced by 50%. Simulations are accelerated by exploiting massive data parallelism innate to the FDTD approach using parallel computation on Graphical Processing Units with NVIDIA CUDA's API. For the proposed numerical scheme, the grid convergence criterion and accuracy over propagating distances are investigated. The study is also extended to determine the contribution from geometric and material models at various input amplitude levels. The time and frequency domain signals obtained from the proposed scheme are verified with a commercial finite element solver. The simulation runtimes for an Aluminium sample of dimensions 20 mm x 10 mm using a 5 MHz pulse is of the order of one minute, which makes the proposed numerical scheme attractive to model nonlinear elastic waves in large domains.

Keywords: *Finite Difference Time Domain, Rotated Staggered Grid, Parsimonious Scheme, Nonlinear elastic waves, CUDA, GPU*

STRESZCZENIE

W artykule przedstawiono odporny schemat metody różnic skończonych w dziedzinie czasu (FDTD) do modelowania propagacji nieliniowych fal sprężystych w jednorodnym materiale izotropowym. Zaproponowano podejście oparte na rotowanych siatkach przestawnych w układzie przemieszczenie-prędkość-naprężenie obejmującym zarówno nieliniowość geometryczną, jak i materiałową. Zastosowanie algorytmu redukcji oszczędnej, zmniejszyło zapotrzebowanie na pamięć obliczeniową o 50%. Symulacje są przyspieszane przez wykorzystanie olbrzymiego paralelizmu danych wbudowanego w podejście FDTD z wykorzystaniem obliczeń równoległych na jednostkach przetwarzania graficznego (GPU) wyposażonych w interfejs API NVIDIA CUDA. Dla proponowanego schematu numerycznego badane jest kryterium zbieżności siatki i dokładność w funkcji odległości propagacji. Badanie rozszerzono również w celu określenia wkładu modeli geometrycznych i materiałowych na różnych poziomach amplitudy wejściowej. Sygnały w dziedzinie czasu i częstotliwości uzyskane z proponowanego schematu są weryfikowane za pomocą komercyjnego oprogramowania wykorzystującego metodę elementów skończonych. Czasy pracy dla symulacji propagacji impulsu o częstotliwości 5 MHz w próbce aluminium o wymiarach 20 mm x 10 mm są rzędu jednej minuty, co sprawia, że proponowany schemat liczbowy jest atrakcyjny dla modelowania nieliniowych fal sprężystych w dużych domenach.

Słowa kluczowe: *metoda różnic skończonych w dziedzinie czasu, rotowane siatki przestawne, schemat redukcji oszczędnej, nieliniowe fale sprężyste, CUDA, GPU*

1. Introduction

Interatomic forces that bind solids determine the responses to external forces. The interatomic potentials can be very well approximated as quadratic in displacements, for sufficiently small displacements of atoms from their equilibrium positions. As a result, the response to small external forces can be reasonably approximated to be linear in displacements. For microscopically homogeneous solids subject to small external forces, a description in terms of linear response would be a reasonable first approximation. However, there are a wide range of solids, natural and synthetic, that are not homogenous in a strict microscopic sense. Microscopically inhomogeneous features such as dislocations, grain boundaries, voids, micro-cracks, pores exist. Solids having these internal features are in reasonably stable equilibrium and may be described as macroscopically homogenous media in some average sense.

There exists considerable experimental evidence to indicate that such macroscopically homogeneous media respond nonlinearly to applied forces. Several of the examples of nonlinear effects reported in the literature include higher harmonics generation[1,2], resonance shift in frequency[3], amplitude-dependent and non-classical dissipation[4], DC response and subharmonic generation[5], wave modulation and frequency mixing[6]. Nonlinear acoustic and elastic waves have been investigated extensively for past few decades on grained materials[7], and rocks[8], in areas relating to geology[9], seismology[10], biophysics[11], biomedical engineering[12], lithotripsy and acoustic physiotherapy of soft tissues[13] and nondestructive testing of polycrystalline and composite media[14].

Historically, the nonlinear theories have been classified

*Correspondence author. E-mail: prsd.shiva@gmail.com

DOI: 10.26357/BNiD.2018.008

into two: classical theory, which accounts for the higher order elastic terms in the Hooke's law and the non-classical theory which includes mechanisms like stress-strain hysteresis and contact acoustic nonlinearities(CAN)[5].

Two types of classical nonlinearity have been reported in the literature[4,15,16], i.e. geometric (kinematic) and material (physical) nonlinearities. The former accounts for the gradient of the strain-displacement relation, whereas the latter is the result of the nonlinear stress-strain function (i.e. the third- and higher-order terms in elastic energy). The contribution of geometrical nonlinearity in solids has been known to be much smaller than the material nonlinearity, and, hence, has usually been neglected[17].

Among the various applications of nonlinear acoustic and elastic waves described earlier, the most exciting potential is believed to be in characterising materials nondestructively. In last few decades, researchers have been able to experimentally relate the acoustic nonlinearity parameter, β with microscopically inhomogeneous features such as dislocations, grain boundaries, precipitates, voids, micro-cracks formed due to various damages mechanism like fatigue, creep, thermal aging and radiation damage which can be related to the third-order elastic(TOE) constants[18,19].

The majority of literature deals with the experimental determination of the nonlinearity parameter using harmonic generation technique. The non-linearity parameter obtained from experiments is the combined effect of many microscopic factors as well as instrumentation non-linearity. The individual contribution of each of the microscopic factors to the non-linearity parameter is not entirely understood. Numerical simulations can provide a better insight into nonlinear wave characteristics by allowing for the study of individual contributions to non-linearity. A variety of numerical methods have been employed for examining the nonlinear wave propagation through homogeneous isotropic media, including the finite element (FE) method [20–23], the elastodynamic finite integration technique[24] and the finite difference(FD) method[25,26]. Researchers in the past have mostly resorted to various commercially available explicit/implicit FE solvers for dealing with such problems. For instance, Chillara and Lissenden [20] solved a two-dimensional FE model using the implicit solver, while Rauter and Lammering[22] and Xiang et al. [23] adopted an explicit solver, all of them incorporating TOE constants to account for the nonlinear effects. Drewry and Wilcox[21] on the other hand, looked at computationally less intensive one-dimensional FE models, underlining various signal processing protocols for obtaining the quantitative value of nonlinearity parameter. Commercial software packages based on FEM are memory intensive. Implicit solvers are also CPU time intensive as the computational domain increases.

Little work has been done in the past to develop finite difference time domain(FDTD) numerical models for elastic wave propagation through nonlinear media. Matsuda and Biwa [25,26] proposed a two-dimensional finite difference time domain(FDTD) model using a Standard Staggered Grid(SSG)[27,28] by incorporating both geometric and material nonlinearities. For anisotropic as well as nonlinear media, SSG requires interpolation of stress and strain [25]. The rotated staggered grid(RSG) FDTD scheme[29] overcomes this shortcoming by placing the density and material parameters at the same location corresponding to velocity and stress components respectively. There have been efforts in the past to exploit the graphics processing cards to accelerate simulations for linear elastodynamic problems [30–33].

The scope of the present work is to develop a robust and time-efficient two-dimensional RSG-FDTD scheme capable of modelling the non-linear response of the material while exploiting massive data parallelism innate to the FDTD approach. A formulation to deal with finite amplitude wave propagation based on FDTD method considering both the geometric and material nonlinearities is presented here. The geometric nonlinear model adopts a Signorini's model[34], while the complete nonlinear model considers Lagrangian stress and strain tensors, accounting for both geometric and material nonlinearity. The gridding convergence requirements to capture the higher harmonics components are presented. Signal stability as a function of propagation distance, evolution of higher harmonics with input amplitude as well as with propagation distance are described. The time and frequency domain signals obtained from the proposed scheme are verified with the commercial FE solver. The article has been organised as follows. Section 2 presents the theoretical formulation of nonlinear wave propagation. Section 3 explains the FDTD scheme implemented in this study. Section 4 describes the numerical model, grid convergence and propagation aspects. The results are discussed in Section 5 and conclusions are presented in Section 6.

Tab. 1. Different models presented in this study
Tab. 1. Różne modele przedstawiane w niniejszej pracy

Model	Strain Measure	Elastic Constants
Linear Elastic (LIN)	Cauchy Strain	Second Order
Geometric Nonlinear (GNL)	Almansi Hamel Strain	Second Order
Material Nonlinear (MNL)	Lagrangian Strain	Second and third Order

2. Non-Linear Elastodynamics - Theoretical Formulations

We consider three different models for the present study. First, a linear elastic model (LIN) is used considering Cauchy strain as the strain measure coupled with second-order elastic constants. Second, geometric nonlinear model (GNL) is introduced by adopting Signorini's model[34] relating finite strain tensor and Cauchy's stress tensor which is coupled with second-order elastic constants. Third, a complete nonlinear model comprising both geometric and material nonlinearity called Material Nonlinear model(MNL) is used. Here, the Lagrangian strain is used as the strain measure and is combined with second and third order elastic constants. The models considered in this study are shown in Table 1.

2.1 Linear Elastic Model

In this model, a linear relationship between stress and strain is assumed and Cauchy strain is used as the strain

measure [35]. The linearized strain tensor is,

$$\varepsilon_{ij} = \frac{1}{2}\left(u_{i,j} + u_{j,i}\right) \quad (1)$$

where ε_{ij} is the strain, u_i is the displacement and $u_{i,j} = \frac{\partial u_i}{\partial u_j}$.

Following the constitutive relationship for elastic isotropic solids we have,

$$\sigma = 2\mu\varepsilon + \lambda\, tr(\varepsilon) I \quad (2)$$

The simplified constitutive equations turn out to be

$$\tau_{xx} = \left(\lambda + 2\mu\right) u_{x,x} + \left(\lambda\right) u_{z,z} \quad (3)$$

$$\tau_{zz} = \left(\lambda + 2\mu\right) u_{z,z} + \left(\lambda\right) u_{x,x} \quad (4)$$

$$\tau_{xz} = \tau_{zx} = \mu\left(u_{x,z} + u_{z,x}\right) \quad (5)$$

where λ and μ are the Lame elastic constants and τ_{ij} is the stress.

2.2 Geometric Nonlinear Model

Here, instead of the linearized strain, a finite strain tensor is used here. Signorini's model[34] relating the finite strain tensor (Almasi-Hamel strain) and Cauchy's stress tensor is employed in this formulation. The third order elastic constants are not considered. The finite strain tensor in terms of displacement gradient is,

$$\varepsilon_{ij} = \frac{1}{2}\left(u_{i,j} + u_{j,i} - u_{k,i}u_{k,j}\right) \quad (6)$$

The constitutive equations concerning two-dimensional non-linear wave propagation following[36] are,

$$\tau_{xx} = \frac{\lambda + 2\mu}{2}\left[2u_{x,x} - {u_{x,x}}^2 - {u_{z,x}}^2\right] + \frac{\lambda}{2}\left[2u_{z,z} - {u_{x,z}}^2 - {u_{z,z}}^2\right] \quad (7)$$

$$\tau_{zz} = \frac{\lambda + 2\mu}{2}\left[2u_{z,z} - {u_{x,z}}^2 - {u_{z,z}}^2\right] + \frac{\lambda}{2}\left[2u_{x,x} - {u_{x,x}}^2 - {u_{z,x}}^2\right] \quad (8)$$

$$\tau_{xz} = \tau_{zx} = \mu\left[u_{x,z} + u_{z,x} - u_{x,x}u_{x,z} - u_{z,x}u_{z,z}\right] \quad (9)$$

2.3 Material Nonlinear Model

For the Material Nonlinear model, the governing equations of motion, the displacement – velocity relation, and the stress- strain relation can be written by[15]

$$\rho\frac{\partial v_i}{\partial t} = \frac{\partial P_{ij}}{\partial X_j} \quad (10)$$

$$\frac{\partial u_i}{\partial t} = v_i \quad (11)$$

$$P_{ij} = C_{ijkl}\frac{\partial u_k}{\partial X_l} + \frac{1}{2}\left(C_{ijklmn} + C_{ijln}\delta_{km} + C_{jnkl}\delta_{im} + C_{jlmn}\delta_{ik}\right)\frac{\partial u_k}{\partial X_l}\frac{\partial u_m}{\partial X_n} \quad (12)$$

where X_i is the Lagragian coordinates, v_i the velocities and P_{ij} are the components of the nonsymmetric first Piola-Kirchoff stress tensor. For an isotropic material, the second- and third-order stiffness tensors are given as,

$$C_{ijkl} = \lambda\delta_{ij}\delta_{kl} + 2\mu I_{ijkl} \quad (13)$$

$$C_{ijklmn} = \frac{A}{2}\left(\delta_{ik}I_{jlmn} + \delta_{il}I_{jkmn} + \delta_{jk}I_{ilmn} + \delta_{jl}I_{ikmn}\right) + 2B\left(\delta_{ij}I_{klmn} + \delta_{kl}I_{mnij} + \delta_{mn}I_{ijkl}\right) + 2C\delta_{ij}\delta_{kl}\delta_{mn} \quad (14)$$

where *A, B* and *C* are the third-order elastic constants for an isotropic material following Landau and Lifshitz[37], δ_{ij} is the Kronecker's delta function and $I_{ijkl} = \frac{1}{2}\left(\delta_{ik}\delta_{jl} + \delta_{il}\delta_{jk}\right)$

In simplified terms, equation (12) can be expressed as

$$\tau_{xx} = (\lambda + 2\mu)u_{x,x} + (\lambda)u_{z,z} + d_1(u_{x,x})^2 + d_2(2u_{x,x} + u_{z,z})u_{z,z} + d_3(u_{x,z}{}^2 + u_{z,x}^2) + d_4(u_{x,z}u_{z,x}) \quad (15)$$

$$\tau_{zz} = (\lambda + 2\mu)u_{z,z} + (\lambda)u_{x,x} + d_1(u_{z,z})^2 + d_2(2u_{z,z} + u_{x,x})u_{x,x} + d_3(u_{x,z}{}^2 + u_{z,x}^2) + d_4(u_{x,z}u_{z,x}) \quad (16)$$

$$\tau_{xz} = \mu\left(u_{x,z} + u_{z,x}\right) + \left(u_{x,x} + u_{z,z}\right)\left(2d_3u_{x,z} + d_4u_{z,x}\right) \quad (17)$$

$$\tau_{zx} = \mu\left(u_{x,z} + u_{z,x}\right) + \left(u_{x,x} + u_{z,z}\right)\left(2d_3u_{z,x} + d_4u_{x,z}\right) \quad (18)$$

where,

$$d_1 = \frac{3}{2}\lambda + 3\mu + A + 3B + C\,;\, d_2 = \frac{1}{2}\lambda + B + C$$

$$d_3 = \frac{1}{2}\lambda + \mu + \frac{1}{4}A + \frac{1}{2}B\,;\, d_4 = \mu + \frac{1}{2}A + B \quad (19)$$

It is to be noted that the stress tensor in the case of material nonlinearity is not symmetric. The elastodynamic equations for two-dimensional problem, in the absence of body forces, are given by,

$$\rho\dot{v}_x = \tau_{xx,x} + \tau_{xz,z} \quad (20)$$

$$\rho\dot{v}_z = \tau_{zx,x} + \tau_{zz,z} \quad (21)$$

$$v_x = \dot{u}_x \quad (22)$$

$$v_z = \dot{u}_z \quad (23)$$

3. Finite Difference Time Domain (FDTD) Formulation

3.1 Rotated Staggered Scheme (RSG)

In this section, the 2D Heterogeneous Explicit Parsimonious Rotated Staggered Grid Scheme is described. The RSG finite difference scheme was proposed by Saenger et al. [29], and it has been successfully applied in seismic modelling of elastic, viscoelastic, isotropic and anisotropic media[38]. In the RSG unit cell, all the velocity (and displacement) components are at the same location and the stress components at the other location (see Figure 1). Correspondingly, density is located at the same position as velocity and material parameters are located at the same position as stress. This gridding scheme is advantageous in modelling non-linear response of materials as well as anisotropic crystal systems with symmetry less than Orthotropic. It is to be noted that non-linearity and anisotropy of a material can also be modelled using the Standard Staggered Grid(SSG) [27,28], but requires interpolation of components[25,39]. The present scheme is also numerically stable with the existence of high contrast heterogeneities like voids, cracks, inclusions and the presence of more than one medium (fluid-solid contact). The application of boundary condition whether welded interface or free-surface boundary condition, is straightforward in the heterogeneous formulation of the RSG Scheme. The major disadvantage of using RSG scheme is a stricter grid dispersion criterion, i.e., a higher sampling ratio is needed to achieve the same level of accuracy as obtained by a conventional SSG [40]. This leads to increased computational memory requirements and consequently large simulation times. Both these issues are addressed in this article by adopting a Parsimonious scheme and accelerating the simulations on Graphical Processing Units respectively.

Compared to the SSG scheme, the RSG method rotates the finite differential operators to the elementary cell in the diagonal directions first, and then, the standard FD operator is calculated by the linear combination of these operators. A detailed description of the RSG scheme can be found in

ref.[29]. We adopt a second order update in space and first-order update in time. The extension to higher order spatial derivatives is straightforward.

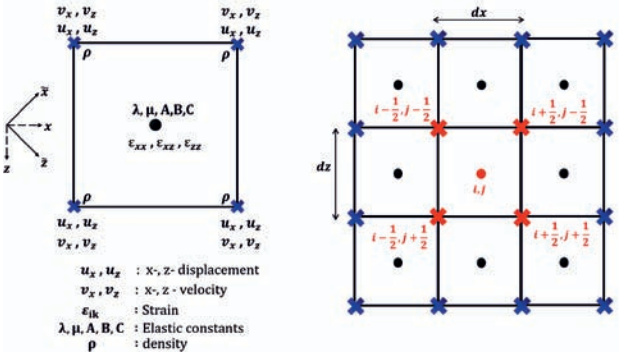

Fig. 1. Rotated Staggered gridding scheme
Rys. 1. Schemat obróconej siatki przestawnej

3.2 Parsimonious Scheme

There are various numerical formulations of the above governing equations: Velocity-stress, Displacement-Velocity-Stress, Displacement-Stress and Displacement-Displacement [41]. We develop an algorithm by adapting a Displacement-Velocity-Stress (DVS) scheme. The proposed scheme is staggered in time where displacements are stored at integral timesteps and velocities are stored at half-integral timesteps leading to a recursive time-marching algorithm (as shown in Figure 2). Equations (3-5), (7-9) and (15-18) are used to compute the stress values from displacement at integral timesteps. Equations (20-21) are used to update the velocities at half timesteps from the stress values, and finally, Equations (22-23) are used to evaluate displacement at the next integral timestep. In order to reduce the computational memory requirement, we employ the parsimonious staggered grid [42][43]. It is not a gridding scheme in itself, but rather an algorithm to reduce computational memory requirement. Since in the DVS formulation, no temporal derivatives involving stress exist, there is no need to store stress tensor components for successive timesteps. This is the prime reason for parsimony. The scheme necessitates storing only displacement components and velocity components reducing the computational memory to 50%.

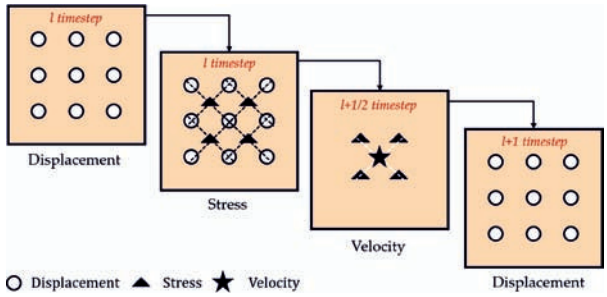

Fig. 2. Parsimonious gridding scheme
Rys. 2. Schemat redukcji oszczędnej

Stress components are evaluated but not stored for subsequent timesteps. The parsimonious scheme has memory requirements similar to that of a collocated grid [44] but exploits the numerical stability and accuracy of a complete[27] and partial staggered grid[29]. The bottleneck is that programming is much more involved and redundant computations are performed between adjacent grid points increasing the computational time. This increase in computational time is compensated by performing parallel computations on Graphical Processing Units exploiting the massive data parallelism innate to the FDTD approach. A complete set of discretized FD equations for geometric and material nonlinearity can be found in Appendix.

3.3 Parallel Computing- Efficient simulation using GPU

The numerical scheme outlined in the previous section is implemented through the use of Compute Unified Device Architecture (CUDA)[45], an Application Programming Interface(API) and a parallel computing platform, to leverage graphical processing units(GPU) capabilities. CUDA provides transparent access to the GPU hardware at a low level while minimising the programming complexity and the attainable efficiency was demonstrated with an FDTD case study performed by Pandala et.al [46], wherein a speed improvement of up to seventy times was reported in comparison with computer processing units(CPU). The authors also have earlier explored the capability to use CUDA based acceleration for linear wave propagation through the polycrystalline material for both two and three-dimensional models[47]. In the present scheme, in order to retain the information between successive timesteps, the two sets of displacement and velocity components are stored as global variables. The stress components are evaluated at individual grid points as local variables. The use of shared memory does not provide any acceleration as there is zero redundancy in memory transactions. All the computations have been carried out with NVIDIA Tesla K40C graphics card.

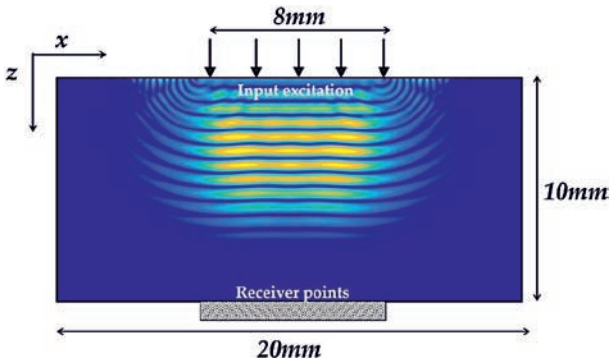

Fig. 3. Snapshot and Schematic diagram of a model for nonlinear elastic wave propagation.
Rys. 3. Schematyczne przedstawienie modelu do propagacji nieliniowej fali sprężystej

4. Numerical Modelling

4.1 Scheme

An FDTD simulation was carried out on a domain having dimension 20 mm x 10 mm. A Hann windowed tone burst signal of 5 MHz centre frequency with eight

cycles was imposed from the top surface of the domain. Hann windowed signal is known to produce significantly lower amplitudes (80dB) at the frequencies of harmonics of interest[21]. Through transmitted signal was received from the other end of the domain as shown in the schematic diagram in Figure 3. The length of the modelling domain was adjusted to isolate the first arrived signal from the side wall reflections at the receiver. The material properties used are for aluminium and are given in Table 2.[48].

Tab. 2. Material Properties used for Aluminum[48]
Tab. 2. Właściwości materiałowe aluminium [48]

Material	Aluminum
ρ	2727 kg/m^3
λ	57.0 GPa
μ	27 GPa
A	-320 GPa
B	-200 GPa
C	-190 GPa

4.2 Gridding

It is known that RSG scheme requires at least 15 grid points per wavelength to avoid numerical dispersion and provide reasonable accuracy [40]. This criterion has been deduced from linear wave propagation considerations. It needs to be re-examined while dealing with nonlinear wave propagation involving generation of higher harmonic components. In the present study, we investigate the spatial sampling requirements to ensure sufficient modelling accuracy to extract up to third harmonics components from the numerical model. For the domain given in Figure 3, numerical simulation was performed for both GNL and MNL models by varying the grid point per wavelength as indicated in Figure 4. The peak amplitude of excitation here was set to 10^{-7}m. The received time domain signal was Fast Fourier transformed to extract the amplitudes of static, second and third harmonic components. Typical input and received time domain signal along with the corresponding frequency spectra are shown in Figure 5.

The grid convergence was obtained by calculating the difference between the amplitudes of individual harmonic component (i.e. static(A0), second(A2) and third(A3) harmonic component) to that of the converged solution Ac. The converged solution is obtained at the highest mesh density, in this case at λ/50. From, Figure 4 (a), for GNL model, it can be seen that both second harmonic and static displacement components converge beyond 30 grid points per wavelength. The presence of third harmonic components in this model was found to be minimal throughout and has hence been ignored from the present analysis and rest of the article. Figure 4 (b), which is for MNL, converges beyond 45 grids per wavelength. As static displacement component converges much earlier, ensuring the convergence for third harmonics will ensure sufficient sampling for static displacement components. General criteria for gridding and time stepping for GNL and MNL model is given in equation (24), (25) and (26)

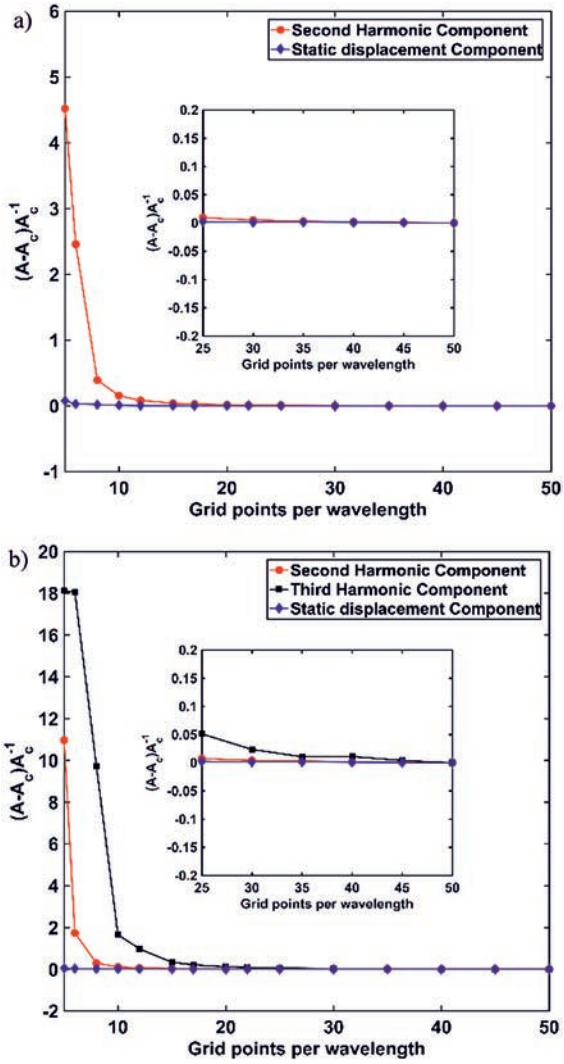

Fig. 4. Convergence of normalised harmonic amplitude against number of grid points per wavelength obtained for (a) GNL and (b) MNL models. A zoomed view of the graph near to the converging point is shown in the inset image. Results are presented for static displacement (blue diamond marker), second harmonic (red circular marker) and third harmonic component (black square marker).

Rys. 4. Zbieżność znormalizowanej amplitudy harmonicznej w funkcji liczby punktów siatki przypadających na długość fali, uzyskana dla modeli: (a) GNL, (b) MNL. W powiększeniu pokazano widok wykresu w pobliżu punktu zbieżności. Wyniki przedstawiono dla przemieszczenia statycznego (niebieski znacznik diamentowy), drugiej harmonicznej (czerwony znacznik kołowy) i trzeciej harmonicznej (czarny znacznik kwadratowy).

$$\lambda = \frac{V_{Lomgitudinal}}{f} \tag{24}$$

$$\Delta x = \Delta z = dh = \frac{1}{2} \times \left(\frac{\lambda}{15}\right)(GNL) \quad or \quad \frac{1}{3} \times \left(\frac{\lambda}{15}\right)(MNL) \tag{25}$$

$$\Delta t \leq \frac{\Delta h}{V_L \sum_{k=1}^{n} |c_k|} \tag{26}$$

where V_L is the longitudinal velocity in the material, λ is the longitudinal wavelength, Δh is the gridding, c_k represents difference coefficients(e.g. Holberg Coefficients[49]).

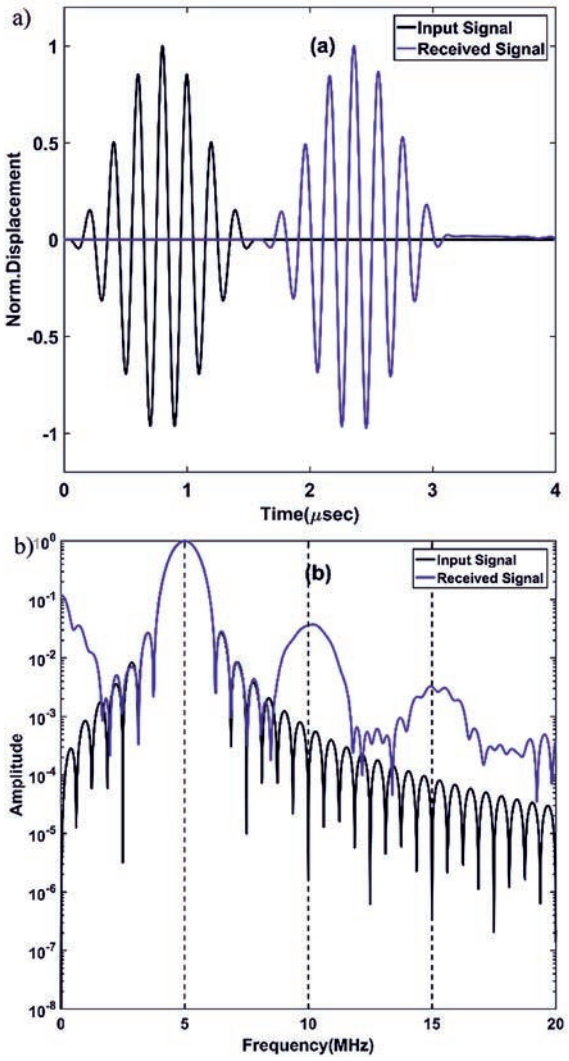

Fig. 5. (a) Typical input excitation and received A-scan signal (normalized) (a) corresponding FFT signal (normalized)
Rys. 5. Typowy znormalizowany sygnał wzbudzenia i wyjściowy: (a) w dziedzinie czasu (sygnał typu A) (b) w dziedzinie częstotliwości

4.3 Propagation Aspects

The solution to the nonlinear ultrasonic wave equation, based on an input harmonic wave train, has been deduced in numerous articles published earlier [15,19,21,50] and hence will not be repeated here. The expression for second harmonic nonlinear response (β) is given by

$$\beta = \frac{8v^2 A_2}{\omega^2 z A_1^2} \qquad A_2 \propto z A_1^2 \tag{27}$$

where β is the second-order nonlinear parameter, v is the longitudinal wave velocity of the material, ω is the angular frequency, z is the thickness of the material, A_1 is the fundamental amplitude, A_2 is the second harmonic amplitude.

Similarly, the third harmonic nonlinear parameter and the static displacement nonlinear parameter are given in Eq. (28) and (29)

$$\delta = \frac{24v^3 A_3}{\omega^3 z A_1^3} \qquad A_3 \propto z A_1^3 \tag{28}$$

$$\beta_{dc} = \frac{24v^2 A_{dc}}{\omega^2 z A_1^2} \qquad A_{dc} \propto z A_1^2 \tag{29}$$

where δ is the third order nonlinear parameter, β_{dc} is the static displacement nonlinear parameter, A_{dc} is the static displacement amplitude, A_3 is the third harmonic amplitude.

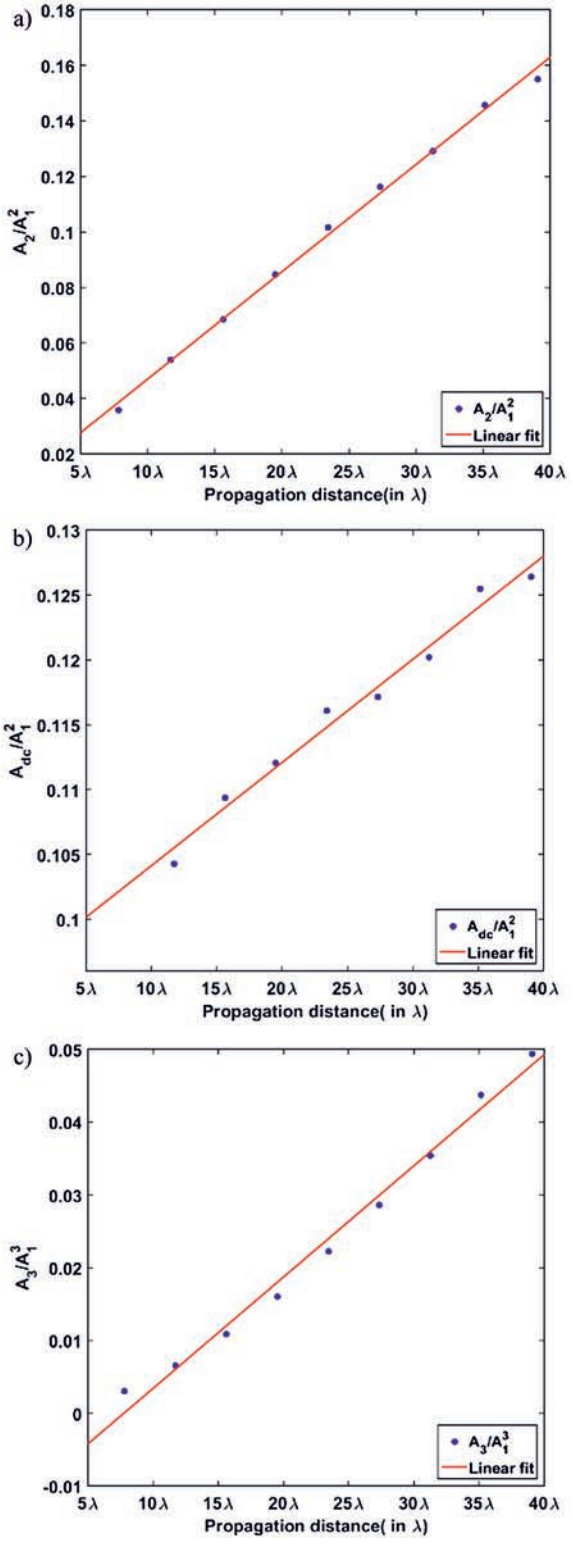

Fig. 6. Variation of (a) A_2/A_1^2, (b) A_{dc}/A_1^2 and (c) A_3/A_1^3 with propagation distance for MNL model
Rys. 6. Zależność (a) A_2/A_1^2, (b) A_{dc}/A_1^2, (c) A_3/A_1^3 od odległości dla modelu MNL

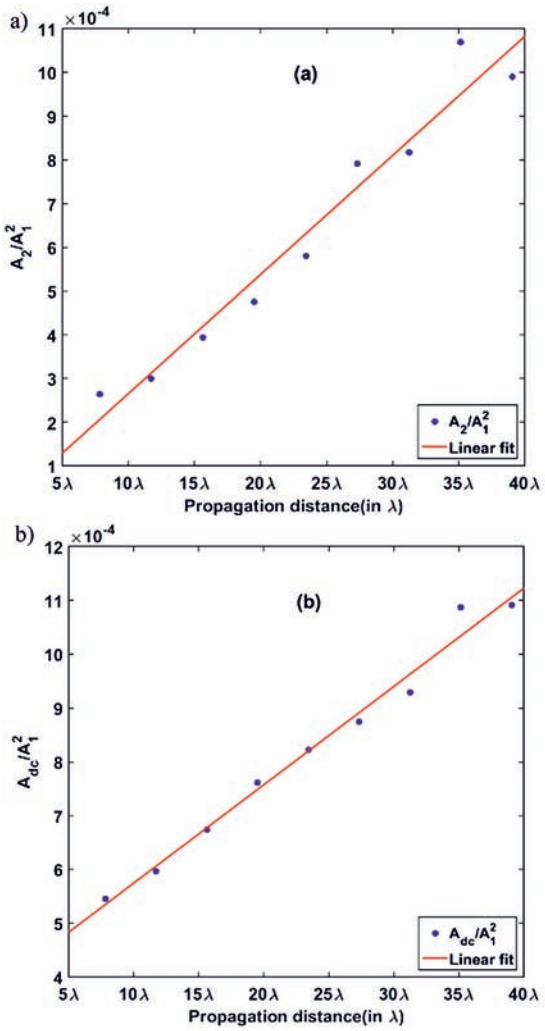

Fig. 7. Variation of (a) A_2/A_1^2 and (b) A_{dc}/A_1^2 with propagation distance for GNL model
Rys. 7. Zależność (a) A_2/A_1^2, (b) A_{dc}/A_1^2 od odległości dla modelu MNL

The stability and accuracy of the proposed FDTD model for nonlinear elastic media are demonstrated by performing simulation on medium with varying propagation distances using both the GNL and MNL models. It is expected from relations (27), (28) and (29) that the relative amplitude ratio, defined by A_2/A_1^2, A_{dc}/A_1^2 and A_3/A_1^3 would vary linearly over the propagation distances. The modelling parameters for this study have been kept similar to that mentioned in Section 4.1 while the propagation distance was varied from 10 mm to 50 mm. The frequency domain plots obtained for GNL and MNL models were individually normalised with respect to their corresponding amplitudes of the fundamental (A_1) and amplitudes corresponding to static, second and third harmonic components were extracted. This normalisation permits comparisons between the responses from different nonlinear models. The variation of A_2/A_1^2, A_{dc}/A_1^2 and A_3/A_1^3 with propagation distance for MNL model is shown in Figure 6. A similar plot for A_2/A_1^2 and A_{dc}/A_1^2 evaluated using the GNL model is shown in Figure 7. The linear trend indicates that the nonlinear effect captured by the numerical scheme is consistent with the theoretical expression for all three nonlinear parameters given in Eq. (27), (28) and (29) As mentioned earlier, the contribution from third harmonics generated from GNL model was found to be negligibly small at the given input amplitude level and has been ignored from the analysis detailed in this section.

5. Results and discussions

5.1 Verification of FDTD model

We compare the MNL-FDTD model with an FE model implemented using a commercial software package, COMSOL Multiphysics 5.2 [51]. This commercial software package runs on an implicit solver and adopts a straightforward implementation of third-order elastic constants (TOEC's). In contrast, our FDTD model employs an explicit scheme, and the objective here is to draw a comparison in terms of the accuracy of the solution, as such packages have been widely utilised for the nonlinear wave propagation studies[20, 52, 53].The modelling parameters are kept identical for both the models and are shown in Table 2 and Table.3. The peak amplitude of input excitation was set of 10^{-7}m. Figure 8.(a) shows the time domain and FFT signal drawing a comparison between the FE and FDTD model. It can be seen that the time domain signals shows good agreement with each other showing a discrepancy within 1%. The FFT shown in Figure 8. (b) also indicates good agreement with the FE Model for static components, second harmonic and third harmonic components showing the differences to be less than 1% for the peak amplitudes. The simulation time for the FDTD model given in Table 3, was of the order of one minute, while the memory intensive model having a dimension 20 mm x 50 mm with 5MHz input frequency took 6 minutes.

Tab. 3. Simulation parameters used for comparing FE and FDTD models.
Tab. 3. Parametry symulacji używane do porównywania modeli FE i FDTD

	FE Model	F DTD Model
Model dimension	20 mm x 10 mm	
Input frequency/Number of cycles	5 MHz/ 8 cycles	
Step time/Gridding	3.4e-9sec / $\lambda_{longitudinal}$/45	

5.2 Comparison of Linear, GNL and MNL models

The amplitude of input displacement considered here is in the order of 10^{-7}m. Figure 9. (a) compares the time domain signal received for the three models. It can be seen that all the three models overlap with each other to a greater extent, while some fluctuations can be observed beyond the first arrived signal in case of MNL model (shown in the inset in Figure 9. (b)). This could indicate the presence of higher harmonic components as reported in Fig.7 of [20]. The frequency spectra shown in Figure 9. (c) indicate a higher harmonic contribution from MNL than GNL. Similar trends have been reported in the numerical model presented by Chillara and Lissenden [20].

The study was extended to investigate into the responses of the harmonic components by varying the input amplitude levels. Figure 10 shows frequency responses for MNL and GNL models, indicating consistent increment in the higher harmonic generation. At lower amplitude levels (in the order of 1e-9m), both GNL and MNL models, showed excellent

agreement with the linear elastic model, which indicates that noticeable harmonic components are generated only above certain finite amplitude levels. The static displacement component (or DC component) amplitudes are observed to be one order higher in MNL model in comparison with GNL model.

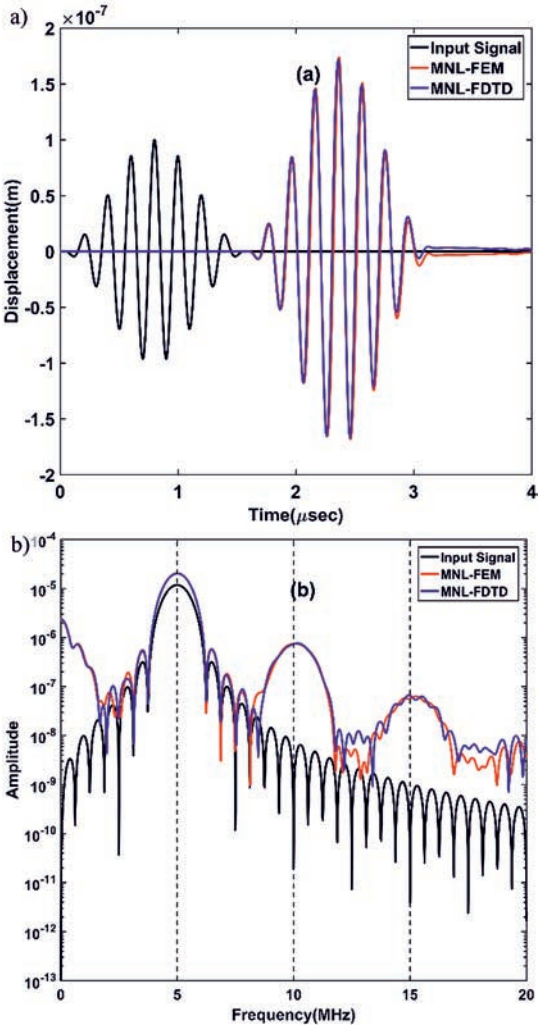

Fig. 8. Comparison of FEM and FDTD models with the input excitation signal (a) Time domain (b) FFT. Note the difference in the signal strength between input and output signal in the time domain are reflected in the FFT plot.

Rys. 8. Porównanie wyników modeli FEM i FDTD z wejściowym sygnałem wzbudzenia (a) w dziedzinie czasu (b) w dziedzinie częstotliwości. Uwaga: różnica w sile sygnału między sygnałem wejściowym i wyjściowym w dziedzinie czasu jest odzwierciedlona na wykresie widmowym.

6. Conclusions

The development of a robust numerical FDTD RSG scheme to deal with geometric and material nonlinearity in homogeneous isotropic materials has been described. The two bottlenecks of RSG scheme: large computational memory and extensive simulations times are addressed by adopting a Parsimonious scheme and parallelizing the time domain simulations on GPU with CUDA API. The simulation runtimes for the most memory-intensive test case of the FDTD model was of the order of six minutes. The study also provides the required spatial sampling to ensure sufficient modelling accuracy to extract up to third harmonics as a guideline for future modelling. The time and frequency domain signals obtained from the proposed scheme are verified with the commercial available FE solver showing a discrepancy within 1%. The amplitude of the harmonic contents extracted has shown linear behaviour with propagation distance, underlying the stability and accuracy of the proposed modelling scheme. It is observed that the contribution of MNL model dominates the GNL model at a given input amplitude level and both GNL and MNL model behaves similar to the linear model at smaller input amplitude levels, which are in agreement with the existing numerical predictions[20].

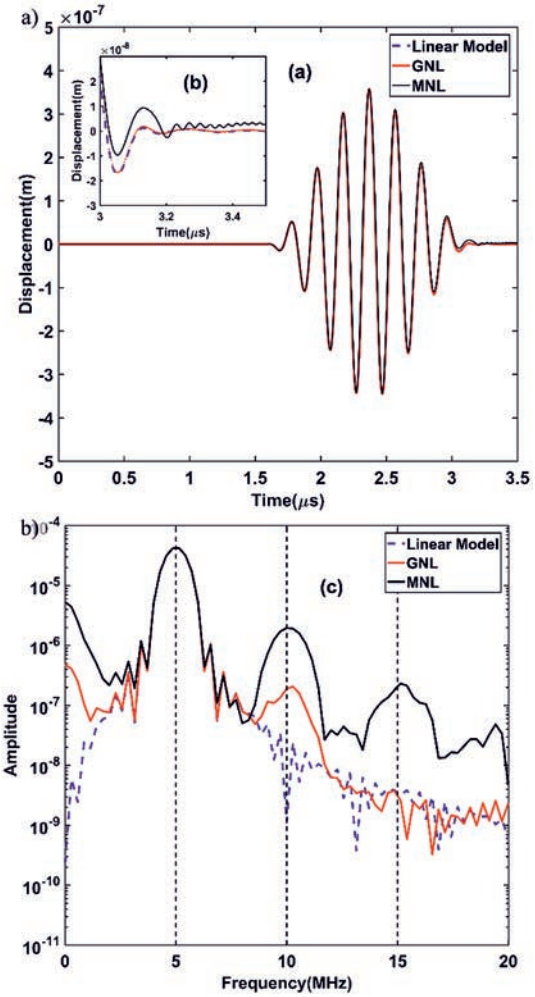

Fig. 9. Comparison of Response of Linear (blue dashed lines), GNL (red solid lines) and MNL (black solid lines) models for a peak to peak input excitation of the order 1e-7 m showing (a) Received time domain signal and (b) magnified view of the time domain signal shown in the inset shows the presence of extra frequency components (c) FFT of the received time domain signal for the corresponding models.

Rys. 9. Porównanie odpowiedzi modelu liniowego (niebieskie linie przerywane), GNL (czerwone linie ciągłe) i MNL (czarne linie ciągłe) dla wzbudzania wejściowego o wartości międzyszczytowej rzędu 10^{-7} m: (a) odebrany sygnał w dziedzinie czasu, (b) powiększony widok sygnału w dziedzinie czasu (obecność dodatkowych składowych częstotliwościowych), (c) wynik transformacji FFT odebranego sygnału dla badanych modeli.

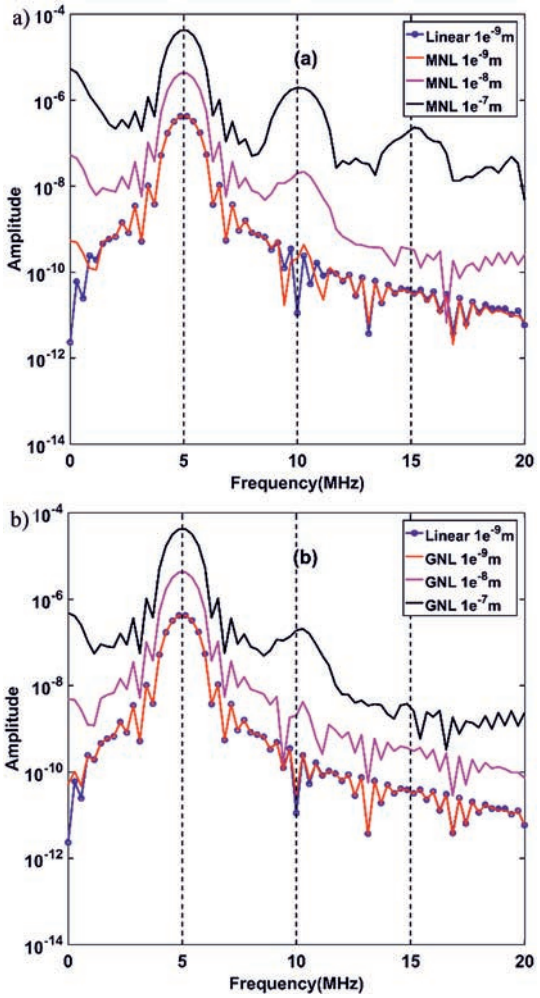

Fig. 10. Comparison of response of (a) Linear versus MNL (b) Linear versus GNL models for various orders of peak to peak input amplitudes. Results of the Linear models are shown in blue dashed lines with circular markers, and both MNL/GNL models are represented using solid lines.
Rys. 10. Porównanie odpowiedzi modeli dla różnych rzędów międzyszczytowej amplitudy sygnału wejściowego: (a) liniowy i MNL (b) liniowy i GNL. Wyniki modeli liniowych są przedstawione za pomocą niebieskich przerywanych linii z okrągłymi znacznikami, a oba modele MNL / GNL są reprezentowane za pomocą linii ciągłych.

As the RSG FDTD scheme is numerically stable with the existence of high contrast heterogeneities such as voids, cracks and inclusions, numerical investigation can be extended to understand the effect of microstructural inhomogeneities like micro-voids[54], micro-cracks, inclusions and precipitates[55] on acoustic nonlinearity parameter with appropriately measured second-order and third-order elastic constants[56].

Also, with the ability of RSG scheme to better handle anisotropic media, the current numerical scheme could also be adopted for studying the nonlinear wave propagation through polycrystalline media by incorporating the appropriate second and third-order elastic constants for each grain. The spatial sampling requirements derived earlier may not hold in this case, as grains are being often smaller compared to the probing wavelength, requiring much finer gridding than the aforementioned criteria.

7. References/Literatura

[1] M.A. Breazeale, D.O. Thompson, Finite-amplitude ultrasonic waves in aluminum, Appl. Phys. Lett. 3 (1963) 77–78. doi:10.1063/1.1753876.
[2] M.A. Breazeale, J. Ford, Ultrasonic studies of the nonlinear behavior of solids, J. Appl. Phys. 36 (1965) 3486–3490. doi:10.1063/1.1703023.
[3] P.A. Johnson, B. Zinszner, P.N.J. Rasolofosaon, Resonance and elastic nonlinear phenomena in rock, J. Geophys. Res. Solid Earth. 101 (1996) 11553–11564. doi:10.1029/96JB00647.
[4] L.A. Ostrovsky, P.A. Johnson, Dynamic nonlinear elasticity in geomaterials, Riv. Del. 24 (2001) 1–46. doi:10.1029/2002JB002038.
[5] I.Y. Solodov, N. Krohn, G. Busse, CAN: An example of nonclassical acoustic nonlinearity in solids, Ultrasonics. 40 (2002) 621–625. doi:10.1016/S0041-624X(02)00186-5.
[6] K.E.-A. Van Den Abeele, P.A. Johnson, A. Sutin, Nonlinear Elastic Wave Spectroscopy (NEWS) Techniques to Discern Material Damage, Part I: Nonlinear Wave Modulation Spectroscopy (NWMS), Res. Nondestruct. Eval. 12 (2000) 17–30. doi:10.1080/09349840009409646.
[7] G.D. Meegan, P.A. Johnson, R.A. Guyer, K.R. McCall, Observations of nonlinear elastic wave behavior in sandstone, J. Acoust. Soc. Am. 94 (1993) 3387–3391. doi:10.1121/1.407191.
[8] R.A. Guyer, K.R. McCall, K. Van Den Abeele, Slow elastic dynamics in a resonant bar of rock, Geophys. Res. Lett. 25 (1998) 1585–1588. doi:10.1029/98GL51231.
[9] E.H. Field, P.A. Johnson, I.A. Beresnev, Y. Zeng, Nonlinear ground-motion amplification by sediments during the 1994 Northridge earthquake, Nature. 390 (1997) 599–602. doi:10.1038/37586.
[10] R.A. Guyer, P.A. Johnson, The astonishing case of mesoscopic elastic nonlinearity, Phys. Today. 52 (1999) 30–35.
[11] R.T. Beyer, The Parameter B/A, in: D.. Hamilton, M. F. and Blackstrock (Ed.), Nonlinear Acoust., 1997: p. 25.
[12] B. Ward, A.C. Baker, V.F. Humphrey, Nonlinear propagation applied to the improvement of resolution in diagnostic medical ultrasound, J. Acoust. Soc. Am. 101 (1997) 143–154. doi:10.1121/1.417977.
[13] E.L. Carstensen, D.R. Bacon, Biomedical Applications, in: D.. Hamilton, M. F. and Blackstrock (Ed.), Nonlinear Acoust., 1997: p. 421.
[14] Y. Zheng, R.G. Maev, I.Y. Solodov, Nonlinear acoustic applications for material characterization: A review, Can. J. Phys. 77 (1999) 927–967. doi:10.1139/p99-059.
[15] A.N. Norris, Finite Amplitude waves in Solids, in: M. F. Hamilton and D. T. Blackstock (Ed.), Nonlinear Acoust., Academic press San Diego, 1998: pp. 263–277.
[16] V. Gusev, V. Tournat, B. Castagnède, Nonlinear Acoustic Phenomena in Micro-inhomogenous Media, in: Mater. Acoust. Handb., ISTE, 2009: pp. 431–471. doi:10.1002/9780470611609.ch17.
[17] O. V Rudenko, M.J. Crocker, Nonlinear Acoustics, in: Handb. Noise Vib. Control, John Wiley & Sons, Inc., 2007: pp. 159–168. doi:10.1002/9780470209707.ch10.
[18] Y. Zheng, R.G. Maev, I.Y. Solodov, Review / Syth?se Nonlinear acoustic applications for material characterization: A review, Can. J. Phys. 77 (2000) 927–967. doi:10.1139/p99-059.
[19] K.H. Matlack, J.Y. Kim, L.J. Jacobs, J. Qu, Review of Second Harmonic Generation Measurement Techniques for Material State Determination in Metals, J. Nondestruct. Eval. 34 (2015). doi:10.1007/s10921-014-0273-5.
[20] V.K. Chillara, C.J. Lissenden, Nonlinear guided waves in plates: A numerical perspective, Ultrasonics. 54 (2014) 1553–1558. doi:10.1016/j.ultras.2014.04.009.
[21] M.A. Drewry, P.D. Wilcox, One-dimensional time-domain finite-element modelling of nonlinear wave propagation for non-destructive evaluation, NDT E Int. 61 (2014) 45–52. doi:10.1016/j.ndteint.2013.09.006.

[22] N. Rauter, R. Lammering, Numerical simulation of elastic wave propagation in isotropic media considering material and geometrical nonlinearities, Smart Mater. Struct. 24 (2015) 45027. doi:10.1088/0964-1726/24/4/045027.
[23] Y.-X. Xiang, W.-J. Zhu, M.-X. Deng, F.-Z. Xuan, Experimental and numerical studies of nonlinear ultrasonic responses on plastic deformation in weld joints, Chinese Phys. B. 25 (2016) 24303. doi:10.1088/1674-1056/25/2/024303.
[24] F. Schubert, Numerical time-domain modeling of linear and nonlinear ultrasonic wave propagation using finite integration techniques--theory and applications., Ultrasonics. 42 (2004) 221–9. doi:10.1016/j.ultras.2004.01.013.
[25] N. Matsuda, S. Biwa, A Finite-Difference Time-Domain Technique for Nonlinear Elastic Media and Its Application to Nonlinear Lamb Wave Propagation, Jpn. J. Appl. Phys. 51 (2012) 07GB14. doi:10.1143/JJAP.51.07GB14.
[26] N. Matsuda, S. Biwa, Frequency dependence of second-harmonic generation in Lamb waves, J. Nondestruct. Eval. 33 (2014) 169–177. doi:10.1007/s10921-014-0227-y.
[27] J. Virieux, P-SV wave propagation in heterogeneous media:Velocitiy-stress finite difference method*, 51 (1986).
[28] J. Virieux, SH -wave propagation in heterogeneous media: Velocity-stress finite-difference method, GEOPHYSICS. 49 (1984) 1933–1942. doi:10.1190/1.1441605.
[29] E.H. Saenger, N. Gold, S. a. Shapiro, Modeling the propagation of elastic waves using a modified finite-difference grid, Wave Motion. 31 (2000) 77–92. doi:10.1016/S0165-2125(99)00023-2.
[30] H. Bao, J. Bielak, O. Ghattas, L.F. Kallivokas, D.R. O'Hallaron, J.R. Shewchuk, J. Xu, Large-scale simulation of elastic wave propagation in heterogeneous media on parallel computers, Comput. Methods Appl. Mech. Eng. 152 (1998) 85–102. doi:10.1016/S0045-7825(97)00183-7.
[31] D. Michéa, D. Komatitsch, Accelerating a three-dimensional finite-difference wave propagation code using GPU graphics cards, Geophys. J. Int. 182 (2010) 389–402. doi:10.1111/j.1365-246X.2010.04616.x.
[32] P. Huthwaite, Accelerated finite element elastodynamic simulations using the GPU, J. Comput. Phys. 257 (2014) 687–707. doi:10.1016/j.jcp.2013.10.017.
[33] P. Packo, T. Bielak, A.B. Spencer, T. Uhl, W.J. Staszewski, K. Worden, T. Barszcz, P. Russek, K. Wiatr, Numerical simulations of elastic wave propagation using graphical processing units—Comparative study of high-performance computing capabilities, Comput. Methods Appl. Mech. Eng. 290 (2015) 98–126. doi:10.1016/j.cma.2015.03.002.
[34] C. Truesdell, W. Noll, The Non-Linear Field Theories of Mechanics/Die Nicht-Linearen Feldtheorien der Mechanik, Springer Science & Business Media, 2013.
[35] J.L. Rose, Ultrasonic waves in solid media, Cambridge university press, 2004.
[36] R.S. Mini, Wave Propagation Through Microstructural Features with Geometric Nonlinearity- Experimental and Numerical Investigations, Indian Institute of Technology Madras, 2016.
[37] L.D. Landau, E.M. Lifshitz, A.M. Kosevich, L.P. Pitaevskiæi, Theory of Elasticity, 3rd, (1986).
[38] E.H. Saenger, T. Bohlen, Finite-difference modeling of viscoelastic and anisotropic wave propagation using the rotated staggered grid, Geophysics. 69 (2004) 583–591. doi:10.1190/1.1707078.
[39] H. Igel, P. Mora, B. Riollet, Anisotropic wave propagation through finite difference grids, GEOPHYSICS. 60 (1995) 1203–1216. doi:10.1190/1.1443849.
[40] V. Lisitsa, D. Vishnevskiy, Lebedev scheme for the numerical simulation of wave propagation in 3D anisotropic elasticity‡, Geophys. Prospect. 58 (2010) 619–635. doi:10.1111/j.1365-2478.2009.00862.x.
[41] P. Moczo, J. Kristek, E. Bystrický, Efficiency and optimization of the 3-D finite-difference modeling of seismic ground motion, J. Comput. Acoust. 9 (2001) 593–609.
[42] Y. Luo, G. Schuster, Parsimonuis staggered grid Finite-Differencing of the wave equation, Geophys. Res. Lett. 17 (1990) 155–158.
[43] J. Zhang, T. Liu, Elastic wave modelling in 3D heterogeneous media: 3D grid method, Geophys. J. Int. 150 (2002) 780–799. doi:10.1046/j.1365-246X.2002.01743.x.
[44] K.R. Kelly, R.W. Ward, S. Treitel, R.M. Alford, Synthetic Seismograms: A Finite Difference Approach, Geophysics. 41 (1976) 2–27. doi:10.1190/1.1440605.
[45] NVIDIA, CUDA C Programming guide, (n.d.). http://docs.nvidia.com/cuda/cuda-c-programming-guide/index.html.
[46] A. Pandala, K. Balasubramaniam, M. Spies, Simulation of Ultrasonic Inspection of Complex Components Using a 3D-FDTD-Approach, in: Proc. 19th WCNDT, 2016: pp. 3–10.
[47] A. Pandala, S. Shivaprasad, C. V Krishnamurthy, K. Balasubramaniam, Modelling of Elastic Wave Scattering in Polycrystalline Materials, in: 8th Int. Symp. NDT Aerosp., 2016.
[48] W.J.N. De Lima, M.F. Hamilton, Finite-amplitude waves in isotropic elastic plates, J. Sound Vib. 265 (2003) 819–839. doi:10.1016/S0022-460X(02)01260-9.
[49] O. Holberg, Computational Aspects Of The Choice Of Operator And Sampling Interval For Numerical Differentiation In Large-Scale Simulation Of Wave Phenomena, Geophys. Prospect. 35 (1987) 629–655. doi:10.1111/j.1365-2478.1987.tb00841.x.
[50] A. Hikata, B.B. Chick, C. Elbaum, Dislocation contribution to the second harmonic generation of ultrasonic waves, J. Appl. Phys. 36 (1965) 229–236. doi:10.1063/1.1713881.
[51] COMSOL, Introduction To COMSOL Multiphysics, (2016). cdn.comsol.com/documentation/5.2.0.166/IntroductionToCOMSOLMultiphysics.pdf.
[52] S. Delrue, K. Van Den Abeele, Three-dimensional finite element simulation of closed delaminations in composite materials, Ultrasonics. 52 (2012) 315–324. doi:10.1016/j.ultras.2011.09.001.
[53] J. Zhao, V.K. Chillara, B. Ren, H. Cho, J. Qiu, C.J. Lissenden, Second harmonic generation in composites: Theoretical and numerical analyses, J. Appl. Phys. 119 (2016) 64902. doi:10.1063/1.4941390.
[54] J.S. Valluri, K. Balasubramaniam, R. V. Prakash, Creep damage characterization using non-linear ultrasonic techniques, Acta Mater. 58 (2010) 2079–2090. doi:10.1016/j.actamat.2009.11.050.
[55] Y. Xiang, M. Deng, F.Z. Xuan, C.J. Liu, Effect of precipitate-dislocation interactions on generation of nonlinear Lamb waves in creep-damaged metallic alloys, J. Appl. Phys. 111 (2012). doi:10.1063/1.4720071.
[56] R.N. Thurston, K. Brugger, Third-Order Elastic Constants and the Velocity of Small Amplitude Elastic Waves in Homogeneously Stressed Media, Phys. Rev. 135 (1964) AB3-AB3. doi:10.1103/PhysRev.135.AB3.2.

8. Appendix

The following discretized equations are valid for interior of the solid. At the boundaries, the computation of velocity is performed by replacing the central finite differences with either forward (or backward) finite differences. The partial derivatives and represented by $\frac{\partial}{\partial x}$ and $\frac{\partial}{\partial z}$ are computed as follows

$$D_x P_{ik}^l = \frac{P_{i+1/2,k+1/2}^l - P_{i-1/2,k-1/2}^l + P_{i-1/2,k+1/2}^l - P_{i+1/2,k-1/2}^l}{2\Delta x} \quad (30)$$

$$D_z P_{ik}^l = \frac{P_{i+1/2,k+1/2}^l - P_{i-1/2,k-1/2}^l - P_{i-1/2,k+1/2}^l + P_{i+1/2,k-1/2}^l}{2\Delta z} \quad (31)$$

where P is the variable of interest, subscript $i = x,z$; $k = x,z$ and superscipt represents timesteps.

Geometric Nonlinearity

The complete set of discretized equations (7-9), (20-23) for geometric nonlinear model described in Section 2.2 are given by

$$\tau^{l}_{x|i,k} = \frac{\lambda+2\mu}{2}\left[2D_x u^{l}_{x|i,k} - \left(D_x u^{l}_{x|i,k}\right)^2 - \left(D_x u^{l}_{z|i,k}\right)^2\right] + \frac{\lambda}{2}\left[2D_z u^{l}_{z|i,k} - \left(D_z u^{l}_{x|i,k}\right)^2 - \left(D_z u^{l}_{z|i,k}\right)^2\right] \quad (32)$$

$$\tau^{l}_{xz|i,k} = \tau^{l}_{zx|i,k} = \mu\left[D_z u^{l}_{x|i,k} + D_x u^{l}_{z|i,k} - D_x u^{l}_{x|i,k} D_z u^{l}_{x\,i,k} - D_x u^{l}_{z|i,k} D_z u^{l}_{z|i,k}\right] \quad (33)$$

$$\tau^{l}_{xz|i,k} = \tau^{l}_{zx\,i,k} = \mu\left[D_z u^{l}_{x|i,k} + D_x u^{l}_{z|i,k} - D_x u^{l}_{x|i,k} D_z u^{l}_{x\,i,k} - D_x u^{l}_{z|i,k} D_z u^{l}_{z\,i,k}\right] \quad (34)$$

$$v^{l+1/2}_{x\,i,k} = v^{l-1/2}_{x|i,k} + (1/\rho)\left(D_x \tau^{l}_{xx|i,k} + D_x \tau^{l}_{xz|i,k}\right)$$

$$v^{l+1/2}_{z|i,k} = v^{l-1/2}_{z|i,k} + (1/\rho)\left(D_z \tau^{l}_{xz|i,k} + D_z \tau^{l}_{zz|i,k}\right) \quad (35)$$

$$u^{l+1}_{x|i,k} = u^{l}_{x|i,k} + dt\left(v^{l+1/2}_{x|i,k}\right) \quad (36)$$

$$u^{l+1}_{y|i,k} = u^{l}_{y|i,k} + dt\left(v^{l+1/2}_{y|i,k}\right) \quad (37)$$

Material Nonlinearity

The constitutive equations (15-18), elastodynamic equations (20-23) for material nonlinear model when discretized take the following form

$$\tau^{l}_{xx\,i,k} = c_{11} D_x u^{l}_{x|i,k} + c_{12} D_z u^{l}_{z|i,k} + d_1\left(D_x u^{l}_{x|i,k}\right)^2 + d_2\left(2D_x u^{l}_{x\,i,k} + D_z u^{l}_{z|i,k}\right) D_z u^{l}_{z\,i,k} + d_3\left(\left(D_z u^{l}_{z\,i,k}\right)^2 + \left(D_x u^{l}_{z|i,k}\right)^2\right) + d_4\left(D_z u^{l}_{x\,i,k} D_x u^{l}_{z|i,k}\right) \quad (38)$$

$$\tau^{l}_{zz|i,k} = c_{11} D_z u^{l}_{z|i,k} + c_{12} D_x u^{l}_{x|i,k} + d_1\left(D_z u^{l}_{z\,i,k}\right)^2 + d_2\left(2D_z u^{l}_{z\,i,k} + D_x u^{l}_{x|i,k}\right) D_x u^{l}_{x\,i,k} + d_3\left(\left(D_z u^{l}_{z|i,k}\right)^2 + \left(D_x u^{l}_{x|i,k}\right)^2\right) + d_4\left(D_z u^{l}_{x\,i,k} D_x u^{l}_{z|i,k}\right) \quad (39)$$

$$\tau^{l}_{xz\,i,k} = c_{44}\left(D_z u^{l}_{x|i,k} + D_x u^{l}_{z\,i,k}\right) + \left(D_x u^{l}_{x\,i,k} + D_z u^{l}_{z\,i,k}\right)\left(2d_3 D_z u^{l}_{x|i,k} + d_4 D_x u^{l}_{z\,i,k}\right) \quad (40)$$

$$\tau^{l}_{zx\,i,k} = c_{44}\left(D_z u^{l}_{x|i,k} + D_x u^{l}_{z\,i,k}\right) + \left(D_x u^{l}_{x\,i,k} + D_z u^{l}_{z|i,k}\right)\left(2d_3 D_x u^{l}_{z|i,k} + d_4 D_z u^{l}_{x\,i,k}\right) \quad (41)$$

$$v^{l+1/2}_{x\,i,k} = v^{l-1/2}_{x|i,k} + (1/\rho)\left(D_x \tau^{l}_{xx|i,k} + D_x \tau^{l}_{xz|i,k}\right) \quad (42)$$

$$v^{l+1/2}_{z|i,k} = v^{l-1/2}_{z|i,k} + (1/\rho)\left(D_z \tau^{l}_{zx|i,k} + D_z \tau^{l}_{zz|i,k}\right) \quad (43)$$

$$u^{l+1}_{x|i,k} = u^{l}_{x|i,k} + dt\left(v^{l+1/2}_{x|i,k}\right) \quad (44)$$

$$u^{l+1}_{y|i,k} = u^{l}_{y|i,k} + dt\left(v^{l+1/2}_{y\,i,k}\right) \quad (45)$$

Przemysław Łopato

Notatka z wyborów PTBNiDT SIMP

W dniu 9 maja 2018 roku w Domu Technika NOT w Warszawie odbyło się Walne Zebranie Sprawozdawczo-Wyborcze Delegatów Polskiego Towarzystwa Badań Nieniszczących i Diagnostyki Technicznej SIMP. W zebraniu wzięło udział 19 delegatów wybieranych w oddziałach PTBNiDT oraz 5 zaproszonych gości, w tym Sekretarz Generalny SIMP Kazimierz Łasiewicki. Ustępującego Prezesa PTBNiDT SIMP Tomasza Chadego uhonorowano medalem im. Prof. Pawłowskiego w uznaniu za wybitne zasługi i za zdynamizowanie środowiska. Następnie Prezes przedstawił sprawozdanie z działalności Zarządu PTBNiDT SIMP w kadencji 2014-2018.

Od lewej: Bogusław Ładecki (Sekretarz), Tomasz Chady (Prezes) i Bogdan Piekarczyk (Członek Zarządu)

Przedstawiciel Komisji Rewizyjnej – Jan Kielczyk – przedstawił sprawozdanie komisji. W podsumowaniu stwierdzono, że ustępujący Zarząd poprawnie wydatkował fundusze PTBNiDT oraz właściwie wywiązywał się ze swoich obowiązków statutowych. Walne Zebranie Delegatów zatwierdziło bilans PTBNiDT SIMP za rok 2017 oraz udzieliło absolutorium Zarządowi PTBNiDT SIMP w kadencji 2014-2018.

W trakcie zjazdu odbyły się wybory Prezesa Towarzystwa. Jedynym zgłoszonym kandydatem był Tomasz Chady, który został wybrany na Prezesa PTBNiDT SIMP na kadencję 2018-2022 oraz delegatem Towarzystwa na Walny Zjazd Delegatów SIMP.

Do Zarządu PTBNiDT SIMP wybrani zostali: Bogusław Ładecki, Bogdan Piekarczyk, Patryk Uchroński, Marek Lipnicki, Przemysław Łopato oraz Dyonizy Szewczyk. Zarząd się ukonstytuował, Wiceprezesem został Marek Lipnicki, Sekretarzem został Bogusław Ładecki a funkcję Skarbnika objął Dyonizy Szewczyk. Powołano również trzyosobową Komisję Rewizyjną w następującym składzie: Jan Kielczyk, Bogusław Olech, Ryszard Świderski.

Podczas spotkania toczyła się dyskusja nad kierunkami działania Towarzystwa i uchwalane były wytyczne, co do programu działań na okres następnej kadencji.

casp system
ADVANCED TECHNOLOGIES

PRZEMYSŁ 4.0

BADANIA NIENISZCZĄCE

DOSTAWA URZĄDZEŃ I SYSTEMÓW

PRODUKCJA / DYSTRYBUCJA / INTEGRACJA / WDROŻENIE / SERWIS

- Automatyzacja badań nieniszczących
- Obniżenie kosztów badań nieniszczących
- Wzrost efektywności badań nieniszczących
- Wzrost szybkości badań nieniszczących

PT MT ET UT RT VT

LOTNICTWO / MOTORYZACJA / ODLEWNICTWO / ENERGETYKA / PETROCHEMIA / GAZOWNICTWO / RUROCIĄGI
SPAWALNICTWO / KOLEJNICTWO / ELEKTRONIKA / PRZEMYSŁ CIĘŻKI I GÓRNICTWO

Casp System Sp. z o.o.
ul. Puszkina 2, 43-603 Jaworzno
tel.: +48 32 720 24 04 / +48 32 614 12 29 / fax : +48 32 750 56 06 / e-mail: ndt@casp.pl
www.ndt24.pl

casp system
ADVANCED TECHNOLOGIES

Łukasz Rawicki[1]*, Karol Kaczmarek[1], Paweł Irek[1], Grzegorz Hottowy[2], Jacek Słania[1]
[1]*Instytut Spawalnictwa w Gliwicach*
[2]*Przedsiębiorstwo „Ekstplast" Sp. z o.o. w Gliwicach*

Badania ultradźwiękowe szyn kolejowych

Ultrasonic testing of the rails

ABSTRACT

Tests carried out during production and exploitation are to give an answer about the correctness of made products such as rails. Visual and ultrasonic examination are performed. Visual examinations are basic non-destructive examinations in rails diagnostics. In the rails catalog, defects of such damage like cracks were classified. You can find there information about the location, position or causes of defects in the rails. Detection of defects in rails is one of the first applications of ultrasonic testing. The aim of the study is to detect defects occurring in the volume of the material and evaluation of their size. Examination of rails mounted on the track causes the introduction of ultrasonic waves from the surface of the head through the coupling liquid layer with the surface of the test. Access from the surface of footer is impossible and no detectable cracks in the footer can be detected. Application in performing in the field of ultrasonic testing include echo technique, tandem technique or modern ultrasonic technique Phased-Array.

Keywords: *Rails, ultrasonic testing, echo technique, tandem technique, Phased Array techniques*

STRESZCZENIE

Badania wykonywane w trakcie produkcji i eksploatacji mają dać odpowiedź o prawidłowości wykonania wyrobów jakimi są szyny kolejowe. Wykonywane są m.in. badania wizualne i ultradźwiękowe. Badania wizualne stanowią podstawowe badania nieniszczące w diagnostyce szyn kolejowych. W katalogu szyn dokonano klasyfikacji wad takich uszkodzeń jak np. pęknięcia. Odnaleźć tam można informacje dotyczące lokalizacji, położenia czy przyczyn powstawania wad w szynach. Jednym z pierwszych zastosowań badań ultradźwiękowych jest wykrywanie wad w szynach. Celem badania jest wykrycie wad występujących w objętości materiału oraz oceny ich wielkości. Badanie szyn zamocowanych na torze powoduje wprowadzanie fal ultradźwiękowych z powierzchni główki przez warstwę cieczy sprzęgającej z powierzchnią badania. Niemożliwy jest dostęp z powierzchni stopki i nie można wykryć rozwijających się pęknięć eksploatacyjnych w stopce. Zastosowanie przy wykonywaniu badań ultradźwiękowych znajdują miedzy innymi technika echa, technika tandem czy nowoczesna technika ultradźwiękowa Phased-Array.

Słowa kluczowe: *szyny kolejowe, badania ultradźwiękowe, technika echa, technika tandem, , technika Phased Array*

Wady w szynach wykrywane są na początku przy pomocy badań wizualnych. Do tego celu zastosowanie ma m.in. katalog szyn, w którym dokonano systemu klasyfikacji pod kątem wad dotyczących złamań, pęknięć i uszkodzeń. Zamieszczone są informacje dotyczące położenia, wyglądu oraz przyczyn powstawania. W katalogu podano również metody wykrywania wad w szynach, jak i zalecenia dotyczące postępowania z szynami, w których wykryto wady [1].

Bez względu na zasady funkcjonowania każdej z kolei, utrzymanie dróg kolejowych wymagać będzie zawsze usuwania pewnej części szyn z powodu ich pęknięć lub zniszczeń powstałych w procesie produkcyjnym lub powstających w eksploatacji. Ważne jest więc śledzenie zachowania się szyn w torze, dzięki czemu zarówno użytkownicy, jak i producenci mogą skupić swoje wysiłki na podnoszeniu jakości i jednocześnie poprawiać warunki ich eksploatacji [1]. Katalog wad szyn podaje możliwości wykrycia wad w szynach przy pomocy metody wizualnej, dającej możliwość wykrycia oraz obserwacji uszkodzeń znajdujących się na powierzchni szyny oraz monitorowania i rozwoju wad. W katalogu podane są również sposoby wykrywania oraz zalecenia dotyczące wykrytej wady szyny. Na rys.1 pokazano przykład pęknięcia poziomego sklasyfikowanego w katalogu wad szyn.

Pękniecie poziome charakteryzuje się stopniowym oddzieleniem górnej części główki szyny, pęknięcie rozpoczyna się wewnątrz główki szyny i postępuje równolegle do powierzchni tocznej, pęknięcie pojawia się na powierzchni główki, czasami towarzyszy mu pęknięcie pionowe, może występować łącznie z wykruszeniami końców szyn i zazwyczaj obserwuje się poszerzenie powierzchni tocznej. W późniejszym stadium może nastąpić oddzielenie fragmentu metalu, oddzielenie takie traktuje się jako złamanie, gdy ubytek na głębokości materiału przekroczy 10 mm i dł. 50 mm. Sposoby wykrywania to m.in. badanie wizualne, badanie młotkiem, badania ultradźwiękowe [1].

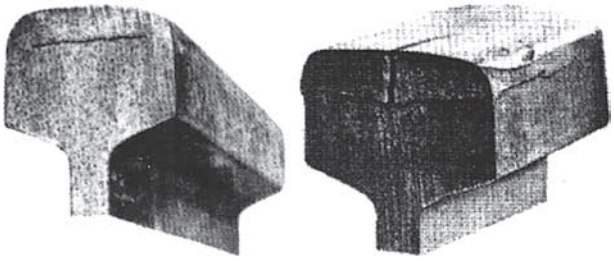

Rys. 1. Pęknięcie poziome (końców szyn) 112. Wada powstała podczas produkcji [1].
Fig. 1. Horizontal crack (the ends of the rails) 112. The defect created during the production [1].

Zalecenia: obserwacja szyny, wymiana szyny, zamknięcie toru, natychmiastowa wymiana złamanej szyny.

Odpowiedzią na pytanie, co znajduje się w objętości elementu badanego są badania ultradźwiękowego. Dają możliwość wykrycia wad wewnętrznych oraz oceny ich wielkości. Podobnie jak w badaniach wizualnych, istnieje możliwość monitorowania rozwoju wady i porównywania z wcześniej przeprowadzanymi badaniami.

Wykrywanie wad w szynach jest jednym z pierwszych zastosowań badań ultradźwiękowych. Układy defektoskopowe

*Autor korespondencyjny. E-mail: lukasz.rawicki@is.gliwice.pl

DOI: 10.26357/BNiD.2018.009

stosowane na stanowiskach kontrolnych w hutach i w ruchomych urządzeniach do badań torowych są bardzo zaawansowane, rozwiązania konstrukcyjne mają jednak istotne ograniczenia. Badanie szyn zamocowanych na torze powoduje wprowadzanie fal ultradźwiękowych z powierzchni główki przez warstwę cieczy sprzęgającej z powierzchnią badania. Niemożliwy jest dostęp do powierzchni stopki i nie można wykryć rozwijających się pęknięć eksploatacyjnych w stopce. Poprzeczne pęknięcia na szynach zaczynają się najczęściej na zewnętrznych krawędziach stopki. Nie wykryte wcześniej prowadzą do zniszczenia. Zestawy głowic ze sprzężeniem cieczowym nie dają właściwych efektów przy wykrywaniu pionowych pęknięć w główce, które powstają najczęściej w części środkowej główki. Niekorzystna orientacja i rozwój pęknięć w kierunku podłużnym i poprzecznym są bardzo niebezpieczne. Celem badania spawanych złączy szynowych jest wykrycie wad występujących w całym przekroju złącza. Badaniom podlegają spoiny i zgrzeiny wykonywane w trakcie napraw nawierzchni oraz inne w zależności od potrzeb [2].

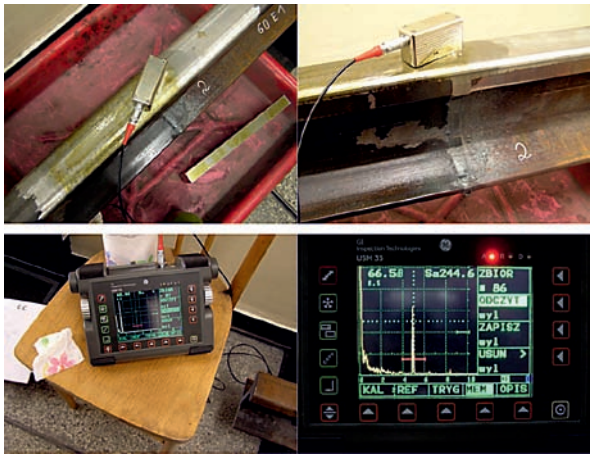

Rys. 2. Przykład wykorzystania ultradźwiękowej techniki echa [3].
Fig. 2. An example of the using of ultrasonic echo technique [3].

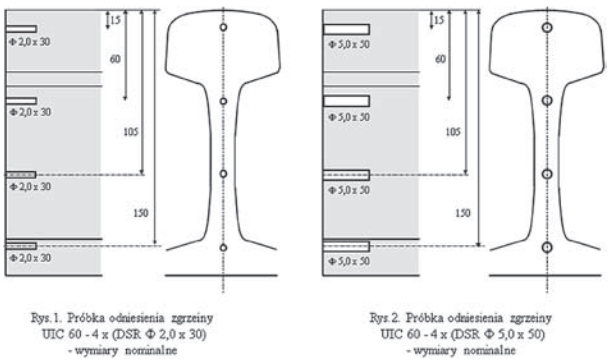

Rys. 3. Wzorce odniesienia z reflektorami wzorcowymi o średnicy 2mm oraz 5mm przy badaniu próbek ze zgrzeinami [3].
Fig. 3. Reference patterns with the reflectors standards with a diameter of 2mm and 5mm at examination of the welded samples [3].

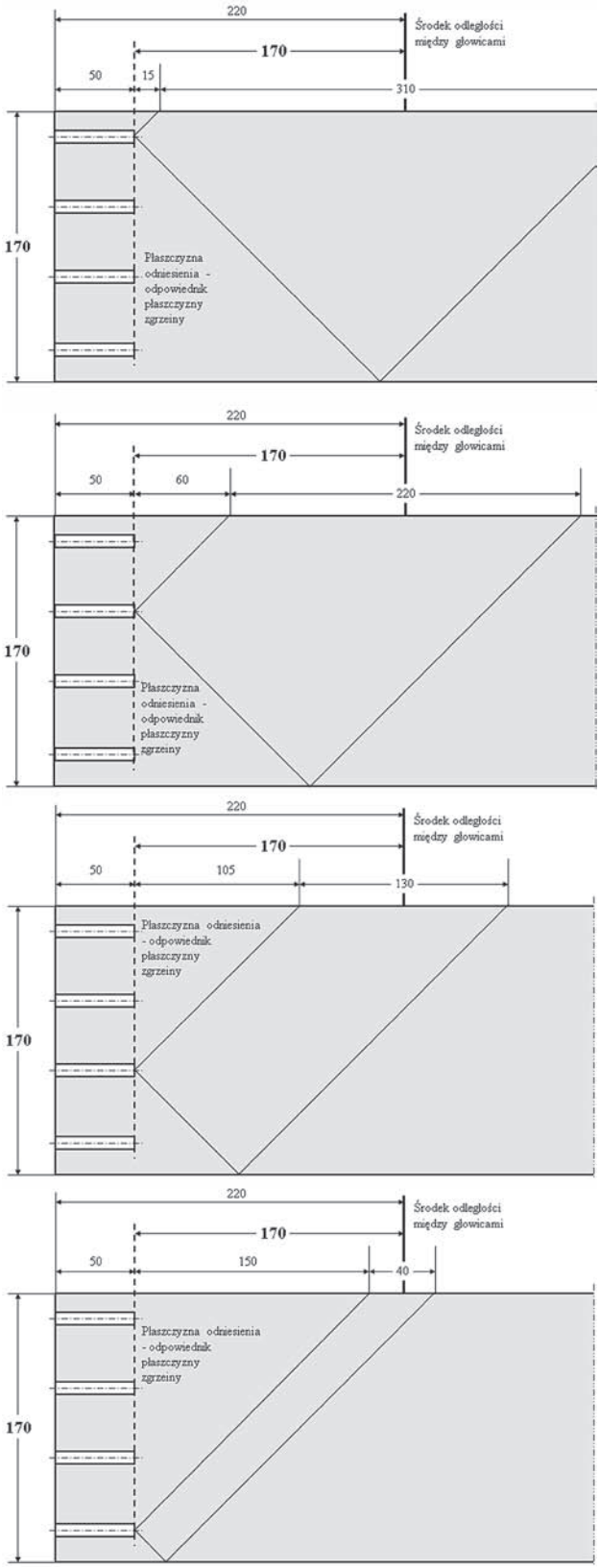

Rys. 4. Przykłady lokalizacji wskazań na przykładzie próbek z reflektorami wzorcowymi [3].
Fig. 4. Examples of location of indications on the example of samples with standards reflectors [3].

W metodzie echa stosuje się pojedynczą głowicę, która początkowo stanowi nadajnik impulsów, a następnie zostaje „przełączona" i odgrywa rolę odbiornika. Sygnał wysyłany przez głowicę do materiału odbija się od nieciągłości lub od przeciwległej powierzchni i wraca do głowicy. Mierząc czas upływający od momentu wysłania impulsu do momentu

jego powrotu i odebrania przez głowicę można określić, znając prędkość fali ultradźwiękowej w materiale, odległość głowicy od przeszkody. Na podstawie wysokości echa niezgodności na ekranie defektoskopu, można określić jej przybliżony wymiar. Na rys. 2 pokazano przykład badania przy pomocy ulradźwiękowej techniki echa.

Na rysunku 3 pokazano przykład wykonanych wzorców do ustawianie czułości badania przy badaniu ultradźwiękowym szyn. Wzorce są wykonane ze sztucznymi reflektorami w postaci otworków o średnicy 2 i 5mm w każdej części badanej szyny tj. główce, szyjce i stopce.

W technice tandem używa się układu dwóch głowic kątowych, nadawczej i odbiorczej, ustawionych w stałej odległości od siebie podczas przeszukiwania złącza. Dla zbadania całej objętości złącza układ głowic przesuwa się kilkakrotnie wzdłuż spoiny zmieniając odległość między głowicami tak, aby za każdym razem przeszukać inny obszar spoiny [3]. Sposób usytuowania głowic w technice tandem i lokalizacji wskazań na przykładzie próbek odniesienia pokazano na rysunku 4.

Zastosowanie techniki echa przy badaniu połączeń spawanych lub zgrzewanych na szynach kolejowych nie daje pozytywnych rezultatów, pokazuje to rys.5. Fala ultradźwiękowa natrafia na wadę zlokalizowaną w materiale, ale na ekranie defektoskopu ultradźwiękowego widać echo dna oraz bardzo słaby sygnał od wady materiału. Odebranie echa nieciągłości przez głowicę odbiorczą może być zobrazowane przez fale impulsową lub ciągłą.

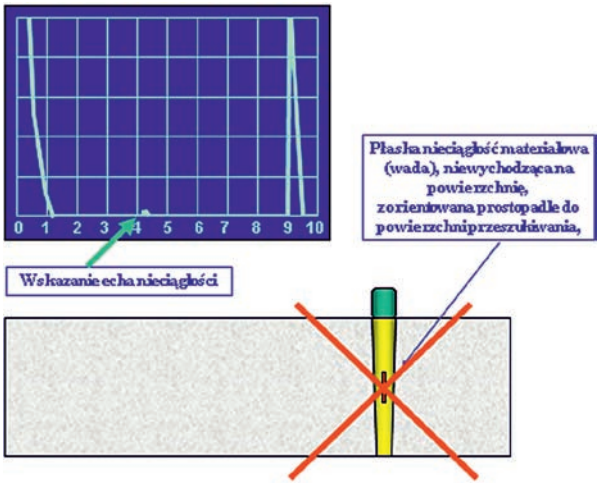

Rys. 5. Zobrazowanie nieciągłości w technice echa [3].
Fig. 5. Imaging of discontinuities in echo technique [3].

Na rysunku 6 pokazano zastosowanie techniki tandem. Głowice ultradźwiękowe ustawione są w określonej odległości względem siebie. Wiązka ultradźwiękowa wyemitowana przez głowicę nadawczą natrafia na nieciągłość zorientowaną w materiale i po odbiciu od niej zostaje odebrana przez głowicę nadawczą. Impuls echa nieciągłości w postaci wielkości amplitudy sygnału zostaje odebrany i zaobserwowany na zakresie podziałki podstawy czasu ekranu defektoskopu ultradźwiękowego.

Na rysunku 7 widać przyrząd do badania szyn w technice tandem. Na specjalnych prowadnicach osadzone są głowice 2T45o. Podziałka milimetrowa ułatwia ustawienie głowic w odpowiednich położeniach względem siebie. Przewody zasilające wyprowadzone od góry ułatwiają przesuwanie głowic względem siebie i umożliwiają ich stabilne zamocowanie. Wytyczne Id-17:2005 „Wytyczne ultradźwiękowych badań złączy szynowych, zgrzewanych i spawanych" opracowane przez PKP Polskie Linie Kolejowe S.A. dopuszczają zastosowanie głowic 3T45o [4]. Zobrazowanie pochodzących impulsów od wad w objętości elementu badanego przekazywane jest w zobrazowaniu typu A pokazującym zobrazowanie amplitudy sygnału ultradźwiękowego w funkcji czasu.

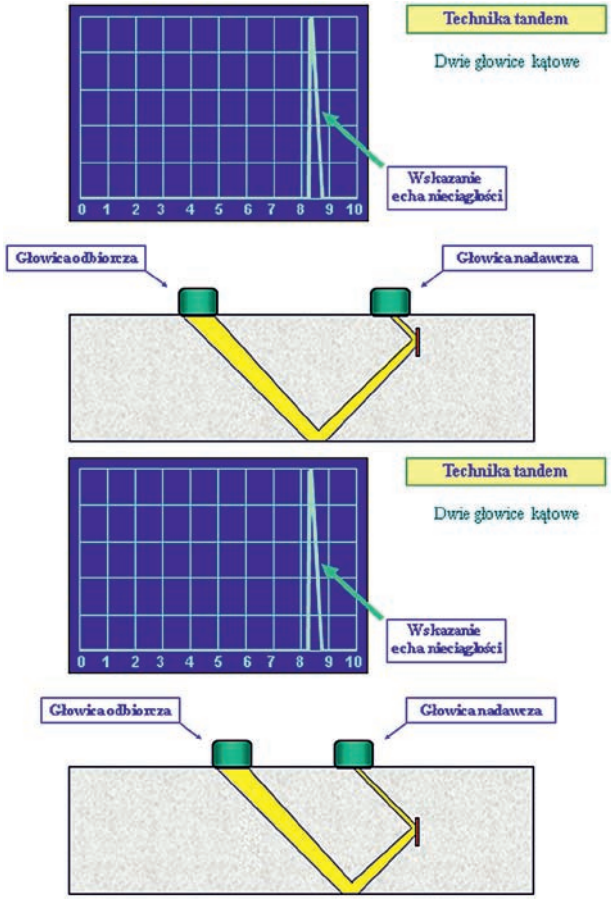

Rys. 6. Zastosowanie ultradźwiękowej techniki tandem [3].
Fig. 6. Application of the ultrasonic tandem technique [3].

Przełomem w zastosowaniu badań ultradźwiękowych jest technika Phased Array, która stanowi rozwinięcie konwencjonalnych badań ultradźwiękowych techniką echa. W technice Phased Array znalazły zastosowanie głowice mozaikowe, zawierające pewną liczbę niewielkich, niezależnie sterowanych przetworników (zazwyczaj 16-64). Zastosowanie głowicy mozaikowej umożliwia wprowadzenie serii wiązek ultradźwiękowych, przetworzenie otrzymanych sygnałów i ich analizę w postaci graficznej z amplitudą kodowaną paletą barw. Powstały w ten sposób S-skan obrazujący położenie wskazań na tle konturu rowka spoiny znacznie ułatwia późniejszą ocenę i charakteryzowanie wykrytych wskazań [5].

W technice Phased Array możliwe jest sterowanie kątem wprowadzenia wiązki ultradźwiękowej, co daje

możliwość uzyskania dowolnych kątów padania lub załamania wiązki poprzez pobudzanie wskazanych przetworników głowicy w zaprogramowanych sekwencjach. Jedna głowica daje możliwość przeprowadzenia skanów przy różnych kątach. Zaletą tej techniki jest również skrócenie czasu badań, co wiąże się m.in. z brakiem konieczności wymiany głowic, a co za tym idzie ponownych kalibracji sprzętu. Na rysunku 8 pokazano przykład bloku kalibracyjnego oraz głowicy w badaniach PA. Zobrazowanie niezgodności oraz system do badania półautomatycznego PA przedstawione są na rysunku 9. W technice PA do obiektu badanego w celu przeszukania objętości badanego materiału wprowadza się wiązkę ultradźwiękową przy wykorzystaniu fal poprzecznych. Stosowane częstotliwości, zakresy stosowanych przetworników, jak również stosowane charakterystyki wiązek ultradźwiękowych nie różnią się od stosowanych w tradycyjnych badaniach ultradźwiękowych. Zasada badania jest bardzo zbliżona do klasycznej metody ultradźwiękowej. Akceptacja wskazania polega na pomiarze maksymalnej amplitudy echa w odniesieniu do ustalonego echa reflektora wzorcowego.

Rys. 7. Przyrząd do badania w technice tandem [3].
Fig. 7. The examination device in tandem technique [3].

Zakres badania jaki może być zastosowany w technice PA zależy od czynników związanych z warunkami konstrukcyjnymi głowicy takich jak. budowa głowicy, częstotliwość, apertura. Ustawienie aparatury w badaniach techniki PA jest zadaniem dużo trudniejszym niż w konwencjonalnych badaniach ultradźwiękowych. Na etapie wejściowym wprowadzeniu podlegają parametry wizualizacji przekroju elementu badanego, takie jak grubość badanego materiału, pozycjonowanie używanych głowic względem siebie; opóźnienia dla używanych skanów liniowych lub sektorowych; kalibracja używanego sprzętu w postaci m.in czułości badania i rozdzielczości enkodera. Nowoczesne systemy posiadają kreatory badania pozwalające na łatwe wprowadzenie wszystkich parametrów i wykonanie wymaganych kalibracji.

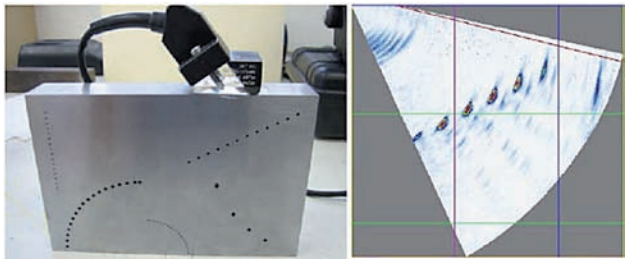

Rys. 8. Głowica i blok kalibracyjny do badań PA oraz zobrazowania 2D otworów [5].
Fig. 8. The head and calibration block for PA examination and 2D imaging of holes [5].

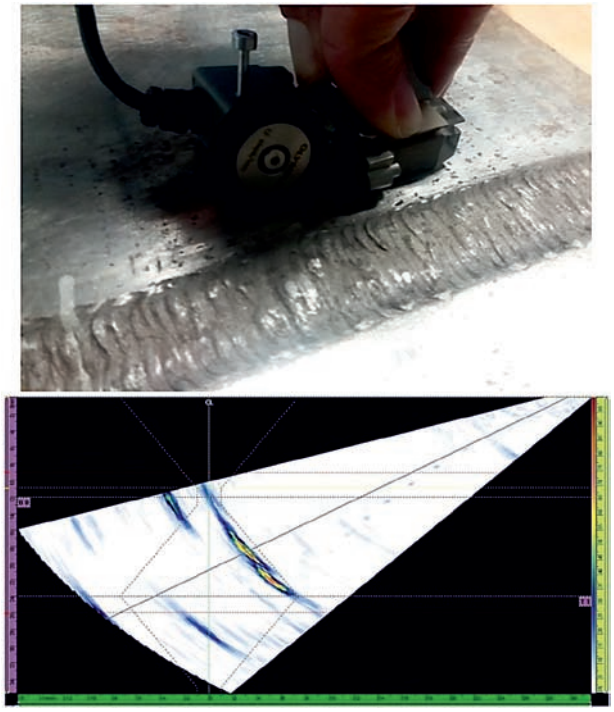

Rys. 9. System do półautomatycznych badań PA-głowica z zainstalowanym enkoderem oraz zobrazowanie niezgodności w badanym złączu [5].
Fig. 9. System for semi-automatic studies PA-head with an installed encoder and imaging of discrepancies in the tested joint [5].

Na rysunku 10a pokazano defektoskop wraz ze skanerem do przeprowadzania badań PA. Na ilustracjach b i c widoczne są przykłady zobrazowań skanu liniowego i sektorowego.

W technice Phased Array wykorzystywane są znormalizowane wzorce zgodnie z normą ISO 19675. Przykład znormalizowanego wzorca dla techniki PA pokazano na rysunku 12.

Technika PA wykorzystuje do przeszukania objętości materiału dwa rodzaje elektronicznych skanów. Wykorzystywane skany to E-skan liniowy i S-skan sektorowy pokazane

na rysunkach 13, 14, 15 i 16.

W skanie typu E punkt wyjścia wiązki ultradźwiękowej przesuwa się wzdłuż głowicy, co pozwala na przeszukiwanie różnych obszarów złącza spawanego szyny. Staje się to możliwe dzięki jednoczesnemu pobudzaniu zespołów głowicy liniowej w kolejnych cyklach częstotliwości przetwarzania. W badaniach konwencjonalnych przemieszczanie wiązki odbywa się fizycznie za pomocą ruchu głowicy. W technice PA przemieszczanie wiązki odbywa się za pomocą sygnałów elektronicznych.

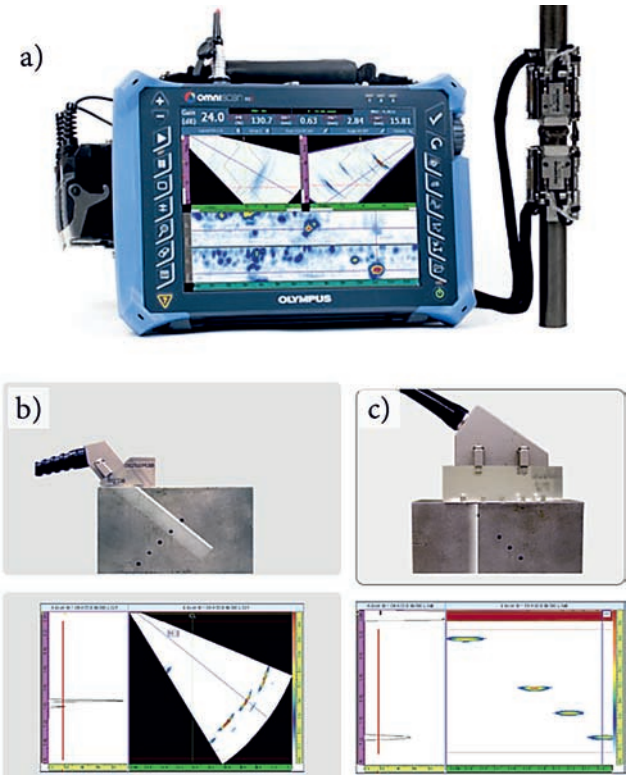

Rys. 10. a) Defektoskop i skaner do badań PA, b) głowica skośna PA do badań i wyniki badania z wykorzystaniem skanu sektorowego, c) głowica prosta PA i wyniki badania z wykorzystaniem skanu liniowego [5].
Fig. 10. a) Flaw detector and scanner for PA examination, b) oblique head for PA examination and test results using a sector scan, c) head straight for PA examination and test results using a linear scan [5].

Na rysunku 11 zaznaczono rodzaje zobrazowań 2D możliwych do uzyskania w oparciu o wcześniej wykonane badania enkodowane z pełnym zapisem wyników [5].

Wykonanie badania wiąże się z szeregiem wprowadzonych parametrów wstępnych takich jak m.in. odległość głowicy od środka spoiny, kąt fali wprowadzonej do materiału badanego. W przypadku badania typowych złączy spawanych kolejne wiązki fali ultradźwiękowej generowanej w E-Skanie pokrywają całą objętość spoiny i przylegającej do niej strefy wpływu ciepła. Skanowanie liniowe typu E, którego przykład w technice PA pokazano na rys. 13, sprawdza się do wykrywania nieciągłości, jakimi są przyklejenia brzegowe ,pod warunkiem odpowiedniego dopasowania kąta emitowanej wiązki. Minusem skanu typu E jest stosowanie wieloprzetwornikowych głowic dla techniki PA dla odpowiednio długich zakresów wiązki ultradźwiękowej. Kontroli wymaga również utrzymanie na odpowiednim poziomie sprzężenie akustyczne odpowiedzialne za kontakt głowicy z obiektem badanym [6].

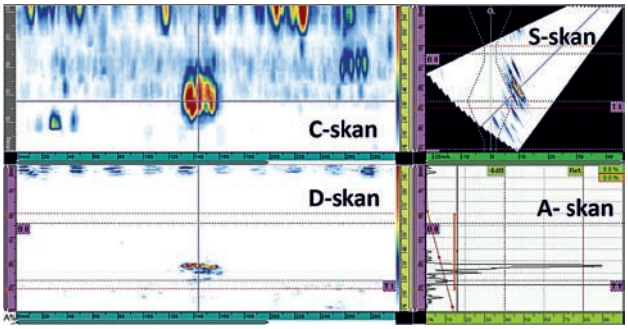

Rys. 11. Przykłady zobrazowań uzyskiwanych w badaniach półautomatycznych [5].
Fig. 11. Examples of images obtained in semi-automatic studies [5].

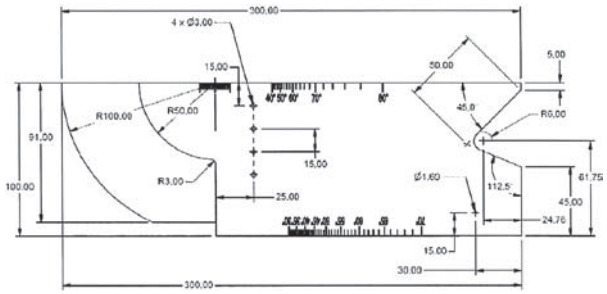

Rys. 12. Wzorzec dla techniki Phased Array zgodnie z normą ISO 19675 [5].
Fig. 12. Pattern for the Phased Array technique in accordance with ISO 19675 [5].

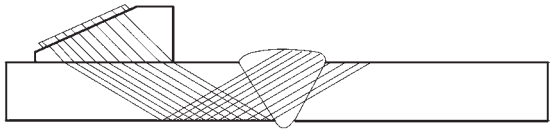

Rys. 13. Zasada skanu liniowego w technice PA badań ultradźwiękowych [7].
Fig. 13. The principle of linear scan in the PA technique of ultrasonic examinations [7].

Skanem stosowanym również w technice PA jest skan typu S, którego zasadę zobrazowania w technice PA jako skan sektorowy pokazano na rys.14. Wiązki ultradźwiękowe emitowane z głowicy ultradźwiękowej różnią się między sobą kątem pod jakim wchodzą do elementu badanego. W zakresie kątowym należy uwzględnić odległość głowicy od osi spoiny elementu badanego tak, aby wiązka elektronicznego S-skanu mogła pokryć objętość badanej spoiny i stref wpływu ciepła. Do zalet badania S-skanem w technice PA należy mniejszy rozmiar stosowanych głowic, zazwyczaj głowic 16 elementowych [6].

Zakres kątowy w technice PA w badaniach wiązką fal poprzecznych powinien być zawężony do kątów w granicach przedziału 40-75°. Nie należy stosować kątów poniżej 33°, ponieważ w badanym materiale mogą powstać zarówno fale podłużne, jak i poprzeczne. Badania techniką PA mogą być

wykonywane zarówno techniką manualną, czyli ręczną, jak również automatyczną. Często wykorzystywaną techniką jest technika półautomatyczna, gdzie przesuw skanera razem z głowicami następuje ręcznie, a rejestracja danych w sposób automatyczny przy pomocy stosowanego enkodera.

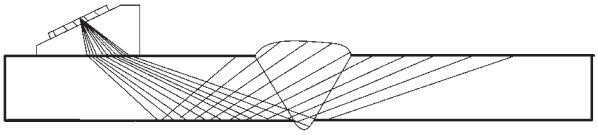

Rys. 14. Zasada działania skanu sektorowego w technie PA badań ultradźwiękowych [7].
Fig. 14. Principle of operation of the sector scan in the PA technique of ultrasonic examinations [7].

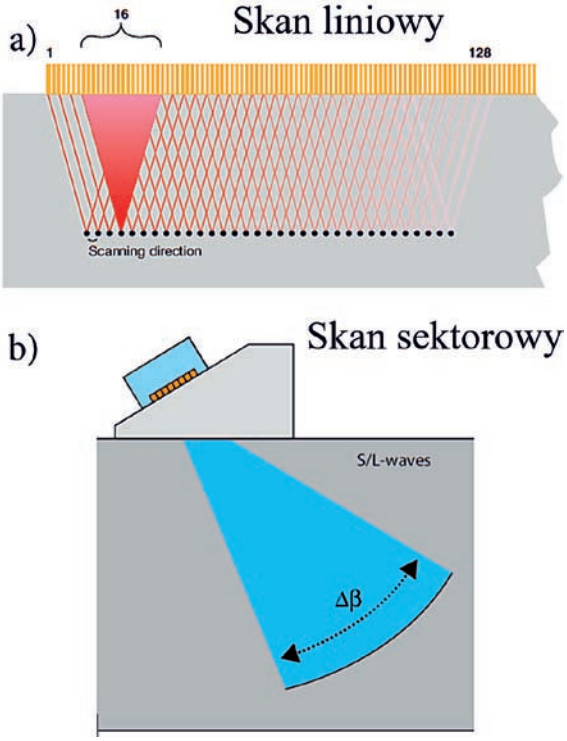

Rys. 15. Rodzaje skanów w PA-liniowy i sektorowy [5].
Fig. 15. Types of scans in PA-linear and sectoral [5].

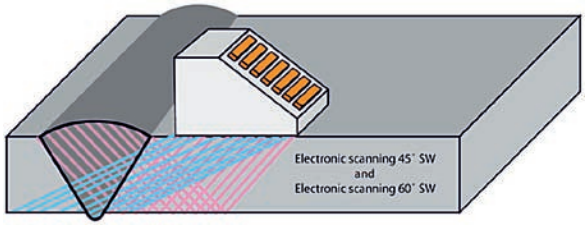

Rys. 16. Przykład badania głowicą PA z zastosowaniem podwójnego skanu liniowego kąt wprowadzenia wiązki 45° i 60° [5].
Fig. 16. Example of testing with a PA head using a double linear scan, angle of beam introduction 45° and 60° [5].

Do zalet techniki Phased Array można zaliczyć [5]:

- duża szybkość badania, znacznie wyższa niż w konwencjonalnych badaniach ultradźwiękowych;
- ocena wyników badania może być prowadzona off-line na komputerze PC;
- intuicyjna, graficzna wizualizacja wskazań;
- duże możliwości w zakresie charakteryzowania wskazań (określanie rodzaju niezgodności);
- możliwość wyznaczenia wymiarów geometrycznych niezgodności;
- możliwość archiwizowania wyników badania w postaci cyfrowej;
- możliwość powtórnej oceny wyników badania przez inną osobę (podobnie jak w przypadku radiografii);
- szeroki zakres możliwych zastosowań techniki PA;
- możliwość elektronicznego kształtowania wiązki ultradźwiękowej (kąta wprowadzenia, apertury, z której generowana jest wiązka i ogniskowania wiązki);
- możliwość symulowania jedną głowicą Phased Array głowic konwencjonalnych o różnych kątach wprowadzenia wiązki i różnych parametrach ogniskowania;
- możliwość badania techniką tandem przy zastosowaniu pojedynczej głowicy PA;
- możliwość prezentacji graficznej wyników w czasie rzeczywistym (S-Skan, E-Skan);
- istotne zwiększenie szybkości badania, w stosunku do konwencjonalnych badań ultradźwiękowych;
- możliwość automatyzacji badań;
- możliwość stosowania zarówno oceny amplitudowej, jak i wymiarowej wykrytych wskazań;
- możliwość pełnego zapisu wyników w przestrzeni 3D (skan enkodowany);
- ułatwiona interpretacja wyników badania, w szczególności dla obiektów (złączy) o złożonej geometrii.

Z powodu dużych możliwości i istotnych zalet techniki PA w stosunku do innych technik i metod badań nieniszczących należy oczekiwać szybkiego wdrażania ich w praktyce przemysłowej. Można oczekiwać, że badanie tą techniką znajdzie również zastosowanie w zakresie badań szyn kolejowych lub ich złączy.

Literatura/References

[1] Makuch J.: Prezentacja. Diagnostyka szyn, wady w szynach. Katedra Mostów i Kolei. Politechnika Wrocławska. Wrocław 2015
[2] Deputat J.: Nowe Techniki Badań Ultradźwiękowych. Pracownia Ultradźwiękowych badań materiałów. IPPT PAN Warszawa
[3] Hottowy G.: Materiały własne firma Ekstplast.
[4] Wytyczne PKP Polskie Linie Kolejowe S.A. Id-17:2005.: Wytyczne ultradźwiękowych badań złączy szynowych, zgrzewanych i spawanych. Warszawa 2005
[5] Kaczmarek K: Prezentacja. Nowoczesne techniki badań ultradźwiękowych oraz ich zastosowanie. Gliwice 2017
[6] Mackiewicz S.: Badania złączy spawanych techniką Phased Array w świetle wymagań PN-EN ISO 13588. Przegląd Spawalnictwa nr 12/2015, s. 101-106
[7] Mackiewicz S.: Ultradźwiękowe badania złączy spawanych techniką Phased Array. XXI Nieniszczące Badania Materiałów. Zakopane 18-20 marca 2015

Volodymyr Troitskiy*
The E.O.Paton Electric Welding Institute of the National Academy of Science of Ukraine

Industrial X-ray testing without intermediate data carriers of information

Przemysłowe badanie rentgenowskie bez pośrednich nośników informacji

ABSTRACT

The new direction of radiography is Flash-radiography (FR) which doesn't have intermediate data carriers (films and storage plates). FR produces a quick image. It provides low testing cost, and capability of multi-angle real time internal defects monitoring of the objects.
In film radiography, if relative photometric density is more than 4, then the snapshots become virtually unreadable and they can be difficult to be digitized. Current film-free technologies do not have this disadvantage and, besides, give results in a digital form without special digitizing systems.
Digital data contain radiation images of internal defects, expand the flaw-detection possibilities and reduce testing cost. Flash-radiography is based on portable X-ray television, which allows the observation of X-ray testing results on a monitor screen. The internal defects examination from different angles may be carried out.
Flash-radiography with digital solid-state transducers is the most perspective one with sensitivity up to 0.1% of examined metal's thickness at resolution exceeding 10 pairs of lines per mm. Application of small-size movable solid-state transducers opens new technological capabilities. They can be located and moved in the zones where positioning of film holders and storage plates is impossible. The new X-ray mini technology expands the application of NDT. The examples of practical application of solid-state miniature transducers are presented.

Keywords: *Film radiography, Flash-radiography, digital image, scintillator, solid-state transducer, X-ray mini technology*

STRESZCZENIE

Nowym kierunkiem radiografii jest radiografia błyskowa (ang. flash radiograpy, FR), która nie ma pośrednich nośników danych (błon i płyt pamięciowych). FR tworzy szybki obraz. Zapewnia niskie koszty testowania oraz możliwość monitorowania obiektów pod kątem błędów wewnętrznych w czasie rzeczywistym. W radiografii błonowej, jeśli względna gęstość fotometryczna jest większa niż 4, migawki stają się praktycznie nieczytelne i mogą być trudne do digitalizacji. Obecne technologie wolne od błon radiograficznych nie mają tej wady, a poza tym dają wyniki w formie cyfrowej bez specjalnych systemów do digitalizacji.
Dane cyfrowe zawierają obrazy promieniowania z defektów wewnętrznych, rozszerzają możliwości wykrywania wad i zmniejszają koszty testowania. Promieniowanie błyskowe jest oparte na przenośnym aparacie rentgenowskim, który umożliwia obserwację wyników badań rentgenowskich na ekranie monitora. Można przeprowadzić badanie wad wewnętrznych pod różnymi kątami.
Promieniowanie błyskowe z cyfrowymi przetwornikami półprzewodnikowymi jest najbardziej perspektywiczne z czułością na poziomie do 0,1% badanej grubości metalu przy rozdzielczości przekraczającej 10 par linii na mm. Zastosowanie przenośnych przetworników półprzewodnikowych o niewielkich rozmiarach otwiera nowe możliwości technologiczne. Można je lokalizować i przemieszczać w strefach, w których nie jest możliwe pozycjonowanie uchwytów błon i płyt do przechowywania. Nowa mini technologia rentgenowska rozszerza zastosowanie NDT. Przedstawiono przykłady praktycznego zastosowania miniaturowych przetworników półprzewodnikowych.

Słowa kluczowe: *Radiografia błonowa, radiografia błyskowa, obraz cyfrowy, scyntylator, przetwornik półprzewodnikowy, technologia przenośnych urządzeń X-ray*

1. Introduction

Radiation methods are preferred to be used in quality of welded and brazed joints testing as well as in mastering the number of process solutions due to illustrative results. This method is also used to validate other NDT methods.

Significant qualitative changes took place in recent years expanding the possibilities of the non-destructive radiation testing, first of all due to appearance of new multi-element semiconductor radiation image detectors as well as intensive implementation of means for producing, processing and analysis of digital images, which are illustrative, easy for archiving and electronic transmission. Such detectors use electronic means and transform ionizing irradiation, passed through examined object containing information about its internal defects, into an electric signals package. After that the signals are digitized, processed and used to make a digital image of the object being examined.

Digital image (DI) can be observed directly during inspection, i.e. in real time. Such a method of radiation testing without intermediate carriers of information is called Flash-radiography. Virtually, it is portable X-ray television with electronic record of information, which can be delivered to a customer, uploaded on the internet, archived and stored on memory cards without additional digitalizing and decoding.

A distinctive feature of the flash-radiography is the absence of intermediate carriers of information, radiographic films, semiconductor (SC) store plates with photo-stimulated memory.

Adjustment of mode in widespread technologies with intermediate carriers of information requires multiple exposures, highlighting, processing and expensive devices for digitizing and reading information. Therefore, absence of intermediate carriers of information (films, semiconductor plates) provide increased efficiency and significant cost reduction of quality testing.

*Correspondence author. E-mail: ndt@paton.kiev.ua

DOI: 10.26357/BNiD.2018.010

2. Methods of radiation digital images producing

Examination of the object's internal defects with the help of portable X-ray television equipment having digital image processing provides principle changes in technology of non-destructive radiation testing. Commonness of optical and radiation digital images (DI) application has increased in recent time. Hardware and software used for processing and digitization of X-ray films and providing digital images are more widely distributed. The digital images can also be produced by means of storage plates instead of X-ray films. Methods and algorithms of DI processing are the same for all three variants of radiation testing (Figures 1-3). This is an important direction in current radiation flaw detection. Now digital images are typically produced by means of X-ray patterns digitization. Rarely, it is produced by processing latent image being read from re-usable storage plates. The same result can be received from flash-radiography digital detectors without additional expenses related with intermediate information carriers.

The digital image produced by any of three indicated methods, shall have similar interpretation. The processing results of radiography DI shall not be inferior to sensitivity and resolving power of the results of radiographic film received via film viewer. An image quality is evaluated using the reference specimen images. On DI they shall be similar to the reference specimen images of X-ray films examined using film viewer.

There are three technologies (see Figures 1,2,3) for receiving DI-results of radiation testing in electronic form, but the principles of processing and further decoding of these images are the same.

Figure 1 shows a classical process of DI production by means of X-ray film patterns digitization. This traditional technology is well known in all branches of industry. It requires preparation of film cartridges and screens. Chemical treatment, film drying, reading information on film viewer and digitizing the results with the help of corresponding computer complex follow up inspection. This technology is mainly used for compact archiving of NDT results in digital form and receiving additional information which cannot be obtained without digitization.

Figure 2 gives a scheme of more perfect technology for digital image production based on storage plates, that is called CR. In comparison to previous scheme of DI production, this technology provides the possibility of multiple use of intermediate carrier of information (storage plate). This makes the process quicker, but does not reduce its price, since it requires qualified personnel, a lot of time for auxiliary operations and expensive readout equipment. Often the storage plates have their inherent defects. Eliminating the details of this method disadvantages, it is necessary to note an appearance of "sandwich" technology which allows exposing on film and storage plate simultaneously.

World film manufacturers such as Agfa, Fuji, Kodak etc, kept the way of film replacement with semiconductor multiple storage plates. Various equipment was developed for this technology realizing. The E. O. Paton Electric Welding Institute spent a lot of time on implementation of selenium plates and other intermediate carriers of information. All these technologies with re-usable carriers of information did not gain ground because of two reasons, i.e. due to expensive equipment and necessity of highly skilled personnel.

Figure 3 shows a scheme of X-ray technology (flash-radiography) based on fluoroscopic and solid detectors. This is the quickest and cheapest method to produce digital image in e-form, which does not require processing and reading equipment and corresponding additional time.

Both types of radiation testing without X-ray films (Figures 2, 3) can provide better results, than the digitized images produced with the help of X-ray film. It is known that the higher optical density and the more exposure provide more information exposed film contains. Therefore, a good scanner is necessary to digitize high density films to collect all the data available on the film. Many reading devices and

Fig. 1. Traditional scheme of radiographic testing with film and X-ray patterns digitization: (1) cartridge with X-ray film; (2) processing of X-ray film; (3) image scanning; (4) digital image

Rys. 1. Schemat tradycyjnych badań radiograficznych z digitalizacją błon i wzorów rentgenowskich: (1) kartridż z błoną rentgenowską; (2) przetwarzanie błony rentgenowskiej; (3) skanowanie obrazu; (4) obraz cyfrowy

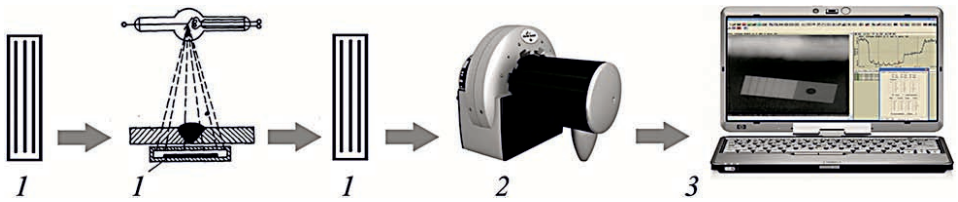

Fig. 2. Scheme of inspection using storage plate: (1) cartridge with store plate; (2) readout of information from plates; (3) digital image.

Rys. 2. Schemat kontroli z użyciem nośnika informacji: (1) wkład z płytą; (2) odczyt informacji z tablic; (3) obraz cyfrowy.

cheap scanners cannot provide high quality digitization of X-ray images, if their relative optical density is above three. All the attempts to receive satisfactory DI from the denser films have not been successful. Thus, satisfactory DI in the film variant (see Figure 1) is possible, if optical film density is in 1.5-2.5 range. At such values the digitizer noises do not introduce irreversible distortions in DI. Experience in digitization of film images with 3-3.2 order density has already shown unsatisfactory results. Fine information is difficult for displaying. For example, images of small pores less than 0.2 mm diameter and cracks with small opening are lost. Therefore, film digitization has significant limitations. Part of the defects, detected with the help of film viewer, is not found on DI. This is a significant disadvantage of traditional film radiography, which is virtually impossible to eliminate in real production.

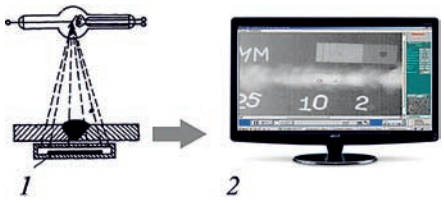

Fig. 3. Quick X-ray inspection scheme without intermediate carriers of information: (1) solid flash-transducer; (2) digital image
Rys. 3. Schemat szybkiego prześwietlenia rentgenowskiego bez pośrednich nośników informacji: (1) przetwornik błyskowy; (2) obraz cyfrowy.

Technologies without film in Figure 2 and 3 do not have this disadvantage; they differ by large dynamic range that expands the possibilities of non-destructive testing. Analysis of DI by technological schemes of Figures 2 and 3 verified that a detectability of small pores, cracks and various inclusions in the welded joints exceeds information about them on the film. Technology from Figure 3 based on solid or optoelectronic transducers are particularly perspective. It provides possibility, after DI computer processing to obtain up to 0.1% sensitivity and examine moving object. The defect detectability is increased due to the fact that moving small images are better distinguished by human eye, than that in static form. It is possible to change the inspection direction if intermediate carriers of information are absent during inspection in Figure 3.

DI received by using three technologies, shown in Figures 1,2,3 is easily archived and webcasted. Time consumption and cost of information being received using presented technological schemes approximately refer correspondingly as 10:5:1 and 5:20:1. Film radiography in Figure 1 offers large number of procedures, which sometimes is repeated several times to get the satisfactory results. There are no such procedures during FR. Film radiography is approximately 10 times longer than FR (Figure 3) to receive the same result. When using the storage plates less auxiliary procedures are needed to obtain the same information of object. Therefore the time spent is correlated approximately as 10:5:1.

As for the cost, the ratio of 5:20:1 means that during X-ray technologies in Fig. 1,2 the equipment for information reading, highly qualified specialists as well as repeated exposures should be used to receive the same results as at FR.

The technologies represented on the Fig. 1 and 3 do not need expensive maintenance. Certainly the numbers 5:20:1 depend on many factors, including the level of life in given country.

For FR the time and the cost were taken to be 1. Two other techniques (Figures 1, 2) take more time 10:5:1 and cost 5:20:1. The exposure at the dentist or fluoroscopy in the hospital is performed for a few seconds, and the picture costs few cents. While the similar results based on the technologies shown in the Fig. 1 and Fig. 2 are significantly longer and much more expensive.

In a short time, detection of the internal defect corrosion damages with the help of portable flash-radiography equipment would become mandatory for all oil-and-gas auxiliary pipelines, which virtually have no control at present time, since X-ray film testing is expensive and ultrasonic testing is less efficient.

Figure 4 presents structural schemes of radiation testing image production in digital form on three described technologies (see Figures 1-3). Procedures of these technologies differ in a stage of digital image production, and DI processing is the same for all three schemes. Therefore, expenses for realizing these procedures and equipment for DI receiving are also different.

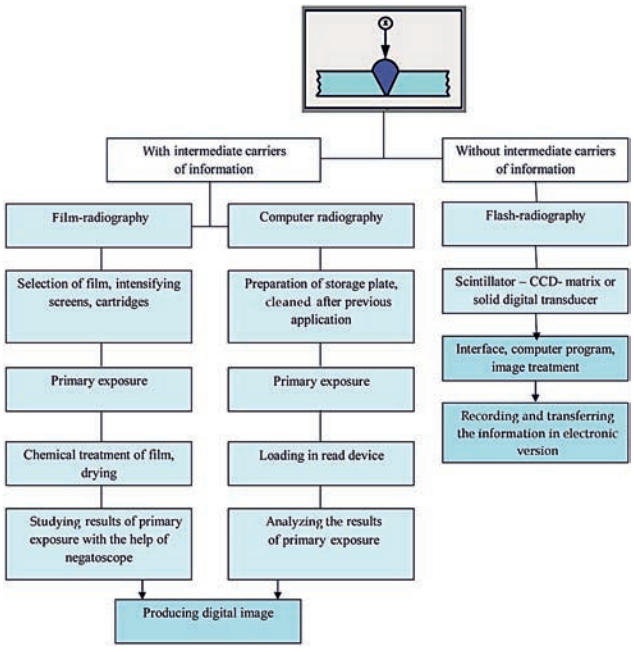

Fig. 4. Structural scheme of process procedures for getting the results of radiation testing in electronic form with film (see Figure 1), computer (see Figure 2) and flash-radiography (see Figure 3)
Rys. 4. Schemat strukturalny procedur procesowych służących uzyskaniu wyników badań radiacyjnych w formie elektronicznej za pomocą błony (patrz rysunek 1), komputera (patrz rysunek 2) i radiografii błyskowej (patrz rysunek 3).

A general disadvantage of the first two technologies with intermediate carriers of information (see Figures 1 and 2) is necessity of re-inspections, sometimes multiple inspections for determination of optimum values of anode voltage, exposure time, focal distance as well as auxiliary procedures

with intermediate carriers of information. Usually, an operator, when working with new unknown objects, needs to find the correct inspection mode and procedure for intermediate carrier of information. Typically, it is performed by means of selection, multiple exposures, i.e. repeating all preparatory operations before inspection.

The most important advantage of the technology, presented in Figure 3, is possibility to observe image changes on the screen during inspection. This is the way to determine the optimum modes. Besides, there is a possibility of multi-angle examination of image of internal defect.

Technologies based on small, few square centimeters, solid digital electron transducers are in specific interest. They do not have limitations related with cartridges, screens, and storage plates. Mobile transducers can move freely over the object surface. Such possibilities are included in diagnostics widely used on practice [8] large custom objects which can have unlimited size. Testing such objects with the help of intermediate carriers of information (films, storage plates) is virtually unreal [8]. Miniature solid transducers can be used on structures of different shape. Images from separate small transducers are joined in general image of object having complex form.

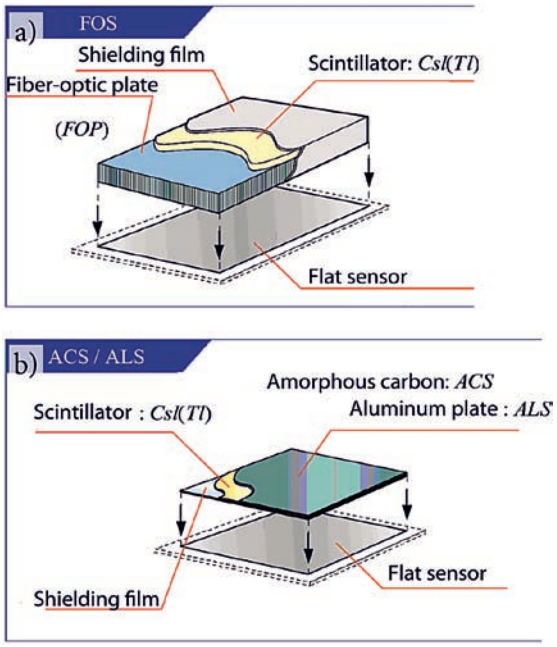

Fig. 5. Design variants of flat flaw detectors of Hamamatsu Photonics company (a) design in which image from screen to sensor is transferred by fiber-optic plate; (b) design with direct positioning of scintillation screen over sensor (CCD-matrix)
Rys. 5. Warianty konstrukcyjne płaskich defektoskopów firmy Hamamatsu Photonics a) konstrukcja, w której obraz z ekranu na czujnik jest przenoszony przez płytę światłowodową; (b) projekt z bezpośrednim pozycjonowaniem ekranu scyntylacyjnego nad czujnikiem (matryca CCD).

Flash-radiography allows varying all main parameters (focus distance, exposure, anode voltage and current) and observing the changes in the image on display screen in real time mode. This significantly reduces the time and consumables. Besides, artifacts from films, screens, storage plates, cartridges in the technologies with intermediate carriers of information are difficult to remove. In the case with real time image, i.e. on technology shown in Figure 3, with possibility to change testing mode parameters, the artifacts are easy to detect and further remove. There are algorithms for electronic images operation. They provide accumulation and extraction of separate fragments in DI.

The USA, Japan, Germany, Russia and other countries carry out intensive works on improvement of solid electron transducers, mobile X-ray television flaw detectors, which replace ultrasonic equipment thanks to better detection capabilities. In time, this tendency will also come in other countries. Therefore, it is necessary to study process capabilities of flash-radiography. A lot of companies manufacture different scintillation panels. Significant part of such devices is described in work [3]. The E. O. Paton Electric Welding Institute cooperates with Hamamatsu Photonics company (Japan). Figure 5 shows two principles of design of solid detectors of this company, and Table 1 provides characteristics of some of them.

Tab. 1. Characteristics of scintillator panels CsI (Tl) of Hamamatsu company
Tab. 1. Charakterystyka paneli scyntylacyjnych CsI (Tl) firmy Hamamatsu

Panel	Panel type	Size, mm	Effective area, mm	Substrate thickness, μm	Scintillator thickness, mm	Light relative output, %	Contrast transfer function, lp/mm
FOS	J6673	50x10	47x7	3	150	70	10
	J6673-01				150	40	
	J6677	50x50	47x47	3	150	70	10
	J6677-01				150	40	
ACS	J8734	50x50	48x48	0,5	150	125	10
	J8734-01				150	150	
	J8977	468x468	440x440	2	600	250	3
ALS	J8978	50x50	48x48	1	150	70	10
	J9857	468x468	440x440	1	600	150	3

The following designations are taken in the Table 1: FOS - Fiber Optic Plate with Scintillator; ACS - Amorphous-Carbon Plate with Scintillator; ALS - Aluminum Plate with Scintillator. Light output and contrast transfer function (CTF) were measured with the help of CCD-matrix at 60kV voltage on X-ray tube. Aluminum filter of 1 mm thickness was used.

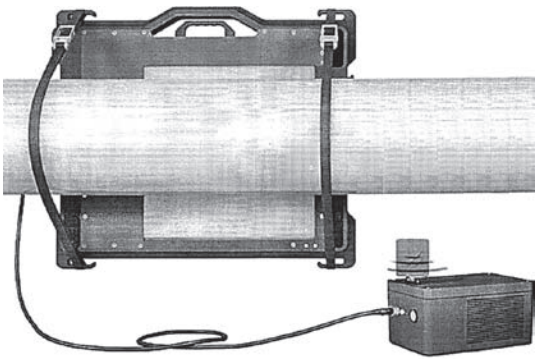

Fig. 6. Pipeline corrosion damage examination with a usage of DRP2020NDT
Rys. 6. Badanie uszkodzeń korozyjnych rurociągów za pomocą DRP2020NDT

A lot of companies in the USA, Japan and Europe produce solid digital transducers virtually to prevent any problems of radiation testing. Figure 6 shows the pipeline corrosion damage examination process with the help of solid transducer of DRP2020NDT type [9], providing wireless transmission of digital image on the screen.

3."X-ray mini" technology capabilities

Inspection X-ray system can be developed based on mini R-transducers (Figure 5). At that, the X-ray transducer [12] is moved over the object surface as it takes place in ultrasonic testing.

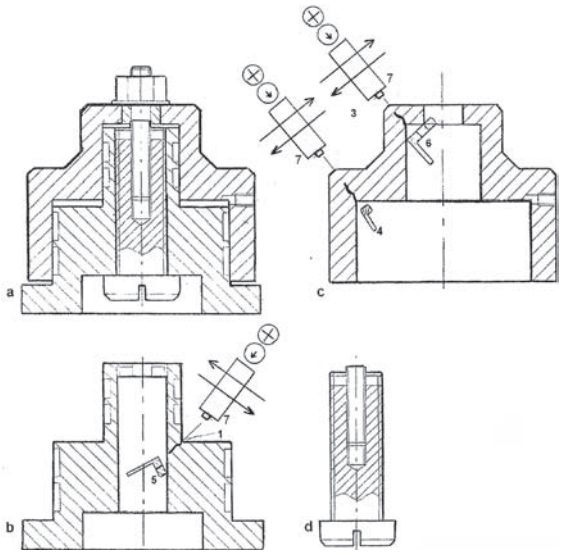

Fig. 7. Test bench for bolts of nuclear reactors: (a) total view; (b) plunger; (c) body; (d) bolt being tested; (,2,3) cracks in the plunger and body appearing in testing of high-strength bolts; (4) one; (5) two; (6) three-section solid-state radiation transducers; (7) radiation source (isotope, R – tube).

Rys. 7. Stanowisko badawcze do śrub reaktorów jądrowych: (a) widok ogólny; (b) tłok; (c) korpus; (d) testowana śruba; (2,3) pęknięcia w tłoku i korpusie pojawiające się podczas testowania śrub o wysokiej wytrzymałości; (4) jeden; (5) dwa; (6) trzyczęściowe przetworniki promieniowania półprzewodnikowego; (7) źródło promieniowania (izotop, R - rura).

The solid-body transducers allow eliminating exposure of large areas and checking only small zones, where interval defects are expected. Such a mobile flash-radiography was used (Figure 7) for examination of testing bench with critical bolts used for joining power reactors, where internal defects can't be found by other methods. Mini R-transducers are recommended for the objects similar to shown in Figure 7. Such a variant of flash-radiography is called "X-ray mini" technology. We realize it using any solid-stare transducers including shown in Figure 5. Mobility of the R-transducer as well as R-emitter (isotope, ceramic tube) is used in X-ray mini technology realizing. Mini-detectors which are ten times smaller than large-panel ones (Figure 6) can easily be used in tangential inspection [13,14] of pipes and stop valves in heat and nuclear engineering. X-ray mini technology should find wide application in monitoring the technical condition of aircraft, lifting and other dangerous equipment. Mobility of the R-transducer as well as emitting source is expanding the capabilities of NDT.

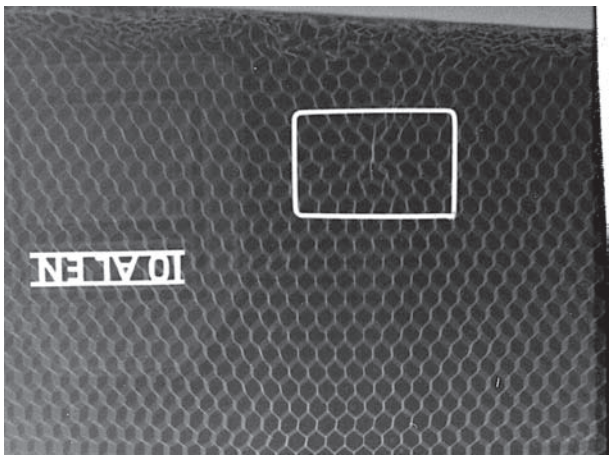

Fig. 8. Digital image of honeycomb structure airplane wing fragment with defective rectangle zone selected for further testing by digital solid-state transducer S10811-11of Hamamatsu Company (Japan).

Rys. 8. Obraz cyfrowy fragmentu skrzydła samolotu o strukturze plastra miodu z wadliwą prostokątną strefą wybraną do dalszych testów cyfrowym przetwornikiem półprzewodnikowym S10811-11 firmy Hamamatsu Company (Japonia).

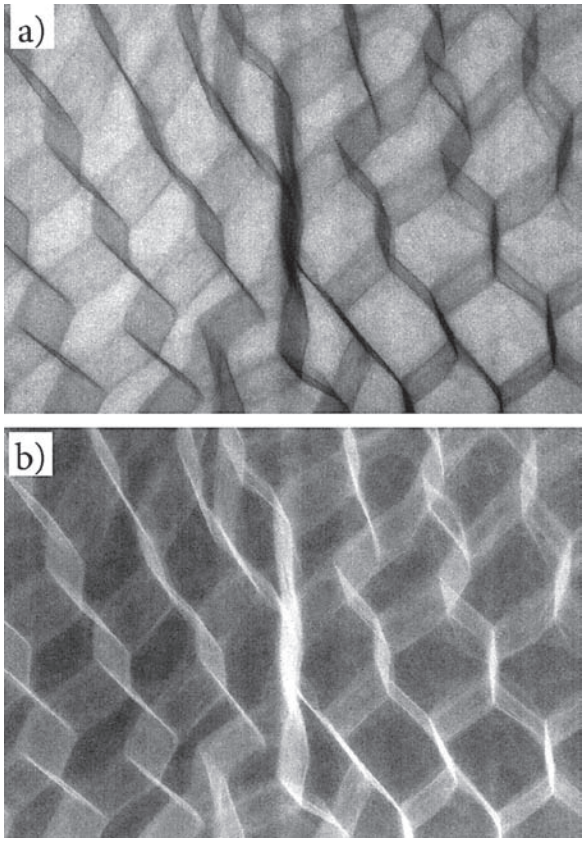

Fig. 9. Digital image of honeycomb structure airplane wing fragment get with digital solid-state transducer S10811-11: a – positive; b – negative

Rys. 9. Obraz cyfrowy fragmentu skrzydła samolotu o strukturze plastra miodu otrzymany cyfrowym przetwornikiem półprzewodnikowym S10811-11: a - pozytyw; b - negatyw

Thus, a success of X-ray mini technology is in its software. Each object has robotics-realized individual programs. It is performed on the customer's request depending on technological processes using X-ray mini technology. The E. O.

Paton Electric Welding Institute manufactures scanners for X-ray mini and releases corresponding software. X-ray mini testing can have complete or partial automation.

There is an opportunity to create highly effective X-ray technologies combining common X-ray testing and X-ray mini technology. As an example, Figure 8 shows honeycomb structure airplane wing fragment testing. At first the airplane wing was tested by common X-ray (160x120mm working area), then it was selected defective rectangle zone having imperfections, then it has been tested by digital solid-state transducer S10811-11 of Hamamatsu Company (Japan) having 34x24 mm working area. Figure 9 shows 7 times increased digital image of defective zone get with such compact solid-state transducer S10811-11.

4. Conclusions

1) Flash-radiography with digital solid transducers is the most perspective technology. It can provide sensitivity up to 0,1% thickness of inspected metal at resolution, exceeding 10 lp/mm. Besides, this technology is compatible film radiography, i.e. can be carried on the same X-ray equipment. All branches of industry need a quick and cheap FR.
2) Application of small-size movable solid transducers opens new technological capabilities. Solid transducers can be set and moved in the zones where positioning of cartridges with films and storage plate is virtually impossible. Digital solid transducer reveals new process capabilities for non-destructive testing, being not available for other physical methods. X-ray mini technology is an expanding application of NDT in industry.
3) The R-transducer and R-emitter in X-ray mini technology should move on agreed trajectories with recording at each exposure: time, coordinates, energy, and distance to object, orientation in relation to each other.
4) Current equipment allows producing the R-detectors and R-emitters of very small size, therefore, X-ray mini technology expands the capabilities of NDT for inspection of the objects of any complex geometry, and require automation of radiation testing process.

5. References/Literatura

[1] Troitskiy V.A. Flash-radiography// NDT Territory, 2013. No.4. P. 44-49.
[2] Mayorov A.A. Digital technologies in radiation testing //In the world of non-destructive testing. 2009. No.3. P. 5-12
[3] Troitskiy V.A., Mikhaylov S. R., Pastovenskii R. A., Shilo D. S. Current systems of non-destructive radiation testing // Technical diagnostics and non-destructive testing, 2015. No.1. P. 23-35.
[4] Stepanov A.V., Lozhkova D. S., Kosarina E. S. Computer radiography of results of practical investigations on possibility of replacement of film technologies. M.: VIAM, 2010.
[5] Grudskiy A.Ya., Velichko V. Ya. Digitization of radiographic images is not very simple// In the world of non-destructive testing. 2011. No.4. P. 74-76.
[6] Tsvetkova N.K., Novitskaya K. A., Kologov A. V., Smirnov V. G. Peculiarities of application digital radiography complexes in non-destructive testing of body production // Machine-building technologies. 2014. No.7. P. 47-50.
[7] Varlamov A.N. Experience of operation of digital radiography complex under field conditions // In the world of non-destructive testing. 2014. No.3 (63). P. 25-28.
[8] Kokkoori S., Wrobel N., Hohendorf S. et al. Mobile High-energy X-ray Radiography for NDT of Cargo Containers // Materials Evaluation. 2015. V. 73. N 2. P. 175 – 185.
[9] Duerr NDT GmbH and Co. KG. URL: http://duerr-ndt.de/ru/product. Panels NDT.net.
[10] Zscherpel U., Ewert U., Bavendiek K. Possibilities and Limits of Digital Industrial Radiology: The new high contrast sensitivity technique. Examples and system theoretical analysis. Lyon, 2007.
[11] Yatsenko S. Ya., Kokorovets Yu. Ya., lozenko A. P. et. al. X-ray television systems "Polyscan"// Technical diagnostocs and non-destructive testing
[12] Troitskiy V.A.: Method of welded joint radioscopic testing. Patent of Ukraine No.113257 of 25 January, 2017
[13] Troitskiy V.A. Non-destructive testing of multilayer welded structures// Insight. 1997. Vol. 39. No. 9
[14] Troitskiy V.A. Manual for welded joints non-destructive testing, Kiev, "Feniks", 2006, P.320.

Badania Nieniszczące i Diagnostyka
Nondestructive Testing and Diagnostics

LISTA RECENZENTÓW W ROKU 2017

1) dr hab. inż. Maciej Roskosz, prof. nadzw. AGH w Krakowie
2) prof. dr hab. inż. Piotr Bielawski, AM w Szczecinie
3) dr hab. inż. Jacek Szelążek, prof. nadzw. PAN
4) mgr inż. Jędrzej Hlebowicz, Pro Novum Sp. z o.o.
5) prof. dr inż. Ryszard Sikora, emerytowany prof. ZUT w Szczecinie
6) dr hab. inż. Jarosław Chmiel, prof. nadzw. AM w Szczecinie
7) dr hab. inż. Bernard Wichtowski, emerytowany pracownik ZUT w Szczecinie
8) dr hab. inż. Jacek Słania, prof. nadzw. IS w Gliwicach
9) dr inż. Grzegorz Jezierski, Politechnika Opolska
10) dr inż. Michał Kawiak, ZUT w Szczecinie
11) dr inż. Adam Sajek, ZUT w Szczecinie
12) mgr inż. Marek Lipnicki, Koli Sp. z o.o.
13) prof. dr hab. inż. Tomasz Węgrzyn, PŚl w Gliwicach
14) dr hab. inż. Jaromir Mysłowski, ZUT w Szczecinie
15) dr inż. Grzegorz Jezierski, Politechnika Opolska

BAKER HUGHES
a GE company

Channel Partner

Popraw dokładność swoich pomiarów z technologią Real3D Measurement, jedyną z pełnym obrazowaniem 3D.

Real3D Measurement - Połączenie trójwymiarowego modelu, zaawansowanych algorytmów pomiarowych oraz wiernego odwzorowania widoku modelowanej powierzchni umożliwia precyzyjne, wiarygodne i powtarzalne pomiary.

Prezentacja ruchomego i skalowalnego modelu, z naniesioną maską rzeczywiście obserwowanej powierzchni, umożliwia wiarygodną weryfikację umiejscowienia wybranych punktów pomiarowych, eliminując dotychczasowe pomyłki.

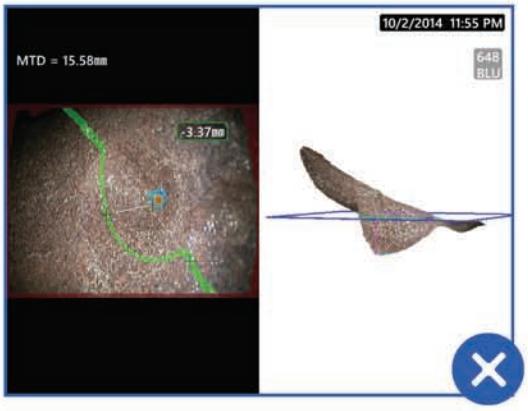

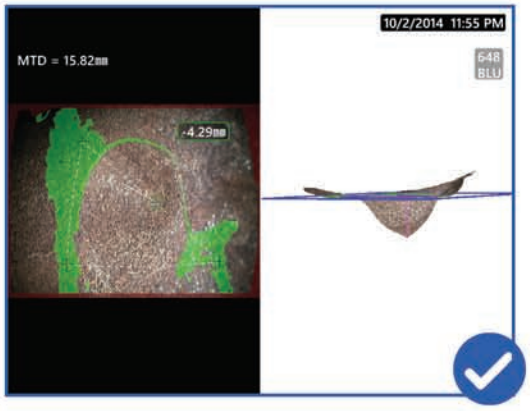

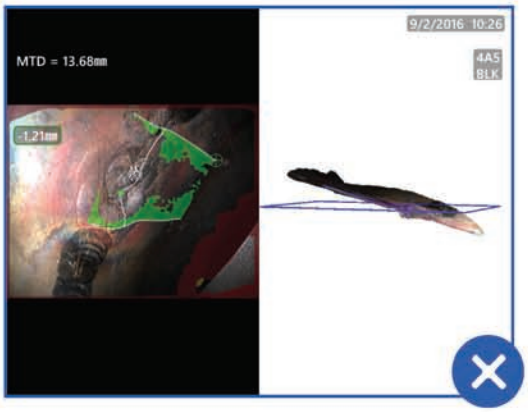

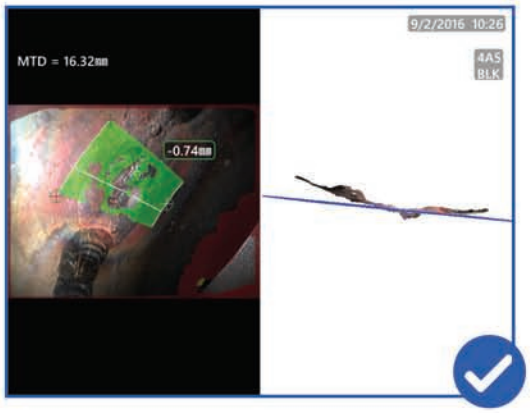

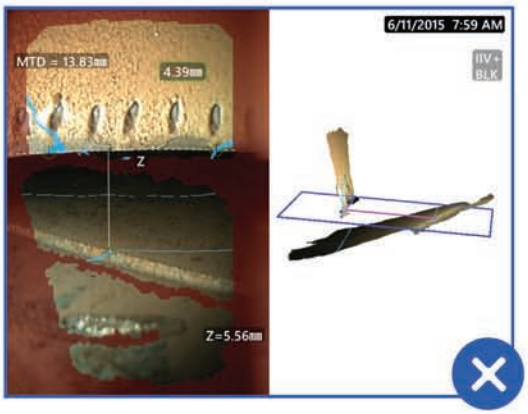

Niepoprawne umiejscowienie kursorów pomiarowych widoczne na modelu 3D

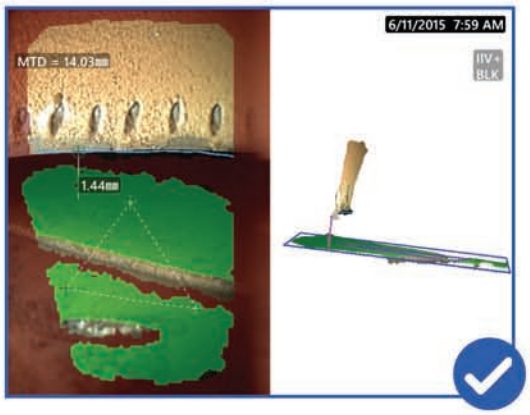

Poprawne umiejscowienie kursorów pomiarowych widoczne na modelu 3D

technologia badań wizualnych
Everest Polska

Everest Polska Sp. z o.o. ul. Geodetów 176, 05-500 Piaseczno k. Warszawy
tel. (+48 22) 750 50 83, faks: (+48 22) 750 70 21, email: everestvit@everestvit.pl, **www.everestvit.pl**

Konferencja "Szkolenia i certyfikacja personelu NDT w TÜV Rheinland Polska"

W dniach 5-7 czerwca 2018 roku w hotelu Holiday Inn w Łodzi odbyła się konferencja na temat działalności szkoleniowej i certyfikacyjnej personelu NDT w TÜV Rheinland Polska.

W konferencji wzięło udział ponad 70 uczestników reprezentujących szerokie spektrum branży przemysłowej oraz usługowej.

Otwarcia konferencji dokonał Janusz Grabka – Prezes Zarządu TÜV Rheinland Polska. W swym wystąpieniu nawiązał do historii firmy oraz momentu podjęcia decyzji o wprowadzeniu szkoleń i certyfikacji personelu NDT w TÜV Rheinland Polska.

Prezentacji działu szkoleń i certyfikacji osób dokonała Anna Konewecka – Dyrektor Działu Szkoleń i Certyfikacji Osób.

Obowiązujący system certyfikacji osób przedstawił Roman Gruca – Kierownik Sekcji Certyfikacji NDT.

20-letnią historię jednostki szkoleniowej, zmiany, które zachodziły na przełomie lat oraz dalsze kierunki rozwoju przedstawił Marcin Rasek – Kierownik Sekcji Szkoleń Personelu NDT.

Konferencja była również okazją do zaprezentowania aktualnych trendów w obszarze badań nieniszczących. Wśród tematów. jakie pojawiły się na konferencji można wymienić:

- Badanie szczelności LT jako alternatywna metoda badania urządzeń ciśnieniowych.
- Ochrona przed korozją wg EN 1090 w teorii i praktyce.
- Zastosowanie mikrotomografii komputerowej do kontroli jakości wyrobu w procesie produkcyjnym.
- Opracowanie planu badania w oparciu o wymagania normatywne dla techniki TOFD oraz Phased Array.

Oprócz ciekawej merytoryki przedstawionej na konferencji uczestnicy mogli wymienić się również własnym doświadczeniem i pozyskać nowe kontakty. co sprawiło, że wydarzenie sprawdziło się jako platforma do nawiązywania relacji biznesowych i poszerzania wiedzy.

Volodymyr Troitskiy*
The E.O.Paton Electric Welding Institute of the National Academy of Science of Ukraine

News in maintenance of technical state of the main pipelines

Wiadomości z zakresu utrzymania stanu technicznego rurociągów głównych

ABSTRACT

Long-term accident-free operation of the main pipelines depends on monitoring of their technical state, level of their maintenance, realization of physical methods of their diagnostics. Currently used types of main pipeline marking system, which should be replaced with individual bar and QR codes, are considered. This allows combining the information capabilities of various diagnostic systems, repairs and examinations, maintain an individual history of each pipe and monitor pipe operation with allowable defects for underground pipelines.

Keywords: *Pipeline degradation, pipeline diagnostics, pipeline marking system, code plate, bar code panel, low-frequency ultrasonic, magnetic diagnostic, polarization potential, marker pipe*

STRESZCZENIE

Długoterminowa bezawaryjna praca głównych rurociągów zależy od monitorowania ich stanu technicznego, poziomu ich utrzymania i prowadzenia fizycznych metod diagnostyki. Rozpatrzono obecnie stosowane rodzaje oznaczeń głównych rurociągów, które należy zastąpić indywidualnymi kodami paskowymi i kodami QR. Umożliwia to łączenie informacji o różnych systemach diagnostycznych, naprawach i badaniach oraz utrzymywanie indywidualnej historii każdej rury i monitorowanie pracy rurociągu z dopuszczalnymi defektami dla podziemnych rurociągów.

Słowa kluczowe: *Degradacja rurociągów, diagnostyka rurociągów, systemy oznaczeń rurociągów*

1. Introduction

Pipelines consist of various pipe. This difference starts from on-reception inspection of metal sheet, which is used for pipe formation, present production defects and performance of welds in the pipeline. All this allowable defects are present in each pipe in various amounts.

The factors, limiting a period of operation of underground pipelines, are propagating multiple initial defects as well as processes of stress-corrosion, material degradation, fatigue and electrochemical processes. Therefore, regular diagnostics, productive organization of pipe monitoring are the main activities on maintenance of working capacity of specific pipes of underground main pipelines.

Number of defects, detected only at in-line diagnostics of linear parts of the pipelines can make hundreds per 1 km. Their simultaneous removal is very labor-consuming tasks and unpractical. However, the zones with defects should be monitored. Current methods of calculation of limiting state of pipe structures with thinning, cracks, measured geometry anomalies allow high reliability prediction of their residual strength, determination of defects of critical size (requiring immediate removal) or medium (do not requiring immediate removal). Accuracy of such calculations depends on peculiarities of specific part, age and resistance to different types of fracture. Therefore, it is necessary to give preliminary evaluation to all found defects and determine sequence of their removal. A level of danger in the world's practice is marked by color. Pipes with defects can have three colors, namely red, orange and grey. This method can be used for ranking defective zones and attracting attention of services and specialists engaged in pipeline operation. These colors should be indicated on markers of defective zones, pipeline fixture elements, structures subjected to repair and markers provided by process documentation.

In the case of postpone of repair of found defects' the color indications will help to find these zones for their monitoring with some frequency. Besides, in addition to defectiveness problem, all pipes (stalks, sections) should have own codes (numbers), being brought to the surface and read with in-line and manual flaw detectors. Such rules should be embedded in technical documents. These innovations are necessary for safety of the main pipelines being built and reconstructed.

It is well known fact that external pipelines have longer life than underground pipelines. Famous Alyaskinskii oil pipeline, which pumps aggressive oil, has been under operation for more than 60 years and will be used for many years more. Service life of underground oil-and-gas main pipelines can be approximated to time of existence of ground pipelines under conditions of equal maintenance of each pipe in the pipeline. For this, they should have own numbers and maximum information about them should be brought to line surface. Pipe state can be easily examined without significant damages and mechanical loads.

Various types of diagnostics are used for underground main oil-and-gas pipelines. Their number continuously increases. The most common among them are:

- in-line [1,7] magnetic (acoustic);
- low-frequency [2] ultrasonic (guided wave);
- electrometric [3, 4] of insulation;
- coercive-metric;
- magnetometer [5] based on magnetic memory;
- acoustic emission;
- thermographic [2, 7], visual-optical etc.

*Correspondence author. E-mail: ndt@paton.kiev.ua

DOI: 10.26357/BNiD.2018.011

Each of these 8 types of tests provides its specific information on underground pipelines, which is only considered by repairmen after it has been confirmed through excavation and manual flaw detection means. For this test boring and opening of one or several pipes are carried out. Currently, application of the defectorgams from each of the mentioned types of diagnostics do not allow indicating a pipe having dangerous defects, since these underground pipes are anonymous, i.e. do not have their own numbers (codes). This uncertainty provokes a lot of problems including reduction of pipeline safety.

All mentioned above physical methods of technical diagnostics have their own origin points and coordinate measurement instruments, rules and means of connection of their results mainly to line surface, but not pipe body. GPS space navigation systems are often used fir this. Therefore, it is difficult to compare the results of different types of diagnostics, which should complement each other. The first (overrun, unnecessary rejection) and the second (shortage, flaw detection skipping) types of errors are very significant for each type of test in comparison of the results of each diagnostics type. The repair services have the most problems with the anonymous pipes. We are going to describe some types of diagnostics, the results of which can be clarified and combined by pipe numeration that allows following life time of each pipe.

Figure 1 shows a scheme for monitoring an insulation condition by measurement of pipeline polarization potential [3, 4]. It is used to study the influence of aggressive ground environment, which leads to insulation and pipeline metal failure. Anti-corrosion protection is used for metal protection and it is periodically checked. Insulating coating and cathodic polarization protect the underground pipelines from corrosion. The main criterion of isolation condition [3, 4] is the difference of potentials between metal and medium, called a polarization potential. The potential should be controlled and maintained within a certain range in electrically conductive medium, avoiding the errors of the first and second type. Special, accurate electron devices are used for that.

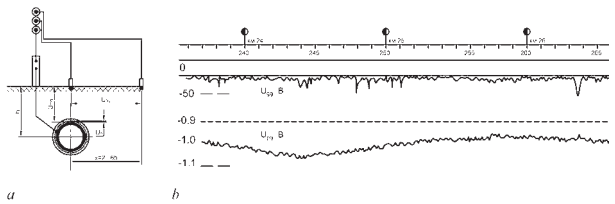

Fig. 1. Evaluation of quality of pipeline insulation based on results of measurement of polarization potential Up: a – scheme; b – measurement results, Umg – potential between pipe and electrode, Ugg – the same at x distance from axis, h – pipeline burial depth

Rys. 1. Ocena jakości izolacji rurociągów na podstawie wyników pomiaru potencjału polaryzacji Up: a - schemat; b - wyniki pomiarów, Umg - potencjał między rurą a elektrodą, Ugg - potencjał jw. w x odległości od osi, h - głębokość umiejscowienia rurociągu

Such an inspection of underground pipelines by electrometric methods (electrodes) from land surface can be contact (Figure 1) and non-contact. The latter significantly increases the efficiency, but do not provide reliable information. There are many original solutions in this type of diagnostics. Figure 1 shows a simplified scheme for measurement of the polarization potential [3, 4]. It presents a measurement point, an electrode buried in the ground at every 5 to 15 meters along pipeline axis and additional electrode, moved parallel to axis at (2-6) h distance. Such a configuration of the measurement point for tens and hundreds of meters along the route allows obtaining distribution of "pipe-to-ground" transient resistance, insulation resistance, "ground-ground" potential distribution and Up - polarization potential along the pipe, assess of the pipeline insulation condition and necessity in its opening and repair.

Figures 2, 3 and 4 show the examples of realization of magnetometric [5] and low-frequency [2, 13] ultrasound diagnostics. Each of these types of tests, as well as in-line diagnostics [1, 7, 11], is realized with the help of special flaw detectors. Their authors try to connect the obtained results to the pipeline body through their own auxiliary means, their origin points, and so on. The magnetometric method (Figure 2) determines the stress concentration zones. These areas with full insulation can contain metal thinning and other defects [5]. In this case magnetogram as well as the results of measurement of the polarization potential are not refereed to specific pipes.

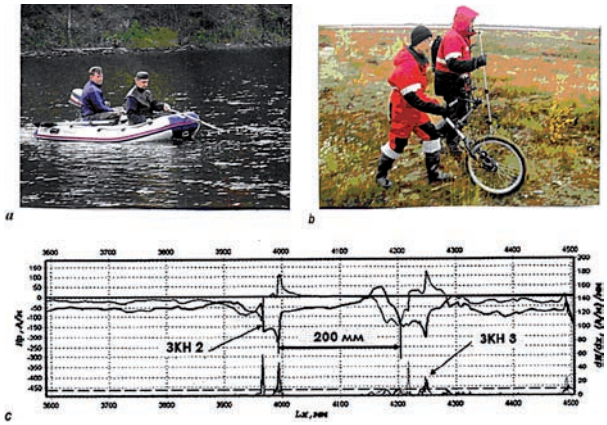

Fig. 2. Magnetometric diagnostics determining stress concentration zones (scz): a, b – measurement process; c – surface distribution H (A/m) of magnetic field intensity and its gradient dH/dx along main pipe axis

Rys. 2. Diagnostyka magnetometryczna wyznaczająca strefy koncentracji naprężeń (scz): a, b - proces pomiarowy; c - rozkład powierzchni H (A / m) natężenia pola magnetycznego i jego gradient dH/dx wzdłuż osi głównej rury

Figure 3 shows an example of diagnostics of main pipeline using low-frequency (LF) [2, 13] ultrasonic testing (UT). In this case, measurements and origin of coordinates takes place from location of a circular antenna on pipe body. This is already somehow more specific point of origin of examined object body. The method of low-frequency ultrasonic testing (LF UT) on new pipelines can provide information on quality of large number of circular assembly joints in the main pipeline of several kilometers. It is necessary to do before pipeline is buried. Wear of pipeline structure can be evaluated on length of penetration of LF-oscillations in

metal. Long-range LF UT is successfully used for diagnostics of various pipelines, including the Alaska oil pipeline.

Work [13] describes an interesting experience of application of LF UT, where this method was used for diagnostics of 74 km of technological pipelines. LF UT helped to find 1345 defects with more than 20% pipe wall thinning. Size of thinning was specified by ultrasonic thickness gauges. At that, 263 unallowable defects with wall thickness less than the reject level and 230 defects with wall thickness close to the reject value (plus 0.5 mm) were identified. The first (263) were subjected to immediate repair, the second group (230) was referred to the nearest scheduled repair. The rest of damaged places 1345 - 263 - 230 = 852 (more than 20% of thickness) should be monitored i.e. should be periodically found in the lines and tested. Obviously, that numeration of the pipes can help to find each of 852 + 230 = 1082 places in the pipelines. It is already done for external lines. Let's show how to do this for underground pipelines. Numeration of the pipes is particularly important for underground pipelines, which are out of direct contact of the line inspectors.

Fig. 3. Low-frequency ultrasonic diagnostics
Rys. 3. Diagnostyka ultradźwiękowa o niskiej częstotliwości

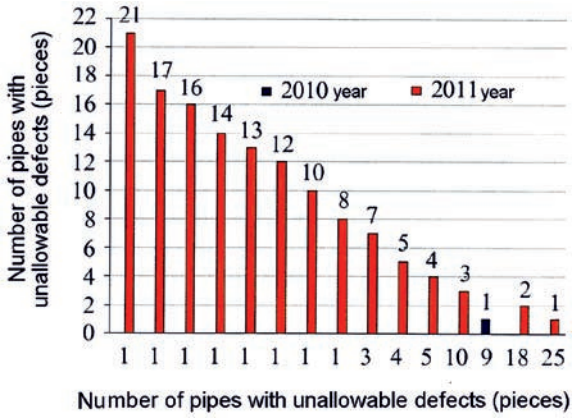

Fig. 4. Diagram of distribution of unallowable detects, pc/pipeline (9 pcs. – 2010, 263 pcs. - 2011)
Rys. 4. Schemat rozmieszczenia niedopuszczalnych defektów, pc / pipeline (9 szt. - 2010, 263 szt. - 2011)

Figure 4 shows [13] a diagram (2011) of pipe-by-pipe distribution of unallowable defects. In this case some pipes have up to 21 unallowable defects. 7 unallowable defects were found in three pipes, and one in 25 pipes. It is characteristic that last year (2010) this company did not use LF UT method and found only 9 pipes with unallowable defects in 74.2 km of pipelines, whereas according to data of 2011 these pipelines had a lot of defects. Reporting for both external and underground pipelines should be made strictly pipe-by-pipe (Figure 4). Pipe-by-pipe record of state is the main peculiarity of ground pipelines in contrast to underground pipelines. Therefore, they have longer life than underground ones. Introduction of numeration, record of real state of each pipe will extend service life of the underground pipelines. At that, each type of diagnostics and repairs receives the possibility to provide the results connected with external (surface) attributes of the line as well as a specific pipe. Then separate types of diagnostics will complement each other, and repairmen will not pay for existing uncertainty. For example, the diagnostics indicates dangerous defects, but manual NDT does not find them because wrong part of the pipeline was opened. Thus, it is nothing to repair. This problem is absent in ground pipelines. The reason of this problem is that the pipes are anonymous.

All enumerated types of diagnostics provide their own important data on the peculiarities of line local places. Not all places identified by that or another type diagnostics are intolerable for further operation. At the same time this zone for another type of diagnosis can be critical, unacceptable for further operation without repair. Therefore, it is important to compare the results of different diagnostics. All numerous types of line state observation can be compared with each other if they have unified system of coordinates, namely pipeline with numerated pipes (assembly welds), each of which has its own history of aging, repairs and defect development. This information should be known to line inspectors, who should easily find location of special pipes.

In-line inspection is the most expensive among all listed types of diagnostics. In-line flaw detectors are continuously improved, the volumes of information provided by them are rising. Inhomogeneities, thinning and other deviations from the standard after defectograms decoding should be found and discussed for a specific pipe following the recommendations of the diagnosticians. In present time a necessary pipe is selected by indirect signs, for example, by the distance from a certain reference mark, which is visualized on the defectogram and can be easily found on line surface. The distance from the reference mark to the pipe, location of test boring place can make hundreds of meters. Therefore, error possibility in determination of excavation point is very high. Old pipelines, except for «nothing to repair" problem, have more dangerous problem, namely "excessiveness". It happens when manual flaw detection finds more flaws than in-line flaw detector. At the same time, something was repaired, but not the most dangerous place, which had not been excavated. Therefore, it is necessary to open large sections of line due to pipes anonymity and uncertainty.

Taking into account these and other reasons, a pipe coding (numeration) system, being well readable on defectogram and by manual devices, should be used for pipeline reconstruction. Today, various indirect systems [9, 10, 11] are

used for main line marking. They are based on application of marker plates, reference marks, specially marked tubes (Figure 6) etc. located on pipe body. Markers on pipe body do not completely cover all uncertainties and discussions mentioned above.

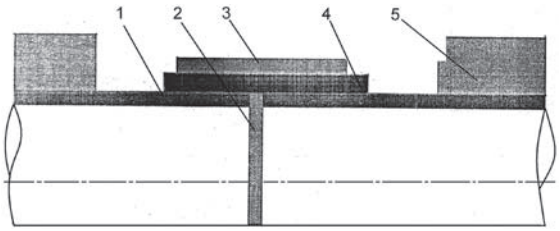

Fig. 5. Location of marker plates in pipeline: 1 – pipe wall; 2 – circumferential assembly weld; 3 – yoke; 4 – marker plate; 5 – concrete

Rys. 5. Lokalizacja tabliczek znamionowych rurociągu: 1 - ściana rury; 2 - obwodowa spoina montażowa; 3 - jarzmo; 4 - tabliczka znacznikowa; 5 - beton

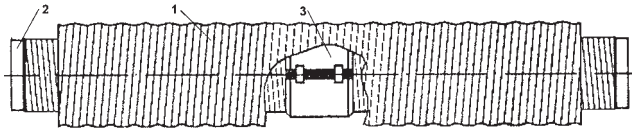

Fig. 6. Marker pipe: 1 – ballast coating; 2 – pipe body; 3 – marker KD 13229.00.000

Rys. 6. Rura znacznika: 1 - powłoka balastowa; 2 - korpus rury; 3 - marker KD 13229.00.000

Work [11] describes marking employing cover marker plates (Figure 5), being located along pipeline on butt joints of separate pipes and corresponding reference marks on line surface. The latest achievement in this series of marks is the marking [11] based on marker tubes, which can be distinguished on defectogram (Fig. 6). They are manufactured under plant conditions and located in line during every 1 - 2 km. It is necessary to read off the long distances moving along the line surface from the reference mark to the marker pipe in order to find a defective pipe. Transfer of information about defect location from the defectogram, which does not take into account peculiarities of line surface relief, is complicated. This is one of the reasons of errors at transfer of the information about defect surface location for determination of excavation place. All detected defects should be found, most of them can be easily identified on line surface at available pipe numeration. .

The code bands (Figure 7), located in a zone of circular assembly weld, can be used as bar code elements in the simplest case, for example, for small diameter pipes. For larger diameter pipes, the bar code can be in a form of panel with code elements (Figure 8) or plate with code holes (Figures 9-13). Thus, there are three constructive possibilities of pipe code formation. A code (number) can be formed for each assembly weld from a specific combination of code elements. These can be bands, panel code elements or holes in a plate. Each of these systems has its own characteristics for manufacture, reading and receiving volumes of information.

The advantage of bar codes based on marker bands lies in suitability for any diameter, their complete identification by in-line flaw detector, since the code bands is a noticeable thickening of metal along the whole pipe generatrix. Such a code is impossible to miss.

Markers bands (Figure 7), located in a zone of assembly weld before insulation, are made of elements of tube metal and tightly abut on pipe surface. They can be multi-element or strip.

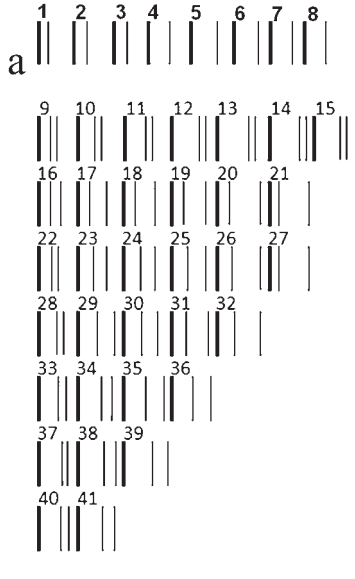

Fig. 7. Formation of bar code due to removal of one (a)or two (b) bands (thin line) from assembly welds (thick line)

Rys. 7. Tworzenie kodu kreskowego w wyniku usunięcia jednego (a) lub dwóch (b) pasm (cienka linia) ze spoin montażowych (gruba linia)

A form, structure of band elements, its distance to assembly weld, and distance between separate elements of the bands (Figure 8) can also be used as informative characteristic of the barcode. These characteristics can be used for identification of hundreds of joints.

If such a bar code is made only at every five joint, i.e. every 4 pipes, then only 20 joints should be marked for a section of 100 pipes.

Figure 7a shows positioning of an isolated strip band near assembly weld (a.w.) at different distances. In this case 8 assembly welds, outlined in Figure with bold lines, were marked in such a way. A thin line is a strip or composite code band, located to the right of a.w. A set of bar codes can be formed by positioning of similar bands also to the left of a.w., i.e. in the direction or against the direction of transported product movement.

Figure 7b represents marking of a.w. similar to marking of Figure 7a, but with the help of two bands. The number of markers is significantly increased in this case due to the distance between bands and a.w. 33 of them are shown in Figure 7b, and total number of bar codes in Figure 7 makes 41. One-strip and two-strip bands from Figure 7 lie on the right of a.w. They can also be located in the same way to the left of a.w. Then the total number of bar codes increases to 82. This at 12 m pipe length allows marking each pipe of 984 m line. Multilink complex bands provide much more possibilities for bar code formation in comparison with strip bands. Only two characteristics are examined in Figure 7, namely

amount (2) and distance. Additionally, if structural design of barcodes (Figure 8) are taken into account, then the number of codes will grow by an order of magnitude.

Formation of barcodes should be described in technical documentation, where codes and pipe numbers (a.w.) corresponding to each other should be indicated in form of tables similar to Table. No. 1, made for a QR code with two holes of 15 possible.

Bar code panels are recommended (Figure 8) for large diameter pipes. In them short straight code elements are similar to the bands.

Let's calculate how many variants of the bar code can be obtained with 5 and 10 variants of the elements' structures, which can be located close to a.w. or at some distance (2 indications). Marker elements (bands) can be located before a.w. or after a.w. (2 indications).

Thus, 5 variants of element structures (bands) will have 9 distinctive variable indications, and that for 10 variants of such indications will make 14. Let's calculate number of combinations (number of codes) for these cases: $A_9^3 = 9 \cdot 8 \cdot 7 = 504$, $A_{14}^3 = 14 \cdot 13 \cdot 12 = 2184$. In this case all pipe at approximately 5 and 22 km of the line will be able to have own unique codes.

Well-known formula $A_m^n = m(m-1)(m-2)...[m-(n-1)]$, where number of locations equals product of n consequent whole numbers, from which m is the largest.

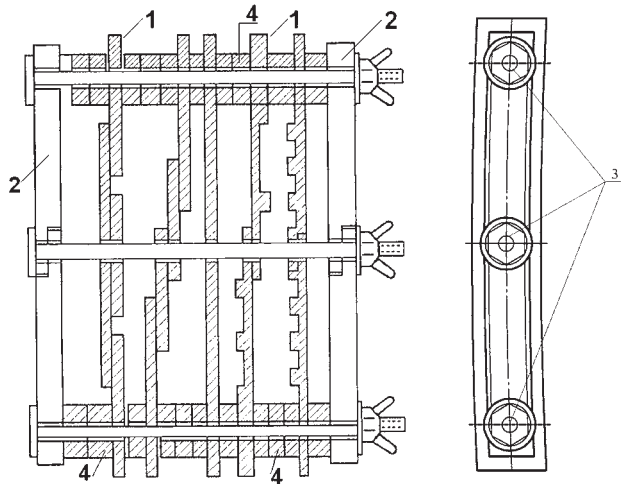

Fig. 8. Bar code panel consisting of 5 different code elements, combination of which determines pipe number: 1 – code elements; 2 – cheek, 3- strengthening pins
Rys. 8. Panel kodów kreskowych składający się z 5 różnych elementów kodu, z których kombinacja określa numer rury: 1 - elementy kodu; 2 – panel czołowy, 3 szpilki wzmacniające

For large diameter pipes, the bar codes can be made in the form of code panels consisting of short code elements of different geometries. Figure 8 shows an example of such a code panel consisting of five code elements.

The panel in Figure 8 represents a set of code elements assembled on pins with plugs determining the distance between bar code elements. Variation of the set, structure of elements and distance between them forms the codes similar to bar codes from bands shown in Figure 7. A numeration system can start with use of one element, then two or three of the same type, further - different bar code elements. The code panel is located in a near-weld zone of assembly weld before its insulation.

The bar code panel in Figure 8 consists of a set of code elements and auxiliary parts, namely two jaws, plugs and three strengthening pins. The latter, in order not to be visible on the defectogram, should be made of non-ferromagnetic metal, have thickness, diameters and other sizes smaller than the size of the bar code elements. Under these conditions the defectogram will show only the bar code elements without auxiliary parts.

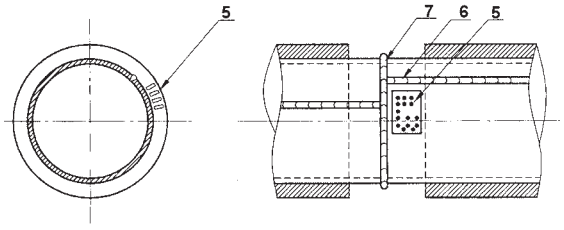

Fig. 9. Position of code panel (5) in zone of intersection of longitudinal (6) and assembly (7) welds
Rys. 9. Położenie panelu kodującego (5) w strefie przecięcia spoin wzdłużnych (6) i montażowych (7)

Each group of information and code elements should follow the applicability hierarchy taking into account their readability on the defectogram. If readability of bar codes depends on direction of magnetization, it has no influence on detection of QR codes. Let's consider the possibilities of QR codes.

Figure 9 shows location of QR code plate 1 in the intersection of circular assembly 3 and longitudinal welds 4. There can be a lot of options for QR codes, their design and meaningful filling. Let's describe four fundamentally different systems for development of QR code designations. They all suggest presence of ferromagnetic plate with holes located on the pipe body.

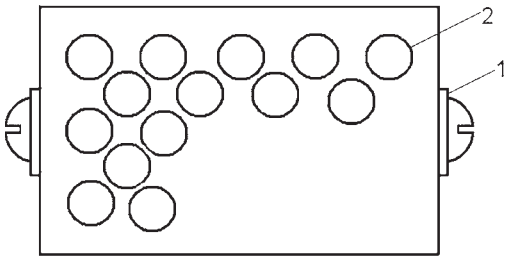

Fig. 10. Marker plate with 14 randomly located holes, amount of which correspond assembly weld number (No. 14)
Rys. 10. Tabliczka z czternastoma losowo rozmieszczonymi otworami, których ilość odpowiada liczbie spawania (nr 14)

Formation of bar code panels in Figure 8 and their assembly on site requires some intellectual efforts. It is much easier to produce and read QR code panels (plates) with holes (Figures 10 - 13). The simplest QR code (Figure 10) is when amount of holes in the plate equals the number without any combinations. Holes' amount corresponds to actual number. This is the simplest possibility of numeration (Figure 10). A more complex variant is to write a code number using the holes as shown in Figure 11. If the holes in Figure 10 plate

can be made in random order, then Figure 11 marker plate shows the code number that belongs to pipe number 9175. A lot of holes is necessary in the first (Figure 10) and in the second (Figure 11) variants.

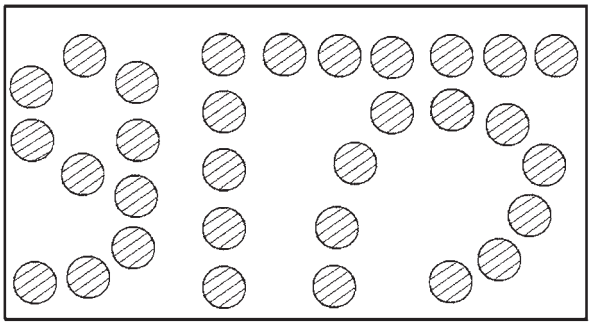

Fig. 11. Marker plate containing 55 points with fixed amount form 31 holes for pipe No. 9175
Rys. 11. Płytka znacznikowa zawierająca ustaloną liczbę możliwych 55 punktów z 31 otworami dla rury nr 9175

In this paper we want to show that even 2 - 3 holes made in the plates allow creating a huge amount of the codes (Figures 12 - 13). Multiplicity of QR codes is reached due to combination of several openings relative to determined points of their possible location.

Figure 12 shows a small plate including 15 determined points, which can have open holes. Opening of one hole in the determined point of such a plate allows getting 15 designations and opening of two similar holes provides 105 designations, as shown in Table 1. If, holes in this code plate have their own distinctive features, for example, one of the two holes has a different diameter, then amount of such codes is doubled and equals 210.

$N = A_m^n = m(m-1)...= A_{15}^2 = 210$ formula is used in order to calculate total amount of variants from 15 with two. In this case each plate has two different holes.

If both holes have the same diameter, i.e. do not have own peculiarities, then amount of codes reduces two times and equals $N = A_n^m/n - 105$. They are given in Table 1. For example, holes number four and twelve should be opened on the code panel for designation of a.w. with number 47, according to Table 1.

Figure 13 shows the code plate which is two times larger than that in Figure 12. It has two times more (30) determined points for the holes than in the plate of Figure 12. Moreover, the holes can be of different and equal diameters. If only one hole of similar diameter is opened in such a plate, then $N_1^1 = 30$ a.w. can be designated, and if two holes (Figure 13b) of the same diameter are opened, then the number of codes will equal $N = A_{30}^2 = 435$. If two holes of different diameters are opened, then $N_{30}^2 = A_{30}^2 = 870$. If three holes (Fig. 13c) of different diameters are opened in the same way, then amount of codes will equal $N_{30}^3 = 24360$. It is already too much. Thus, it is possible to mark all the pipes in the line of 24.360 x 12 = 292.320 m ≈ 300 km length. Redundancy of possibilities is desirable to decrease, for example, by making only one diameter holes in order to facilitate understanding of QR codes application. Then $N_1 = 30$; $N_2 = 435$; $N_3 = 8120$ (~ 97 km).

Tab. 1. Correspondence of QR code to pipe number in form of two similar holes on plate with 15 possible points for holes
Tab. 1. Zależność kodu QR od numeru rury w postaci dwóch podobnych otworów na płycie z 15 możliwymi punktami na otwory

No a.w.	ø n_1-n_2	No a.w.	ø n_1-n_2	No a.w.	ø n_1-n_2	No a.w.	ø n_1-n_2	No a.w.	ø n_1-n_2	No a.w.	ø n_1-n_2	No a.w.	ø n_1-n_2
1.	1-2	17.	2-5	33.	3-9	49.	4-14	65.	6-11	81.	8-12	97.	11-13
2.	1-3	18.	2-6	34.	3-10	50.	4-15	66.	6-12	82.	8-13	98.	11-14
3.	1-4	19.	2-7	35.	3-11	51.	5-6	67.	6-13	83.	8-14	99.	11-15
4.	1-5	20.	2-8	36.	3-12	52.	5-7	68.	6-14	84.	8-15	100.	12-13
5.	1-6	21.	2-9	37.	3-13	53.	5-8	69.	6-15	85.	9-10	101.	12-14
6.	1-7	22.	2-10	38.	3-14	54.	5-9	70.	7-8	86.	9-11	102.	12-15
7.	1-8	23.	2-11	39.	3-15	55.	5-10	71.	7-9	87.	9-12	103.	13-14
8.	1-9	24.	2-12	40.	4-5	56.	5-11	72.	7-10	88.	9-13	104.	13-15
9.	1-10	25.	2-13	41.	4-6	57.	5-12	73.	7-11	89.	9-14	105.	14-15
10.	1-11	26.	2-14	42.	4-7	58.	5-13	74.	7-12	90.	9-15		
11.	1-12	27.	2-15	43.	4-8	59.	5-14	75.	7-13	91.	10-11		
12.	1-13	28.	3-4	44.	4-9	60.	5-15	76.	7-14	92.	10-12		
13.	1-14	29.	3-5	45.	4-10	61.	6-7	77.	7-15	93.	10-13		
14.	1-15	30.	3-6	46.	4-11	62.	6-8	78.	8-9	94.	10-14		
15.	2-3	31.	3-7	47.	4-12	63.	6-9	79.	8-10	95.	10-15		
16.	2-4	32.	3-8	48.	4-13	64.	6-10	80.	8-11	96.	11-12		

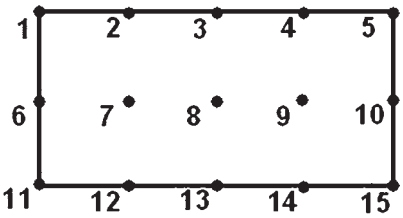

Fig. 12. Code plate with 15 possible holes for 105 and 210 QR codes
Rys. 12. Tabliczka z 15 możliwymi otworami na 105 i 210 kodów QR

Simple auxiliary capabilities can add necessary information. For example, it can be done by making notches on upper edge of code plate (Figure 13a) or varying determined location of the code, which is also easily determined distinctive feature.

Thus, the simplest from these three considered systems are QR codes based on holes in code plate, namely:

1) holes in random order (Figure 10b), amount of which determines the number;
2) digital image (fig. 11) in form of Arabic (1, 2, 3. ...) or Roman (I, II, III, ...) numbers;
3) combinations of 2 or 3 holes (Fig. 13b, 13c);
4) using one code hole, location of which determines the number (Figure 13a).

As can be seen from these figures, the system of QR codes with more than 3 holes is already redundant for pipe issues. Expansion of possibilities complicates understanding of QR codes. It is better to focus on periodic repetition of the simple codes with one or two bar elements or one or two holes after natural artifact of the line.

Since, there are no standards requiring pipe-by-pipe coding, a planner can develop own numeration systems. He can choose one of four listed QR code systems taking into account the peculiarities of expected construction or reconstruction.

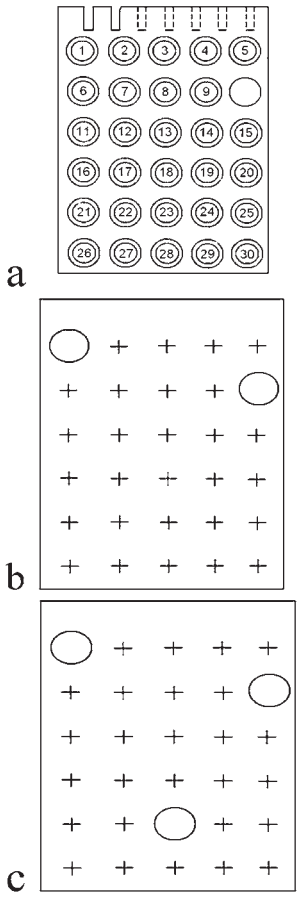

Fig. 13. Code plate: a) – with one (10) open hole from 30 possible and 7 possible notches on periphery; b – with two and c) – with three open holes
Rys. 13. Tabliczka znamionowa: a) - z jednym (10) otworem otwartym z możliwych trzydziestu i jednym wycięciem na obwodzie z siedmiu możliwych; b - z dwoma i c) - z trzema otworami

The simplest (Figure 13a) method providing sufficient information assumes opening every time of one different diameter hole and application of number of notches on plate periphery. Figure 13a shows two possible diameters and seven notches in code plate upper periphery. The side notches, amount of which corresponds to number of pipeline section, are the auxiliary informative peculiarities and can be used for additional coding of large number of pipes.

The pipe-by-pipe marking is important for underground as well as underwater pipelines, particularly in zones of not stable soil, including tectonic fractions, mountainous terrain, where stressed state of pipeline should be monitored. The environment determines a numbering method (codes) for periodic inspection and observation of separate pipes.

Accuracy requirements to underground pipeline marking systems will increase with rise of operation culture. The pipe-by-pipe marking will facilitate solution of disputable situations that arise periodically in underground pipelines during long period of their operation. Currently, different types of diagnostics are used for this (Figures 1-3). Thus, it is possible to provide monitoring of every pipe that was or should be repaired. All defects, which were found by in-line flaw detector, can be marked on route surface without line opening. The defectograms shows the codes and pipe defects, which should be brought to line surface. Thus, the principle of repair sequence according to defect hazard level (red, orange, gray) can be realized. The color on a route surface determines activities in relation to this pipe with defect.

The pipe coding system, outlined in the technical documentation, will reduce operating costs, time of maintenance and monitoring of individual pipes, and their repair, will promote reduction volumes of excavation work.

Sufficient simplified informative coding can be received using only two or three holes, two or three bar code elements. Pipes deviating from the norm should be periodically monitored by various means of non-destructive testing by means of point test boring without damaging adjacent zones of the pipeline. The exact location of the defect on specific pipe can be easily found on its defectogram and brought to the surface together with its number. The number is easily read by inspectors. Bar or QR code is read by devices and specialists, acknowledged with the technical documentation and conversion tables. Inspectors, diagnosticians and other personnel monitoring the route surface should clearly understand pipe numbers and level (color) of defect hazard. Thus, one of the main information differences in operation of underground and ground lines will be removed. The level of their damaging will be reduced because of decrease of excavation volumes.

According to data of [14], the largest portion of accidents (69%) in underground pipelines is related with external mechanical effect. 26.1% of accidents in the USA are caused by machines and mechanisms. Mechanical loads are created by unauthorized inserts. Complex automatic systems of quick preventive actions are developed to reduce this effect. Any type of quick reaction can be performed only at precise indication of a place of unusual sounds (noise from the mechanisms used for notches).

Everything that is located along the route should be used to bring pipe-by-pipe marking to the surface. These are pickets, measuring points, kilometer and intermediate posts, milestones, external communications crossing the route, including power lines, etc. Pipe markings (red, orange, gray) for defects of various hazards are of particular importance. Underground as well as ground pipes should be "identifiable" without excavations, they should have easy access. Any excavation, any trail boring is a trauma for pipeline, which should be minimized. The principle of "do no harm" will be realized only if the whole lifetime history of each pipe, its diagnostics, repairs, previous trail boring etc are taken into account during excavation.

In-line diagnostics [15] sometimes detects up to 150 - 200 defects per 1 km in certain oil product pipelines, corrosion depth of which reaches 60% of wall thickness of the pipe, regardless electrochemical protection. It is impossible to repair everything and at once. It is necessary to examine amount of defects in one pipe and determine complementary reasons for stress concentration in addition to thinning. There are a lot of such reasons. Therefore, it is impossible to find two identical pipes in one pipeline after long-term operation, repairs, various loads and effect of environment. All of them are different and require different preventive

works. Possibility of operation without repair or sequence of repair can't be determined without individual records for each pipe.

Conventional signs (Figure 14) from small pieces of strip (~ 10´20´5) or pipe metal, described in technical documentation, can indicate pipe peculiarities, which were determined in process of construction (reconstruction) of pipeline to the diagnosticians. These conventional signs, located in pipe body, can refer to mechanical damages of different origin, indicate the places of allowable defects, being left without repairs, zones being repaired by welding-up or other technology. The conventional signs of administrative nature can indicate work performer, repair reasons, date and other information. They can have decisive effect of determination on level of pipe risk and stating repair order.

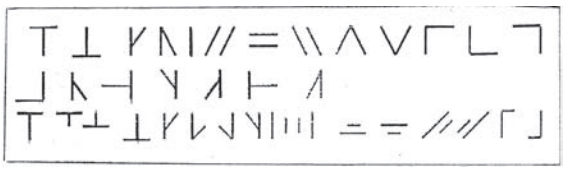

Fig. 14. Signs of technological peculiarities of reconstruction: remained defects, places of welding-up, repair, mechanical damages
Rys. 14. Oznaki cech technologicznych rekonstrukcji: pozostałe wady, miejsca spawania, naprawy, uszkodzenia mechaniczne

Construction organizations, which could master pipe coding and number them along the route, will be more popular than other. The authority of the inspectors indicating the number (code) of the problem tube in their reports will increase. Operators will learn how to mark the problem pipe categories and determine repair sequence without excavation using the defectorgrams of in-line flaw detector. Reduction of excavation volumes and mechanical effects will increase reliability and service life of underground pipelines. It is necessary to monitor every pipe taking into account its origin, life history, repairs and diagnostics in course of many decades. Only such an approach will ensure "longevity" of the whole pipeline.

2. Conclusions:

1) Natural allowable in manufacture and acquired in process of operation defects make all underground pipes different with various level of risk. Risk increases with age (degradation). Therefore, technical state, consideration of the results of repairs and diagnostics, strength calculations, planning of working capacity maintenance should be taken into account for each pipe, not by kilometers, i.e. specifically and individually. Thus, all pipes (sections) should have own numbers (codes), which can be read by in-line and manual flaw detectors.
2) Three-level used in the world practice color ranking of defective zones danger, which comes from grey to orange and red without repair and special measures, should be used for indication of different defects, number of which can be more than hundred per 1 km, and determination of sequence of repairs.
3) Numbers (codes) of pipe, location of ranked defective zones, their color location (risk) should be brought to the line surface, that facilitate their monitoring without test trials and excavations, i.e. as in the case with ground pipelines.
4) Combination of two-three bar code elements or combination of two-three holes on code plate located in pipe body under insulation in specific place, for example, near-weld zone at intersection of assembly circumferential and longitudinal welds, are enough for coding (numeration) of pipes (sections), which can be read in-line as well as manual flaw detection.
5) Ranking of defective zones requires the next sequence. Marking of defects is made without risk evaluation shortly after decoding of diagnostic defectograms. This provides a general pattern of defective zone location on the line surface. Further, risk level (color) and sequence of repair are determined after investigation of information on each defective pipe, performance of strength and expert calculations taking into account weight coefficients considering defect size and other peculiarities. Ranking of the defective zones without repair should be specified with time since risk level rises with age.

3. References/Literatura

[1] Abakumov A.A, Abakumov A.A. (ML). Magnetic diagnostics of gas pipelines. - Moscow: Energoatomizdat, 2001, 440 p.
[2] Paton B.E., Troitskiy V.A. The main areas of work of E.O.Paton Electric Welding Institute in improvement of non-destructive testing of welded joints. - Proceedings of the 8th National Conference UkrNDT-2016, p. 8-28.
[3] Tsykh V.S, Yavorsky A.V. Electromagnetic testing of isolation of underground pipelines from land surface. - Proceedings of the 8th National Conference UkrNDT-2016, p. 206-207.
[4] Dzhala R.M., Verbenets B.Ya., Melnyk M.I. New methods of testing of PKZ of underground pipelines by currents and potentials measurement. - Proceedings of the 8th National Conference UkrNDT-2016, p. 236-239.
[5] Dubov A.A, Magnetometric diagnostics of underground pipelines. www.energodiagnostika.ru.
[6] Construction of main pipelines. Reference book. Chirskov V.G., Berezin L.G. et. al. - M. Nadra, 1991. - 475 p.
[7] Non-destructive testing edited by Kluev V.V. Reference book in 8 volumes, 2010. Book I. Moscow, "Spectrum"
[8] Troitskiy V.A. Magnetic particle testing of welded joints and machine parts. K., 2002, "Phoenix", 300 p.
[9] A.S .No. 1214984, MPK8: F17D3 / 00, published 28.02.86.
[10] Patent of the Russian Federation No. 2511787, MPK9: F17D5 / 02, published April 10, 2014
[11] Kovalenko A.N. Systems for determination of location of pipeline defects. Testing and diagnostics, № 2, 2016, p. 27-35.
[12] But V.S., Oliynyk O.I. Strategy of development of technologies for repair of operating main pipelines. Collection of papers on "Problems of the resource and safety of operation of structures, constructions and machines" for 2004-2006, Resource, p. 490-500.
[13] Sarazha S.V. Implementation of the new concept of diagnostics of technological pipelines at OJSC "Samotlorneftegaz". "Territory of NDT", No. 4, 2013, p. 36-41.
[14] Galiulin R.V., Bashkin V.N., Galiulina R.A. The problem of non-sanctioned inserts in liquid hydrocarbon pipelines. Journal of Oil and Gas Construction. 2013, No. 4, p. 46 - 49.
[15] Galyautdinov A.A., Zubailov G.I. To the question on pipelines dismantling. Oil and gas business. 2007. http: www.ogbus.ru.

Gábor Vértesy*
Centre for Energy Research, Institute of Technical Physics and Materials Science, Budapest, Hungary

Nondestructive investigation of wall thinning in ferromagnetic material by Magnetic adaptive testing: influence of yoke size

Nieniszczące badanie przewężenia materiałów ferromagnetycznych za pomocą adaptacyjnych testów magnetycznych: wpływ rozmiaru jarzma

ABSTRACT

Magnetic adaptive testing is a powerful way of nondestructive evaluation. Minor magnetic hysteresis loops are systematically measured and evaluated. In the present work this technique was applied for detection of local thinning of ferromagnetic plates. The same plate with a given artificial slot was tested by different size magnetizing yokes. A definite maximum of magnetic descriptors was found, as a function of yoke size, which made possible the optimization of the yoke size for a given size of defect. The character of the maximum also revealed that the measurement is not sensitive for the geometrical parameters: the same yoke is suitable for detection of defects in a wide range. It was proved by simulation that the change of the magnetic flux density in the yoke – due to local thinning – was responsible for the observed effect. Good correlation was found between simulation and experimental data. The result of this work will help to find the optimal parameters of the experimental arrangement.

Keywords: *electromagnetic nondestructive testing, wall thinning, magnetic hysteresis measurements, magnetic adaptive testing, magnetic field simulation*

STRESZCZENIE

Magnetyczne testy adaptacyjne są skutecznym sposobem oceny nieniszczącej. W ich trakcie mniejszościowe pętle histerezy magnetycznej są systematycznie mierzone i oceniane. W niniejszej pracy zastosowano tę technikę do wykrywania miejscowego przewężenia płytek ferromagnetycznych. Ta sama płyta ze sztucznymi defektami została zbadana przy wykorzystaniu jarzma magnetyzującego o różnych rozmiarach. Określono maksymalną liczbę deskryptorów magnetycznych, zależnych od wielkości jarzma, co umożliwiło optymalizację rozmiaru jarzma dla danej wielkości defektu. Uzyskana charakterystyka ujawniła również brak wrażliwości wyników pomiaru na parametry geometryczne: to samo jarzmo nadaje się do wykrywania defektów w szerokim zakresie. Udowodniono, że za obserwowany efekt odpowiedzialna była zmiana gęstości strumienia magnetycznego w jarzmie - będąca wynikiem lokalnego przerzedzania. Stwierdzono dobrą korelację między symulacją a danymi eksperymentalnymi. Uzyskane wyniki umożliwią wyznaczenie optymalnych parametrów układu pomiarowego.

Słowa kluczowe: *elektromagnetyczne badania nieniszczące, przewężenie materiału, pomiary histerezy magnetycznej, magnetyczne testy adaptacyjne, symulacja pola magnetycznego*

1. Introduction

For pipes used in industry, wall thinning is one of the most serious defects [1, 2]. Local wall thinning on the inner surface of a pipe may occur due to the stream of coolant flowing inside the pipe, causing a serious problem of maintenance of the piping systems. The inspection should be done from the outer side of the pipe. Recently many nondestructive testing techniques have been used for the measurement of pipe wall thinning. Currently the magnetic flux leakage (MFL) method is the most commonly used pipeline inspection technique [3,4]. Another technique, the recently developed nondestructive magnetic method (Magnetic Adaptive Testing, MAT [5]) was also successfully applied for the inspection of wall thinning in layered ferromagnetic materials. MAT is based on systematic measurement of minor magnetic hysteresis loops and introduces a large number of magnetic descriptors to diverse variations in nonmagnetic properties of ferromagnetic materials, from which those, optimally adapted to the just investigated property and material, can be picked up. It was shown in [6] that Magnetic Adaptive Testing was an effective and promising tool for nondestructive detection of local thinning of a plate from the other side of the specimen. The method gave good results also in a layered ferromagnetic material. It was proved by these model experiments, that a 9 mm wide and 2 mm deep slot, made in a 3 mm thick ferromagnetic material could be well detected with good signal/noise ratio through one (or even two) air-gap(s) and through 3-6 mm additional ferromagnetic material. The slot is seen not only in case when the measuring yoke is positioned exactly above it, but from about ±10 mm distance, too, with an acceptable signal/noise ratio.

To improve the applicability of MAT, the measurement conditions should be optimized. On one side it is important to study, how the modification of the measured hysteresis loops, caused by the presence of an artificial slot in the investigated ferromagnetic plate are influenced by the geometry of the applied magnetizing yoke. For this purpose

*Correspondence author. E-mail: vertesy.gabor@energia.mta.hu

DOI: 10.26357/BNiD.2018.012

numerical simulation was performed. In our recent work [7] we calculated how the geometrical parameters of the measured arrangement affect the change of the magnetic flux inside the magnetizing yoke, which is the main source of the detected change in the measured signal. The yoke size and influence of air gap (which is extremely important in open magnetic circuits) were also taken into account in a three plate system of ferromagnetic plates. The result of simulation will help to find the optimal parameters of the experimental arrangement. On the other side it is also important to determine, how the real measured magnetic parameters depend on the size of the applied magnetizing yoke. The purpose of the present work is to study – both by simulation and by experiments – the influence of the size of magnetizing yoke on the magnetic parameters, in case of detection of an artificial slot in a ferromagnetic plate. The results of simulation and measurement are compared with each other as well.

2. Experimental arrangement

A 500 mm x 300 mm x 6 mm size carbon steel plate was chosen for the measurement, which contained a 10 mm x 1 mm size slot in the middle of the plate along the whole plate. The magnetizing yoke was moved over the top surface of the sample, while slot was located in the bottom side, as shown in Fig. 1.

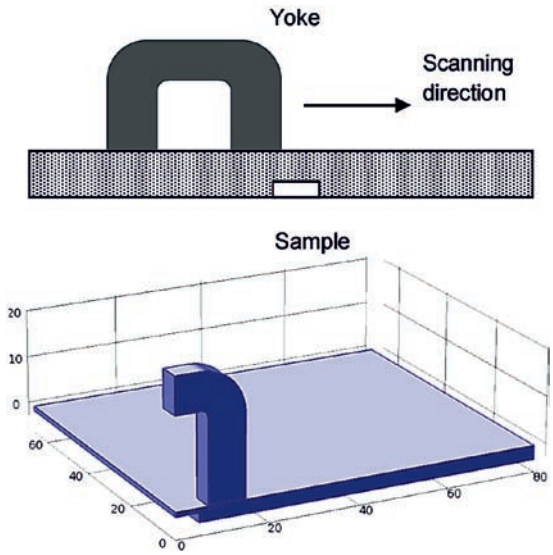

Fig. 1. Configuration used both for measurement and simulation. The geometry down represents a quarter-view of the arrangement, showing only part of the whole plate, and with the yoke in central position right above the slot.
Rys. 1. Konfiguracja używana zarówno do pomiarów, jak i symulacji. Geometria po prawej stronie przedstawia ćwiartkę układu, pokazując tylko część całej płyty, a także jarzmo w pozycji centralnej tuż nad szczeliną.

Tab. 1. Magnetizing yokes used for measurements and the distance between their legs.
Tab. 1. Odległości pomiędzy kolumnami jarzm magnesujących wykorzystanych podczas pomiarów.

Yoke No.	1	2	3	4	5	6
Distance between yoke legs (mm)	8	11	14	19	25	30

Different size of yokes were used. The yokes were C-shaped laminated Fe-Si transformer cores. The distance between the legs of the yokes are given in Table 1.

3. Numerical simulation

The AC/DC Module of the Comsol Multiphysics® finite element software was used for the simulations [8]. The physics setting is "magnetic fields" (mf), the governing equation of which is

$$\nabla \times \left(\mu^{-1} \nabla \times \vec{A}\right) = \vec{J}. \tag{1}$$

Here $\vec{A}$ is the magnetic vector potential, from which the magnetic flux density can be obtained as $\vec{B} = \nabla \times \vec{A}$, $\vec{J}$ is the current density, and μ stands for the local permeability of the media. Note that in this study one is allowed to use linear material model of both the yoke and the plate, for which we assumed $\mu = 5000\mu_0$. The excitation is prescribed as a surface current density $\vec{K}$ on the lateral surfaces of the "bridge" of the yoke, which adds up to a total current of 1 A. The flux through the yoke is computed by an integral of the flux density over the cross-sectional surface, S, of the yoke:

$$\Phi = \int_S \vec{B} \cdot \overrightarrow{ds} \tag{2}$$

The variation of magnetic flux, Φ_1 and Φ_2 was calculated according to the above described way. Let Φ_1 denote the flux in the yoke according to (2) when there is no slot in the material ($\mu_r = 5000$) and, in turn, Φ_2 be the flux in the presence of the slot ($\mu_r = 1$). We define the relative change of the magnetic flux as $|\Phi_1 - \Phi_2|/\Phi_1$. By the simulations we investigated how this flux change depends on the distance between the legs of the magnetizing yoke.

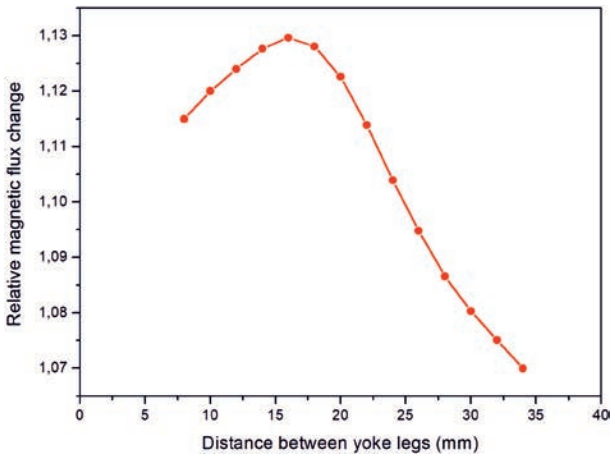

Fig. 2. Relative flux change $|\Phi_1 - \Phi_2|/\Phi_1$ in the yoke, as a function of the yoke leg distance.
Rys. 2. Względna zmiana strumienia $|\Phi_1 - \Phi_2|/\Phi_1$ w jarzmie, w zależności od odległości kolumny jarzma.

In Fig.2. the calculated flux change is plotted as a function of the distance between the legs of the magnetizing yoke. The Figure shows how the relative change of the flux, $|\Phi_1 - \Phi_2|/\Phi_1$ depends on the distance between the yoke legs. It can be seen that by optimal choice of the yoke, the obtained flux change can be maximized. As expected, the flux change depends on the dimensions of the magnetizing yoke (e.g. distance

between yoke legs). The presence of the slot results close to 13% modification in the relative magnetic flux change if the size of yoke is optimized to the size of slot. However, no drastic change is observed around the top area if the yoke size is modified by ±5 mm range.

4. Magnetic adaptive testing

MAT investigates a complex set of minor hysteresis loops (from a minimum amplitude of the magnetizing field, with increasing amplitude by regular steps) for each position of the magnetizing yoke. A specially designed Permeameter [9] with a magnetizing yoke was applied for measurement of families of minor loops of the magnetic circuit differential permeability. The samples were magnetized by the attached yoke, having a magnetizing and a pick-up coil, wound on the legs of the yoke. The magnetizing coil gets a triangular waveform current with step-wise increasing amplitudes and with a fixed slope magnitude in all the triangles. Block-scheme of the Permeameter and triangular variation of the magnetizing current with time are illustrated in Fig. 3.

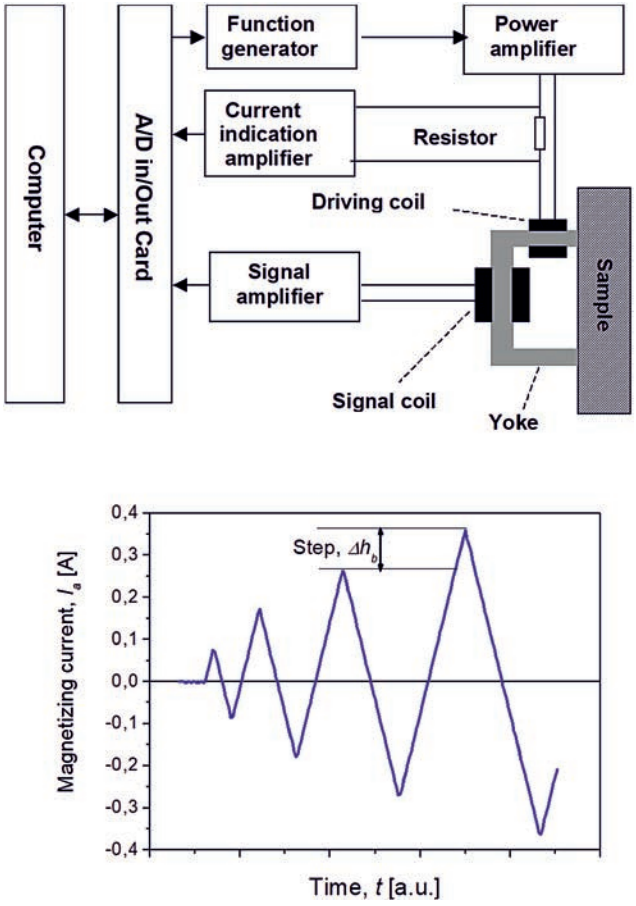

Fig. 3. Block-scheme of the Permeameter (up) and triangular variation of the magnetizing current with time (down).
Rys. 3. Schemat blokowy miernika przenikalności magnetycznej (góra) i przebieg trójkątny prądu magnesującego w czasie (dół).

This produces a triangular time-variation of the effective field in the magnetizing circuit and a signal is induced in the pick-up coil. As long as the field sweeps linearly with time, the voltage signal in the pick-up coil is proportional to the effective permeability of the magnetic circuit. The permeameter works under full control of a PC computer, which registers data files for each measured family of the minor "permeability loops".

The experimental raw data are processed by an evaluation program, which divides the originally continuous signal of each measured sample into a family of individual permeability half-loops. The program filters experimental noise and interpolates the experimental data into a regular square grid of elements, $\mu \equiv \mu(h_a,h_b)$, of a μ-matrix with a pre-selected field-step. Degradation functions, created straight from the induced signal (which is proportional to the average permeability measured in the magnetic circuit "measuring head – measured plate"), are labeled as the μ-degradation functions. Coordinates h_a, h_b of the elements represent the actual magnetic field value, h_a, on the actual minor loop with amplitude h_b. Each μ-element represents one "MAT-descriptor" of the investigated sample. The matrices are processed by another evaluation program, which divides values of their elements by corresponding element values of a chosen reference matrix (i.e. matrix standardization), and arranges each set of the mutually corresponding elements μ of all the evaluated μ-matrices into a μ(x)-degradation function. In general x can be any independently measured parameter. In our case this is the position of the center of the magnetizing yoke with respect to the axis of the slot when it moves step-by-step on the surface of the sample along a straight line perpendicular to the length of the slot. The slot is located on the bottom side and the axis of the yoke is oriented perpendicular to the axis of the slot. The details of experimental apparatus and evaluation (i.e. how the optimal MAT descriptors are chosen) are presented in [10]. In some cases, the degradation functions based on the derivative of permeability with respect to the field, h_a, $\mu' = d\mu/dh_a$ are more sensitive. They are referred to as the μ′-degradation functions.

Once the degradation functions are computed, the next task is to find the optimum degradation function(s) for the most sensitive and enough robust description of the investigated material degradation. The matrix-evaluation program calculates also sensitivity of each permeability μ(x)-degradation function and draws their "sensitivity map" in the plane of the field coordinates (h_a,h_b). A 3D-plot of sensitivity of the degradation functions can substantially help to choose the optimum one(s). This map shows relative sensitivity of each μ(x)-degradation function with respect to the independently measured x-parameter of the investigated material. Sensitivity of each degradation function is computed as the slope of its linear regression and it is expressed by a color and/or shade in the sensitivity map figure. This map is very useful if we want to characterize the reliability and reproducibility of the MAT descriptors. The sensitivity map gives useful information about the relative change of the investigated magnetic descriptor with respect to the independent variable (the top of the "hills" are those area(s) from where the most sensitive MAT-degradation functions can be taken). On the other side it also indicates, how reliably the parameter can be determined if the measurement is repeated (large plateaus are favourable from this point of

view, where parameters depend only very slightly from the actual choice of the exact field coordinates values h_a and h_b). In this measurement it is difficult to determine exact values of the magnetic field, h, inside the sample, due to the open magnetic circuit. Because of this the magnetizing current, I, (given in A) is used to characterize the samples' magnetization when MAT descriptors are evaluated.

5. Experimental results

The results of the measurements performed on the investigated plate containing the artificial slot are given in Fig. 4. Here the results of line scans are presented: different yokes (as shown in Table 1) were scanned over the surface in 5 mm steps along a line perpendicular to the direction of the slot. In all cases MAT degradation functions are normalized by the corresponding degradation function measured at the largest distance (–40 mm) from the centre of the slot, so the points in Fig. 4 represent the relative change of the magnetic parameter with respect to the „no slot" case. In the present case the derivative $d\mu/dI = \mu'$ was found as the most sensitive descriptor and therefore in the whole work the μ'-degradation functions are used. It is seen that in the most favourable case 100% modification of magnetic parameters was experienced caused by the presence of the slot.

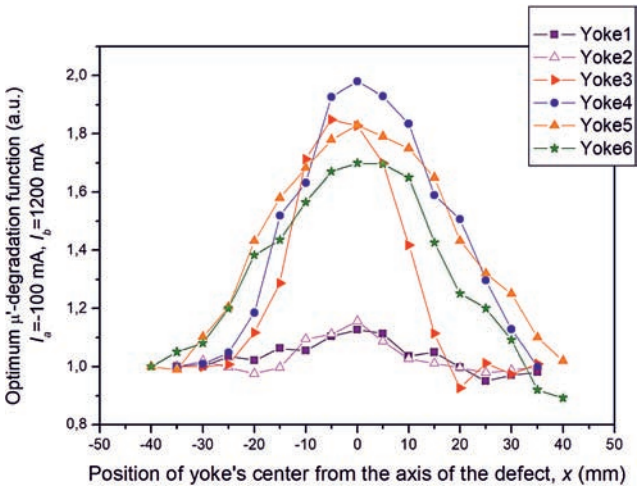

Fig. 4. The most sensitive μ' degradation functions, measured by different yokes, moving the yoke along the surface of the sample over the defect (defect's center is at x=0).
Rys. 4. Najbardziej czułe funkcje degradacji μ', mierzone przez różne jarzma, podczas przesuwania jarzma wzdłuż powierzchni próbki ponad defektem (środek defektu ma wartość x = 0).

The map of relative sensitivity of the μ'(x)-degradation functions in the case of yoke 4 is shown in Fig. 5. It is also indicated in this figure by crossing lines, from which point the "optimum MAT degradation function" of Fig. 4 is taken.

The maximal values of normalized MAT descriptors (which can be measured at x=0 position, see Fig. 4) are shown in Fig. 6 as a function of the size of magnetizing yoke. This curve is suitable on one side to determine the influence of the yoke size on the values of detectable MAT descriptors for the given arrangement, and on other side to make a comparison between simulated and calculated parameters.

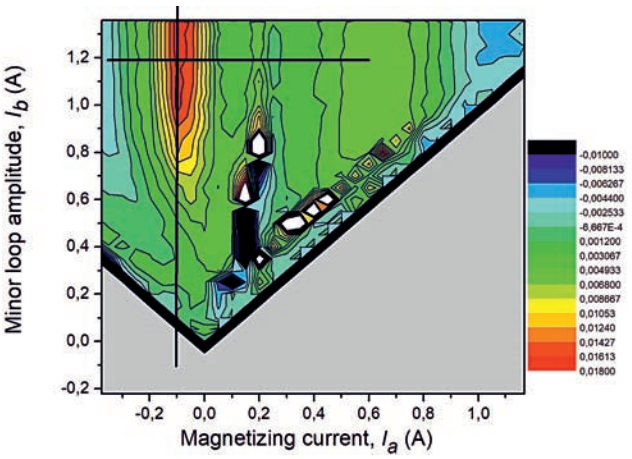

Fig. 5. Sensitivity map of the μ' degradation functions (measured by yoke 4). The degradation functions with the magnetizing current coordinates around I_a=–0.1 A, and with minor loop amplitudes larger than I_b =1 A have the top sensitivity, and is used in Fig. 4.
Rys. 5. Mapa czułości funkcji degradacji μ' (mierzona jarzmem 4). Funkcja degradacji z parametrami prądu magnesującego ok. I_a = -0,1 A oraz z amplitudami mniejszościowych pętli większymi niż I_b = 1 A ma najwyższą czułość i jest wykorzystywana na rysunku 4.

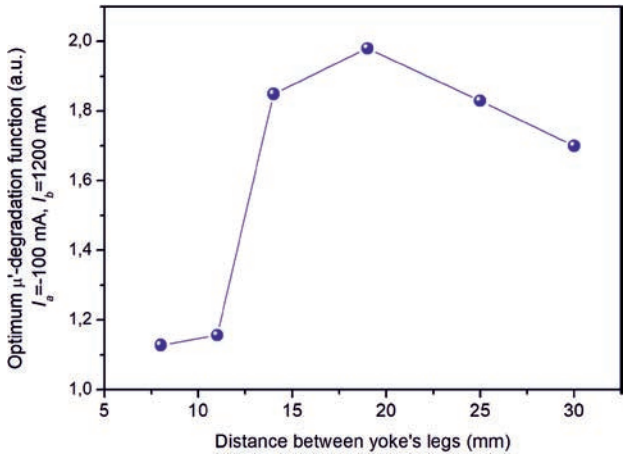

Fig. 6. The maximal values of normalized optimum MAT descriptors as a function of the distance between yoke legs.
Rys. 6. Maksymalne wartości znormalizowanych optymalnych deskryptorów MAT jako funkcji odległości między kolumnami jarzma.

6. Discussion

It was determined empirically that the value of MAT descriptors depend on the size of the magnetizing yoke, if measurements are performed on a ferromagnetic plate having an artificial slot on the bottom side. A definite, well measurable local maximum was found at 20 mm distance between the legs of the yoke. This shows that the geometry of the measurement arrangement (size of magnetizing yoke) can be optimized for a given size of defect. In this particular case a 10 mm wide slot can be detected the most effectively by a yoke having about 20 mm distance between the legs. This result concerns for the investigated case, where one model of the plate was applied with one definite size of defect. However, it is very probable that the observed correlation, that different size defects need different size yokes can be more general. It is assumed that this tendency is valid

for other cases, too, but for a definite and reliable answer to this question more efforts should be done.

The relatively flat curve around the optimal size of the yoke (see Fig. 6) is promising from that point of view, that the sensitivity of the detection of the slot is not influenced much (at least in a certain range) on actual choice of the magnetizing yoke's size.

Results of simulations gave similar correlation between the modification of magnetic flux in the yoke (due to defect) and size of yoke. It is worth of mentioning that the optimal size of yoke is more or less the same in empirical case and in simulation. This fact gives on one side a rather promising theoretical background for this type of nondestructive evaluation, and on the other side it means the empirical validation of the simulation.

7. Acknowledgement

The work was supported by the Hungarian Scientific Research Fund (project K 111662).

8. References/Literatura

[1] H.M. Crockett, J.S. Horowitz, „Erosion in nuclear piping systems", J. Pressure Vessel Technology, vol. 132, 024501-1, 2010
[2] I. Nishiguchi, F. Inada, M. Takahashi, B. Ogawa, T. Inagaki, T. Ohira, K. Iwahara, K. Yamakami, „A Review: Japanese Pipe wall thinning management based on JSME rules recent R&D studies performed to enhance the rules", E-Journal of Advanced Maintenance, vol. 2 pp. 14-24, 2010/2011
[3] H. Kikuchi, Y. Kurisawa, K. Ara, et al., "Feasibility study of magnetic flux leakage method for condition monitoring of wall thinning on tube", Int. J. Appl. Electromagnetics and Mechanics, vol. 33, pp. 1087-1094. (2010)
[4] P.B.C. Rao, „Magnetic Flux Lekage Technique: Basics", Journal of Non Destructive Testing & Evaluation, vol. 11, pp. 7-17, 2012
[5] I. Tomáš, "Non-destructive magnetic adaptive testing of ferromagnetic materials", J.Magn.Magn.Mat., vol. 268/1-2, pp. 178-185, 2004
[6] G. Vértesy, I. Tomáš, T. Uchimoto, T. Takagi, "Nondestructive investigation of wall thinning in layered ferromagnetic material by magnetic adaptive testing", NDT & E International, vol. 47, pp. 51-55, 2012
[7] G. Vértesy, B. Bálint, A. Bingler, S. Gyimóthy, S. Bilicz, J. Pávó, „Simulation of magnetic flux distribution for the measurement of the local thinning of ferromagnetic plates", International Journal of Applied Electromagnetics and Mechanics, vol. 55, pp. 597–612, 2017
[8] AC/DC Module User's Guide, COMSOL, October 2014
[9] I. Tomáš, O.Perevertov, in: JSAEM Studies in Applied Electromagnetics and Mechanics 9, ed. T. Takagi and M. Ueasaka, (IOS Press, Amsterdam, 2001), pp. 5-15
[10] I. Tomáš, G. Vértesy, „Magnetic Adaptive Testing", chapter in book „Nondestructive Testing" (Editor M.Omar), InTech-d.o.o. - Open Access publisher: www.intechopen.com, (ISBN 979-953-307-487-9), 2012

Konferencje NDT

47. Krajowa Konferencja Badań Nieniszczących KKBN

Mamy przyjemność zaprosić Państwa do udziału w 47. Krajowej Konferencji Badań Nieniszczących, która odbędzie się w dniach 16-18 października 2018 r.

Krajowa Konferencja Badań Nieniszczących jest corocznym wydarzeniem, które w 2018 roku będzie miało swoją czterdziestą siódmą odsłonę.

KKBN jest miejscem omówienia ostatnich dokonań w zakresie badań nieniszczących, jak również inspiracją do dalszych prac naukowych oraz szansą na nawiązanie nowych relacji biznesowych. 47. KKBN będzie okazją do wymiany wiedzy i doświadczeń dla wszystkich uczestników, zapoznania się z nowościami technicznymi i technologicznymi na rynku badań nieniszczących i diagnostyki technicznej.

Termin zgłaszania referatu upływa 1 lipca 2018 r.

Szczegółowe informacje oraz najważniejsze terminy dla referentów, wystawców i uczestników dostępne są na stronie Konferencji www.kkbn.pl.

Komitet Organizacyjny 47. KKBN:

- Bogusław Olech
  tel.: (+48) 601 795 718, e-mail: 47kkbn@kkbn.pl
- Ryszard Bartz
  tel.: (+48) 604 849 280, e-mail: wystawa@kkbn.pl
- Komitet Naukowy
  e-mail: komitetnaukowy@kkbn.pl

Krajowa Konferencja Badań Radiograficznych KKBR 2018

Zapraszamy uprzejmie do udziału w XX Krajowej Konferencji Badań Radiograficznych „Stary Młyn 2018", która odbędzie się w dniach od 10 do 12 września 2018 r. w Ośrodku Konferencyjnym „Stary Młyn", 98-430 Bolesławiec k. Wieruszowa, ul. Młyńska 11.

Konferencja ma charakter szkoleniowy oraz stanowi forum dla personelu związanego z zapewnianiem jakości materiałów, wyrobów i konstrukcji spawanych, dla personelu laboratoriów, kontroli technicznej oraz inspektorów ochrony radiologicznej (IOR). Ramowy program konferencji obejmuje wykłady i referaty prezentowane na sesjach plenarnych oraz wystawę aparatury kontrolno-pomiarowej i materiałów stosowanych w badaniach nieniszczących.

Termin zgłaszania uczestnictwa i wniesienia opłaty to 20 sierpnia 2018 r.

Szczegółowe informacje dostępne są na stronie www.ndt-system.com.pl w zakładce Konferencje.

Kontakt emailowy: level_tmo@onet.pl, tel.: 601 259340

Organizatorzy XX KKBR:

- NDT System
- Politechnika Opolska
- Usługi Techniczne i Ekonomiczne "Level"

Informacje dla Autorów i Czytelników

PROFIL CZASOPISMA

Kwartalnik „Badania Nieniszczące i Diagnostyka" jest czasopismem naukowo-technicznym Wydawanym przez Stowarzyszenie Inżynierów Mechaników Polskich w Warszawie we współpracy z Towarzystwem Badań Nieniszczących.

Odbiorcami czasopisma są specjaliści, ośrodki naukowe, dydaktyczne i organizacje gospodarcze zainteresowane problematyką określoną w tytule czasopisma. Czasopismo jest wysyłane również do ważnych ośrodków zagranicznych zainteresowanych tą tematyką.

Czasopismo wydawane jest w języku polskim i jest dostępne zarówno w wersji drukowanej jak i w elektronicznej w internecie. Artykuły publikowane w języku polskim mają dodatkowo streszczenia oraz opisy rysunków i tabel w języku angielskim. Wybrane artykuły naukowe publikowane są w języku angielskim.

W czasopiśmie „Badania Nieniszczące i Diagnostyka" są publikowane oryginalne komunikaty i artykuły dotyczące:

- metodologii badań,
- certyfikacji w badaniach,
- charakterystyki urządzeń, sprzętu, materiałów i systemów w badaniach nieniszczących,
- diagnostyki,
- szkoleń, przepisów i normalizacji,
- praktyki badań w przemyśle i poradnictwa technicznego,
- wydarzeń, karier zawodowych specjalistów i ich doświadczeń zawodowych.

WSKAZÓWKI DLA AUTORÓW

Objętość artykułu powinna wynosić do 10 stron, a komunikatu 1 ÷ 4 stron wydruku komputerowego na arkuszu formatu A4 bez tabulatorów i wcięć, czcionka Times New Roman 12, marginesy górny, dolny, lewy i prawy - 2,5 cm.

Rysunki i tablice z ich tytułami winny być umieszczane w tekście. Rysunki, wykresy i fotografie należy nazywać rysunkami (np. Rys. 1), a tablice (np. Tab. 3) i numerować cyframi arabskimi.

Opisy znajdujące się na rysunkach oraz grubość linii powinny mieć wielkość umożliwiającą zmniejszenie rysunku do 30%. Maksymalna szerokość rysunku jednoszpaltowego wynosi 8,5 cm, natomiast dwuszpaltowego 17,5 cm.

Rysunki wykonane komputerowo winny być w oddzielnych plikach w formacie JPEG min. 300 DPI.

Jednostki - układ SI.

Artykuł powinien zwierać:

- informacje o autorach: stopnie naukowe lub zawodowe, instytucja i zdjęcia (w osobnym pliku);
- imię i nazwisko;
- tytuł artykułu;
- streszczenie (do 0,5 strony) z informacją dotyczącą problematyki artykułu, metodyki badań, obliczeń lub analizy problemu oraz wyniku końcowego;
- tekst wraz z podziałem na zatytułowane rozdziały;
- wnioski końcowe;
- wykaz literatury; pozycje literatury numerowane cyframi arabskimi w kwadratowych nawiasach i w kolejności cytowanej w tekście.

Artykuły w formie pliku Word należy przysłać na adres e-mail: wydawnictwo@ptbnidt.pl wraz z wypełnionym drukiem „Zgłoszenie publikacji" dostępnym na naszej stronie www: www.bnid.pl.

OGŁOSZENIA I ARTYKUŁY PROMOCYJNE

Ogłoszenia i artykuły promocyjne w kwartalniku "Badania Nieniszczące i Diagnostyka" – czasopiśmie ogólnopolskim dostępnym w formie drukowanej i elektronicznej na naszej stronie internetowej docierają do szerokiej grupy specjalistów.

W czasopiśmie zamieszczane są kolorowe i czarno-białe: ogłoszenia reklamowe na okładkach lub wewnątrz numeru oraz wrzutki dostarczane przez zleceniodawcę; artykuły techniczno-informacyjne jak również informacje o wydarzeniach oraz imprezach naukowo-technicznych. Cennik i forma ogłoszeń dostępne są na naszej stronie www: www.bnid.pl.

PRENUMERATA

Aktualne wydania dostępne w prenumeracie: 1–4/2018 oraz archiwalne: 1–2/2016; 1–2/2017; 3/2017; 4/2017.

Prenumerata realizowana jest przez Redakcję. Kontakt i zamówienia pod adresem mailowym: prenumerata@bnid.pl.

TELEMOND HOLDING

telemond-holding.com

TELESKOP we produce the future

MONTEL we produce the future

TELEYARD we produce the future

HENSCHEL ENGINEERING AUTOMOTIVE

facebook.com/telemond

W skład Holdingu Telemond wchodzą cztery Spółki: Teleskop, Montel, Teleyard i Henschel Engineering Automotive. Jesteśmy specjalistami w zakresie przetwarzania wysokowytrzymałych drobnoziarnistych stali konstrukcyjnych. W naszych zakładach realizujemy usługi między innymi w zakresie realizacji wszystkich powszechnie stosowanych procedur spawalniczych, cięcia blach i rur, obróbki mechanicznej, lakierowania i montażu. Wykonujemy konstrukcje stalowe, zarówno jako pojedyncze elementy jak i złożone moduły dla najważniejszych producentów z branży motoryzacyjnej i maszyn budowlanych. Od wielu lat darzą nas zaufaniem tacy klienci jak np. Liebherr oraz Volkswagen. W zakresie realizacji projektów oferujemy pełen zakres usług. Zajmujemy się zakupem, wykonaniem, a także logistyką, montażem i zapewnieniem jakości.

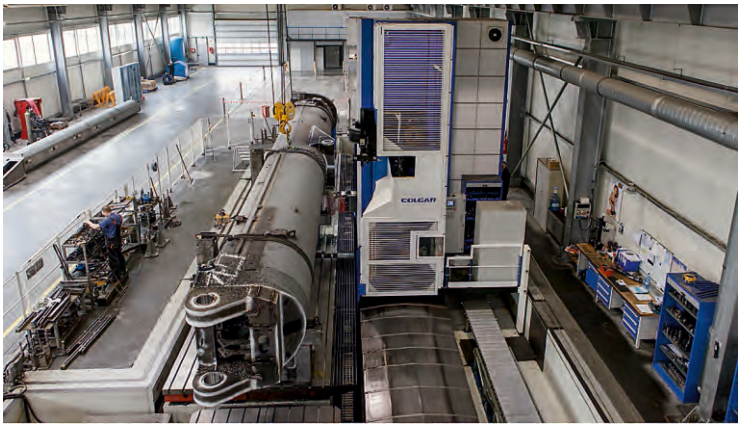

Spółka Holdingu Firma Teleskop jest największym pracodawcą w Kostrzynie nad Odrą zatrudniając ponad 600 pracowników. W naszych osiemnastu halach produkcyjno-montażowych wytwarzamy od podstaw sprzęt transportowy, konstrukcje spawane ze stali o wysokiej wytrzymałości dla czołowych producentów dźwigów oraz podzespoły dla producentów z sektora kolejowego. Specjalizujemy się również w produkcji wysięgników teleskopowych, chwytaków kontenerowych i podzespołów urządzeń dźwigowych.

Najmłodszą ze spółek córek Holdingu jest Firma Teleyard, która produkuje konstrukcje spawane wykonane ze stali o wysokiej wytrzymałości i odporności na ścieranie, kierując swoją ofertę przede wszystkim w stronę sektora offshore systemów kontenerowych. Teleyard wykonuje także specjalne projekty w zakresie produkcji o dużych wymiarach i ciężarze. Spółka wybudowała w 2015 roku fabrykę w Szczecinie, która specjalizuje się w wielkogabarytowych konstrukcjach stalowych. Powstają w niej między innymi części dźwigów, chwytaków, specjalistyczne wyposażenie pogłębiarek.

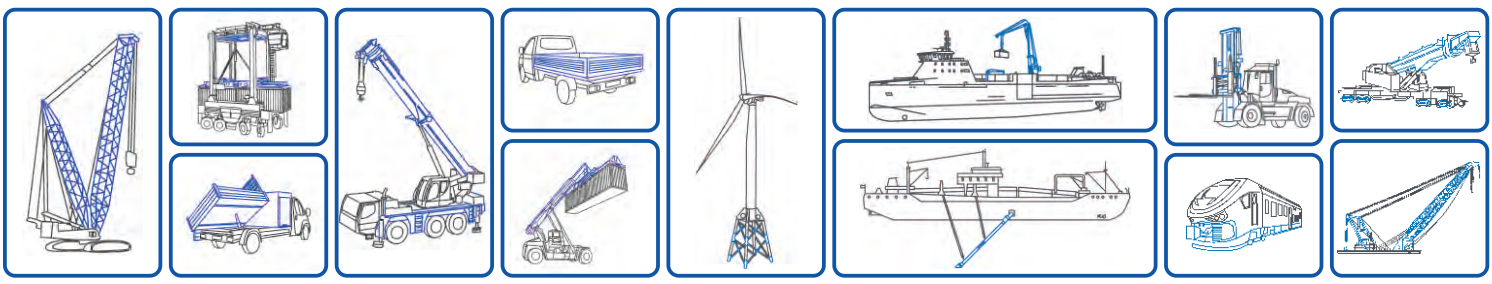

BAKER HUGHES
a GE company

Channel Partner

Mentor Visual iQ teraz w wersji HD

Najlepszy WideoBoroskop na rynku teraz z sondą High Definition

Nowy Mentor Visual iQ, teraz z **TrueSight Imaging** w wersji HD to jeszcze szybsze i dokładniejsze badania. Nowy intuicyjny ekran dotykowy, indywidualne profile użytkownika oraz trójwymiarowe obrazowanie w Pomiarze Fazowym **Real3D Measurement**, to tylko niektóre możliwości, znacznie podnoszące efektywność badań wizualnych. Inteligentne rozwiązania wbudowane w platformę Mentor Visual iQ, to większa efektywność badań oraz trafniejsze decyzje.

Więcej na temat nowego podejścia GE do badań nieniszczących na: **everestvit.pl** lub **endoskopy.pl**

---

technologia badań wizualnych
Everest
Polska

Everest Polska Sp. z o.o.
ul. Geodetów 176, 05-500 Piaseczno k. Warszawy
tel. (+48 22) 750 50 83, faks: (+48 22) 750 70 21
email: everestvit@everestvit.pl, **www.everestvit.pl**